January 2012

Shape-Shifting Surfaces for Rapid Release and Direct Stamping of Organized Micro-Tissues

Samuel James Dupont
University of South Florida, prozacsmile@yahoo.com

Shape-Shifting Surfaces for Rapid Release and Direct Stamping of Organized Micro-Tissues

by

Samuel J. DuPont, Jr.

A dissertation submitted in partial fulfillment
of the requirements for the degree of
Doctor of Philosophy
Department of Chemical and Biomedical Engineering
College of Engineering
University of South Florida

Major Professor: Ryan Toomey, Ph.D.
Nathan D. Gallant, Ph.D.
Mark Jaroszeski, Ph.D.
Piyush Koria, Ph.D.
Donald Haynie, Ph.D.

Date of Approval:
November 14, 2012

Keywords: poly(N-isopropylacrylamide), tissue engineering, soft materials, cellular organization, cell stamping

Dedication

I dedicate this dissertation to the loving memory of my grandmother, Shirley Weigenthaler. Without her encouragement and assistance I may have never began my collegiate adventure and experienced the challenges and joys of the hard work required to earn my Ph.D. I am also extremely thankful for the wisdom and support provided to me by my loving parents Samuel DuPont Sr. and Debbie DuPont.

I would also like to thank all of my close friends who have eased my insanity and brought joy to my eyes during the rough patches.

Acknowledgments

First, and foremost, I would like to acknowledge the exhaustive assistance, professional wisdom, and inspiring insights afforded to me by my mentor and advisor Dr. Ryan Toomey. Without his patience and persistence my success as a student would not have been complete.

I would also like to acknowledge Mark Llyod and Joseph O. Johnson at the H. Lee Moffitt Cancer Center analytical microscopy core for assistance in the acquisition of images via confocal microscopy, the staff at the Nanotechnology Research and Education Center (NREC) (USF) for assistance in photolithography, and Dr. Steve Saddow and his lab group for assistance with atomic force microscopy. I have recieved proffessional support from numerous faculty and staff including: Dr. John Wolan, Dr. Richard Pollenz, Dr. Tapas Das, Jaime Fargen, Leigh West, and Rafael Urena. A number of fellow students have provided technical assistance as well as moral support and brief moments of comical relief from everyday student life. These outstanding friends and fellow students include: Audrey Buttice, Dave Rodenfels, Dr. Matthew Cutter, Dr. Russell Ferlita, Dr. Kenneth Nilsson, Ryan Cates, Dr. Kranthi Elineni, Melissa Pope, Dr. Janelle Christensen, Claire Osborne, Gulnur Efe, Maritza Muniz, Leena Patra, Chris Connor, Dr. Christopher Frewin, Dr. Christopher Locke and Dr. Ajay Vidyasagar.

Finally, I would like to acknowledge my committee for their guidance and oversight of my journey.

Table of Contents

List of Tables

List of Figures

Abstract

The primary aim of the research in this study is to develop a robust and simple platform for the *in vitro* organization of cells on surfaces which facilitate rapid cell release and allows for the direct stamping of highly organized micro-tissues. Current approaches towards this goal have been very successful but are lengthy and subject cells to harsh conditions for extended periods of time raising questions regarding cell health and maintenance of physiological state. To address these concerns a platform was developed to allow for rapid cell release by utilizing a release mechanism different from previous work.

Micron-scale structures comprised of the thermally responsive polymer poly(N-isopropylacrylamide) (pNIPAAm) were fabricated into various geometries to serve as a platform for cell culture. Structures were covalently confined to rigid surfaces causing non-uniform distortion of the structure's geometry upon swelling. This resulted in four primary modes of geometric distortion, or swelling-induced instability: differential lateral swelling, localized edge buckling, bulk structural buckling, and surface wrinkling. It was found that slight modifications to a linear elastic model was sufficient to predict these behaviors and provided guidance on design of the cell culture platform. Observations also suggest that a rapidly swelling structure engenders multiple forms of instability which arise as sequential and discrete steps during the swelling process. At each step the length

scale of the instability increases in a step-wise fashion until the final equilibrium structure is reached.

Culture of NIH 3T3 fibroblasts atop pNIPAAm structures of various geometries resulted in the growth of highly aligned micro-tissue building blocks with three distinct geometries: planar aligned micro-tissue sheets, “ribbon-like” micro-tissues, and “fiber-like” micro-tissues. Release of the micro-tissues was facilitated by the thermally-induced shape-shifting nature of micron-scale pNIPAAm structures. Release occurred rapidly (~3 min) and required a more mild temperature shift ($\Delta T \approx 9°C$) than other approaches. It was found that the mechanism for cell detachment was mechanical in nature and did not require cellular activity unlike other approaches. Cell detachment was directly correlated to surface strain as a result of thermally-induced shape-shifting and has a level of dependence on cellular contractility.

The platform was tested to show its capacity to directly translocate organized micro-tissues to a virgin surface. Cell transfer by direct stamping was achieved with micro-tissues retaining their shape, although stamped micro-tissues lost their organization after several hours of culture. Although the stamping process requires additional optimization, these results provide evidence that this platform has the capacity to culture and directly translocate highly organized micro-tissues. Additionally, this process provides a new, minimally invasive, approach to cell culture such that rapid construction of highly organized multi-layered tissues can be realized.

Chapter 1: Introduction

This chapter serves as a primer for the research outlined in this study. Material presented in this chapter only presents the basic concepts of the important topics addressed throughout the study. Each chapter will contain its own background which will present a more specific overview of the pertinent information for the research presented in that chapter.

1.1 "Smart Materials"

Materials and material science are at the core of a majority of engineered systems. The flexibility of designing materials for application in both highly specialized and broad engineering designs manifests from the intricate molecular interactions between the engineered material and its physical environment. Over the past 20 years much attention has been focused on the integration of materials into engineering design which have dynamic properties that manifest by responding directly to chemical and physical cues in the environment. These materials are often referred to as responsive or "smart" materials. The phrase "smart material" refers to a material's ability to change its chemical and physical properties in tandem with a change in its environment. Typically, the environmentally induced change in material properties is dramatic in comparison to the magnitude of the change in the environmental variable. Additionally, another hallmark of these materials is the reversible nature of the response allowing the material to

dynamically shift between at least two states which have dramatically different chemical and/or mechanical properties. These features allow for enhanced engineering design as specific functions can be "programmed" into the material upon fabrication through discrete changes in material chemistry and geometry.

"Smart" or responsive materials truly represent a class of materials which benefit from modern advances in understanding molecular interactions, as this understanding plays a key role in the "programming" and predictive functionality of the material. "Smart" materials have been described, designed, and studied possessing numerous modes of response to environmental cues such as temperature [1-3], pH [4-7], ionic strength [7], light [8, 9], chemical species [10, 11], solvent composition [12], magnetic fields [13], electrical fields [14], and stress fields [15, 16]. With an expansive catalog of environmental cues available for dynamic material response, engineering design of this class of materials has been eagerly applied to a plethora of fields including: drug delivery [6, 14, 17], microfluidics [9, 18], chemical sensing/detection [5, 10, 11, 19], and tissue engineering [20-24].

1.1.1 Poly(N-isopropylacrylamide) (pNIPAAm)

While "smart" responsive materials have gained increased attention in the scientific community, one material in particular stands out as the most studied and applied; the thermally responsive polymer poly(N-isopropylacrylamide) (pNIPAAm). Like many responsive materials, pNIPAAm exhibits its response in the form of a volume/phase transition. Due to the thermally responsive nature of pNIPAAm, a dramatic shift in the aqueous solubility of pNIPAAm chains occurs within a slight thermal shift around its "programmed" critical temperature often referred to as its lower critical

solution temperature (LCST) or demixing temperature. This represents the temperature at which the rapid response is engendered and can be used as a switch to drastically shift between two distinct material states. Additionally, the demixing temperature can be tuned by augmenting either the aqueous environment by changes in ionic strength or pH as well as augmenting the chemistry of the polymer through introduction of co-polymers.

1.1.2 Swelling Behavior of pNIPAAm

For a typical native pNIPAAm chain, the LCST occurs closely around 32°C, above which the chains are in a hydrophobic or insoluble mode and the polymer is in a tightly packed globule confirmation due to dominate hydrophobic interactions between adjacent isopropyl groups along the chain. This rapid change between solubility states is a distinguishing feature of pNIPAAm in an aqueous environment while solubility in other solvents is a more gradual function of system temperature. When the aqueous environment shifts below the native LCST, polymer chains rapidly shift from a hydrophobic mode to a hydrophilic mode causing the isopropyl groups along the chain to become soluble in the surrounding bulk water leading to hydration and relaxation of the chains and ultimately resulting in well dispersed coiled chains [1, 25, 26]. Although the mechanism by which the rapid transition of pNIPAAm's solubility in water is not completely understood the hydrophobic/hydrophilic transition has been greatly attributed to the affinity for hydrogen bonding of water subject to the thermal and chemical conditions of the environment [3, 27-30]. The general structure of the pNIPAAm side-chain is provided in Figure 1-1.

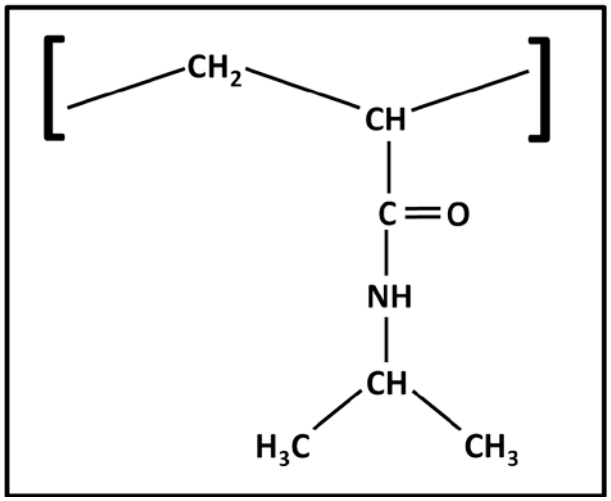

Figure 1-1: Molecular structure of a pNIPAAm side-chain.

The molecular structure of a pNIPAAm side-chain possesses two distinct features which play an important role in the thermally induced transition in polymer solubility, the dominantly hydrophilic carbonyl (C=O) and amide (N-H) moieties and the dominantly hydrophobic isopropyl (H_3C-CH-CH_3) group. At temperatures below the LCST the hydrophilic moieties are strongly hydrogen bonded with surrounding water molecules while cage-like water structures sometimes referred to as “ice-bergs” (due to their similarity to the molecular structure of ice) are ordered around the hydrophobic isopropyl chains [31, 32]. As the thermal energy of the aqueous environment rises beyond the LCST, hydrogen bonding weakens and water surrounding the hydrophobic isopropyl groups is discharged. This allows for increased proximity between adjacent isopropyl groups along the polymer chain causing hydrophobic interactions to dominate resulting in a collapse of the polymer chain and ultimately precipitation of the molecule [2, 31, 33].

Swelling of pNIPAAm polymers can be different depending on the physical arrangement and interconnectivity of the polymer chains. Various configurations of

pNIPAAm structure are presented in Figure 1-2. Polymeric materials, such as pNIPAAm, can exist as either free or confined linear chains such as those illustrated in Figure 1-2a and Figure 1-2b or as a network of interconnect chains forming a single continuous molecule or gel (Figure 1-2c – Figure 1-2e).

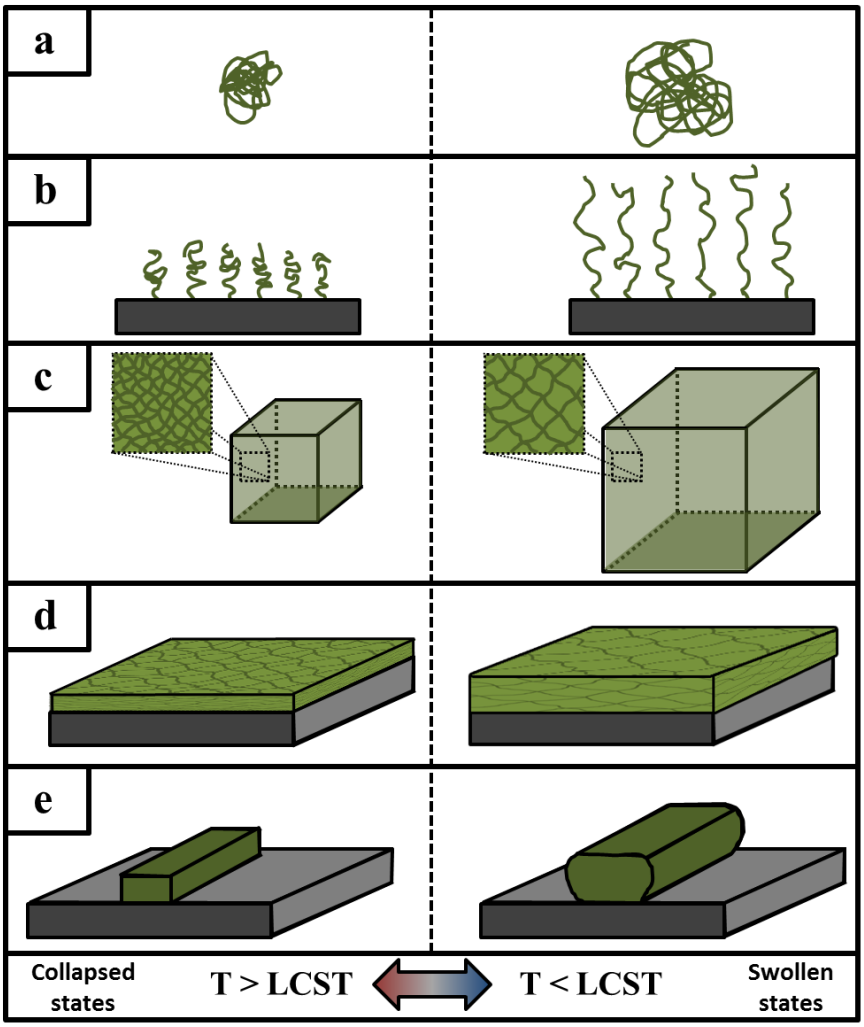

Figure 1-2: Basic types of pNIPAAm material conformations. Illustrations for (a) free linear chains, (b) surface tethered linear chains, (c) 3D crosslinked gel, (d) Surface confined crosslinked thin film, and (e) surface confined 3D crosslinked gel.

1.1.3 Free Linear pNIPAAm Chains

The simplest form of pNIPAAm is that of a free linear chain. In this case the pNIPAAm molecule is a repeating chain of N-isopropylacrylamide groups with each end of the polymer being free from constraint (Figure 1-2a). At temperatures below the LCST, polymer chains are well solvated resulting in a soluble coiled state while at temperatures above the LCST the chains are in a tightly packed insoluble globule state [(26)]. The thermally induced transition from the globule state to the coiled state upon hydration of the polymer chains results in a rapid increase in both the hydrodynamic radius and the root-mean-square radius of gyration [(1)]. This rapid change in polymer properties has been exploited to enhance flocculation and settling due to a rapid increase in polymer density as well as a shift in the adsorption characteristics of the chain allowing for aggregation of suspended particles and eventual settling at temperatures above the LCST [(34-36)].

1.1.4 Surface Tethered pNIPAAm Linear Chains

The second, slightly more complex, scenario involves the same linear pNIPAAm chains but rather than both ends being free, one terminal end of the polymer is chemically tethered to another material surface (Figure 2b). Typically these structures are referred to as polymer brush surfaces due to the polymer chains being forced to stretch away from the confining surface in densely grafted systems such that the chains resemble bristles on a brush. Although the swelling behavior of pNIPAAm brushes is similar to that of free linear chains, confinement to the surface causes the transition to dramatically change the properties of the brush surface. The two most notable changes which occur during

swelling of the pNIPAAm brush surface are a significant increase in brush thickness as well as a significant increase in surface wettability as measured by a reduction in contact angle [37, 38]. These property changes have been widely applied in engineering design as a method of functionalizing materials to provide a thermally switchable mechanism of control. Selective adhesion has been a primary focus in engineering application of pNIPAAm grafted surfaces. For instance, one study shows the application of pNIPAAm film surfaces in combination with a selective heating strategy for protein separation. This was possible due to the rapid shift in adsorption properties when the material was cycled through its transition [39]. Functionalized surfaces have also found use in achieving control over bacterial adhesion as an active surface for prevention of bio-fouling [40-42]. In light of their ability to control adhesion of proteins and cells, grafted pNIPAAm surfaces have found wide application in the arena of tissue engineering. Most notably, a process developed by Okano in the early 90's where grafted pNIPAAm surfaces were shown to have the ability to release cultured cells due to the change in hydration state of the surface [43-46].This was achieved by grafting pNIPAAm to standard polystyrene culture surfaces having film thicknesses of <30nm. This widely applied approach for controlling cell adhesion is generally referred to as "cell sheet engineering" and has been applied to an expansive library of cell types for growth and recovery of harvested micro-tissues [45, 47, 48].

1.1.5 Crosslinked pNIPAAm Gels

The third case involves the formation of a three-dimensional (3D) network of polymer chains where there are covalent points of attachment between neighboring chains referred to as physical crosslinks. In this scenario numerous pNIPAAm chains are

joined together to form a single macromolecule or polymer gel (Figure 2c). Swelling of unconfined 3D crosslinked networks results in a hydrogel which occupies a significantly greater volume than its unswollen counterpart due to hydration of the network chains. Although the volume of the gel greatly increases, it typically retains the same proportionate geometry of the collapsed or non-swollen state due to isotropic swelling. Swelling in a crosslinked gel differs from swelling in single linear chains as expansion of network chains are balanced by the physical crosslinks in the gel giving rise to two competing phenomena; a Flory-like energy of mixing which drives gel swelling through chain hydration and a Hookean-like elastic energy which ultimately limits the elongation of polymer chains between crosslinks [49-52]. The equilibrium volume is engendered when these two energies are balanced and the stress of the system is zero everywhere leading to an isotropic expansion of the original shape. Due to the thermally reversible nature of pNIPAAm gels, the material properties of the gel also change in response to the transition. For instance, the elastic properties of the material are altered upon swelling where Young's modulus is significantly reduced by as much as $1/10^{th}$ of its value in the collapsed state due to expansion of the crosslinked network [53, 54]. Crosslinked pNIPAAm gels have been extensively applied in design of drug delivery platforms [6, 55, 56] and flow control in microfluidics [57, 58].

1.1.6 Surface Confined Crosslinked pNIPAAm Gels

A confined gel has a portion of its surface bound to another, usually rigid, surface (Figure 2e). In this case the underlying mechanism that causes the responsive transition is similar to an unconfined gel, but the effects of confinement have a significant impact on

swelling such that expansion of the network becomes anisotropic. This swelling anisotropy arises from the clamped boundary condition as expansion at the confinement interface is zero and results in non-uniform propagation of compressive stresses during expansion. These swelling non-uniformities lead to adoption of geometries far different from the original gel shape such a wrinkled surfaces [59-63] , structural buckling [49, 64-69], and differential lateral swelling [70, 71]. Recently, a considerable amount of attention has been focused towards understanding and modeling of confinement-induced swelling and the formation of these geometrically rich structures [64, 66, 67, 69, 71-73]. Swelling of confined gels is typically considered to be a non-linear elastic process due to the magnitude of material deformations suggesting the requirement of a complex model to describe the process [71, 74, 75]. In contrast, models derived from linear elasticity have proven effective at describing a majority of the behavior in these systems [49, 66, 67, 69, 76]. For instance, the onset of buckling and its characteristic wavelength in a swollen acrylamide gel confined to a rigid surface was shown to be explained by a simple linear theory derived from application of the Föppl–von Kármán equations for large deformations in thin elastic plates [66]. A similar approach was also applied to predict the buckling behavior of pNIPAAm nano-lines [69]. Additionally, Biot's theory of linear poroelasticity was found to sufficiently predict the swelling kinetics and surface curvature in pNIPAAm structures constrained to one-dimensional swelling [76, 77]. These models provide a much simpler relationship between material parameters and swelling of the material as they assume that deformations are small such that the relationship between the deformation field and stress field is linear.

Although the formation of these geometries is not fully understood, they stand to enrich engineering design of surfaces by allowing for switchable surface morphologies. One such application involved the confinement of an array of rectangular patterns on a surface with defined spacing which allowed for size based separation of particles. Upon particles of an appropriate size entering between the rectangular structures, thermally induced swelling of the structures resulted in the "closing" of the channels due to differential lateral swelling, and ultimately entrapment of the particles. Once particles of larger sizes were removed by rinsing, the entrapped particles could then be released by thermally inducing the deswelling of the structures [(70)]. Additionally, wrinkle formation in swollen poly(n-butyl acrylate) films was "locked" in to generate permanently wrinkled surfaces. It was shown that the characteristic wavelength of the wrinkles could be easily controlled by the initial geometry of the film and resulted in fine control over the adhesive properties of the surface [(62)].

1.2 Tissue Engineering

Tissue engineering is a new and emerging scientific field which aims to organize living cells into tissue-like structures through use of engineered materials and biological components such as growth factors, proteins, and cells. Ultimately, engineering of "tissue building blocks" serves two primary purposes in medicine and research science: development of implantable tissues for repair or regeneration of damaged tissues *in vivo*, and development of platforms for the evaluation of cellular activity and behavior for enhancement of drug discovery, biomaterial development, and fundamental research in cell biology and physiology. With the recent lift on the ban which stifled research in the

field of stem cells, it has become increasingly attractive to develop robust platforms and novel techniques for cellular organization and application [78].

Although tissue engineering is typically considered a new and emergent field, humans have been practicing the fundamental concepts of tissue engineering for over 3,500 years. For instance, Sanskrit texts dating back to 1500 BCE describe the reconstruction of mutilated human noses using skin grafts from the buttocks [79]. Further advances in rhinoplastic surgeries involving skin grafts reached into the 15th century and by the 19th century, autograft-based surgeries began to become an accepted scientific practice with the first documented success in allograft transplant from human cadaveric skin [79, 80]. Perhaps the most influential and impactful advances in the application of skin grafts to human health was the idea of using skin grafts to treat the wounds of burn victims as introduced by Pollock in 1871 [79, 81]. This revelation resulted in an intense amount of research into the application of skin-grafting practices to enhance the success of healing large-scale dermal damage and overcome issues such as transplant rejection due to immune system response [79, 82]. Until recently, most advances in this area have been confined to repair and/or replacement of skin tissues.

The term “tissue engineering” was first confirmed in 1987 at a National Science Foundation bioengineering panel meeting which defined the term as “the application of the principles and methods of engineering and life sciences toward the fundamental understanding of structure-function relationships in normal and pathologic mammalian tissue and the development of biological substitutes to restore, maintain, or improve function” [83, 84]. Since this time, tissue engineering has emerged as a vast field of research. Numerous approaches have been developed to interface with biological systems

and engineer the growth of native tissues for both enhancement of tissue regeneration/replacement and development of platforms for exploring cell behavior and rapid drug discovery.

1.2.1 Tissue Engineering for Regenerative Medicine

Repair or replacement of damaged tissues *in vivo* is a primary focus of modern tissue engineering. The general aim is to introduce the appropriate biomaterials (i.e. cells, proteins, and other biological components) at the site of a damaged tissue in a way which encourages tissue regeneration and/or tissue repair. The most commonly successful method of tissue repair, which utilizes a tissue engineering approach, is the application of an artificial three-dimensional construct engineered from materials which, at minimum, allow for cell attachment and growth while having a limited impact on cell health. These engineered materials are commonly referred to as tissue engineering scaffolds and are typically comprised of organic polymers. As these materials are designed for direct integration into the host tissue, other important design factors must be considered including biocompatibility, mechanical properties, biodegradability, and mass transport properties such as diffusion of nutrients and metabolites [85-89].

1.2.2 Cell Sheet Engineering

Culture of tissues which have the capacity to be used *in vivo* without the need for implantation in tandem with synthetic materials has gained increased attention in the research arena. One strategy, which has recently met with considerable success, is the culture of cells into confluent cell sheets atop surfaces which allow for minimally invasive harvesting and translocation of the cultivated sheets. This process was first

realized by experiments using thin pNIPAAm film surfaces to selectively release cultured cells by Teruo Okano in the early 90's [44]. Since these first studies, this process has been used extensively to culture cells of numerous types and harvest cell sheets while maintaining cell/cell connections and interconnecting extracellular matrix intact [21, 43-45, 47, 48, 90-97].

This approach, referred to as "cell sheet engineering", has been extended one step further to generate multi-level micro-tissues via a stamping process. In short, micro-tissues are grown on responsive pNIPAAm surfaces, a gelatin stamp is used to collect the tissue after thermally initiated release by decreasing culture temperature, this is repeated for each subsequent micro-tissue sheet, and finally the multi-level tissue can be translocated to another surface and the gelatin can be removed by dissolution after resuming the temperature to that of standard culture conditions [98-100].

Although this process is widely applied and has significant room for expansion, cultivation, or release, of micro-tissues requires a significant drop in culture temperature ($\Delta T \approx 17°C$). Additionally, release is slow. This requires tissues to endure a low temperature environment for an extended period raising questions regarding cell health and physiological state post-harvest. It is unclear why such low temperatures are required for tissue release, but studies have shown that cell sheet release requires active metabolic cellular processes which may explain why release is slow [43, 46]. Also, sequential stacking of cell sheets to produce multi-level tissues requires the use of an intermediate surface which greatly increases exposure to sub-culture temperatures and increases the potential for mechanical disruption of the tissue and constituent cells.

1.2.3 Tissue Engineering as a Research Platform

In addition to direct therapeutic application of tissue engineering technologies, many tissue engineering-based strategies are used to evaluate cell-cell interactions, cell-extracellular matrix interactions, gene expression, and other important biological processes. These "research platforms" allow for a more rapid approach to biomaterial development, drug discovery, and acquisition of fundamental knowledge in cell biology and physiology [101-104]. The success of tissue engineering strategies to create such platforms hinges on the ability to construct *in vitro* tissue models which mimic native cellular environments and behaviors. Ideally, this calls for strategies which allow for control over cellular organization and development of three-dimensional tissues without integration of non-native components.

1.3 Research Motivation and Objectives

The aim of this research is to harness the non-uniform swelling behavior of confined, micron-scale, thermally responsive structures as a tool for tissue engineering. Evaluation of previous studies on confined, swellable, materials shows the capacity of these materials to form complex geometries by swelling of simple, easily fabricated, structures. This behavior, in tandem with the "switchable" properties of pNIPAAm materials, provides an attractive platform for development of surfaces which possess rapidly augmentable morphologies, through small temperature shifts, within a physiologically acceptable range. Previous studies have shown the capacity of grafted pNIPAAm surfaces to culture and harvest confluent micro-tissue sheets. Although this has met with much success in both experiment and clinical application, the process of cell

release is slow and requires very large shifts in culture temperature. This raises questions regarding the effects of prolonged low temperature exposure on cell health and physiological state. Additionally, translocation of tissues from these surfaces to form multi-layered tissue constructs is slow, increases duration of potential low temperature exposure, and requires the use of an intermediate transfer surface. This research focuses on addressing these concerns by harnessing the “Shape-shifting” nature of confined, micron-scale, structures for organized cell culture, rapid micro-tissue release, and direct stamping of organized micro-tissues.

First, swelling of micron-scale surface confined structures will be evaluated to identify the important parameters which dictate the general equilibrium structure after thermally-induced swelling. These results will be compared to an established linear elastic theory to determine agreement between experimentally measured post-swelling geometries and those predicted by the model. As previous studies have suggested, it is expected that the basic relationships from a linear elastic theory should be capable of approximating the swollen structure’s geometry although slight modifications may need to be made to the theory to account for swelling anisotropy without invoking a complex non-linear approach. Additionally, these experiments will help to elucidate the important parameters required to develop a shape-shifting surface for rapid release of organized micro-tissues.

The next phase of this study is designed to test the capacity for these surfaces to induce alignment in cells under culture conditions thus generating well-organized micro-tissues. Although culture on tall, micron-scale, pNIPAAm surfaces has not yet been demonstrated, it is expected that culture and alignment of cells will be successful as

previous studies have demonstrated cell culture on pNIPAAm surfaces and alignment by contact guidance has been shown to be purely a function of substrate geometry.

Upon successful culture of organized micro-tissues, it is expected that significant alteration of structure geometry due to a mild thermal shift ($\Delta T \approx 9°C$) will have a more rapid impact on cell release rates as no biological processes are required and release should be purely mechanical in nature. It is expected that micro-tissue release will be facilitated by shear stresses which arise between the shape-shifting surface and the overlying micro-tissue and can be directly correlated to the degree of surface deformation, or surface strain. This would be a more preferable mode of tissue release as cultured cells will be subject to a more mild decrease in culture temperature for a reduced period of time, ultimately minimizing impacts on cell health and physiological state.

The final aim of this research is to test the ability of the surfaces to directly stamp cells to a virgin surface. This effort is motivated by an attempt to develop a strategy which can be extended to the subsequent stamping of organized micro-tissues into complex multilayered micro-tissues without the need for an intermediate surface. These complex tissues can then be used as a model which more closely mimics the native cellular environment for use in tissue replacement and as an advanced platform for testing cell behavior or advanced drug discovery. Additionally, it is envisioned that this strategy may be extendable to an automated process for the fabrication of functional organs through a subsequent stamping strategy. This would have profound effects on the field of tissue engineering and provide a relevant avenue for organ replacement without the need of donor tissues.

Chapter 2: Materials and Methods

This chapter serves as a reference for all materials and methods used to accomplish the research outlined in this document.

2.1 Fabrication of poly(N-isopropylacrylamide) Structures

In general, pNIPAAm structures were formed by UV-initiated free radical polymerization in an acetone solvent within transparent molds atop glass coverslips treated with 3-(trichlorosilyl)propyl methacrylate (TPM) to ensure covalent binding, and thus mechanical confinement, of the structures to the glass surface during polymerization. Patterning of pNIPAAm structures was accomplished by using soft patterned polydimethylsiloxane (PDMS) molds formed by curing the PDMS atop of rigid patterns comprised of crosslinked SU-8 photoresist formed on a silicon wafer. The PDMS molds were then cut to isolate individual patterns, placed on TPM treated glass, filled with pre-polymer solution, and irradiated with UV light to initiate the free radical polymerization and formation of pNIPAAm patterned structures [49, 70]. A detailed schematic describing each of the fabrication steps involved in the formation of surface confined pNIPAAm structures on glass surfaces is provided in Figure 2-1. The following portions of this section will outline the previously described process of pNIPAAm structure formation in greater detail.

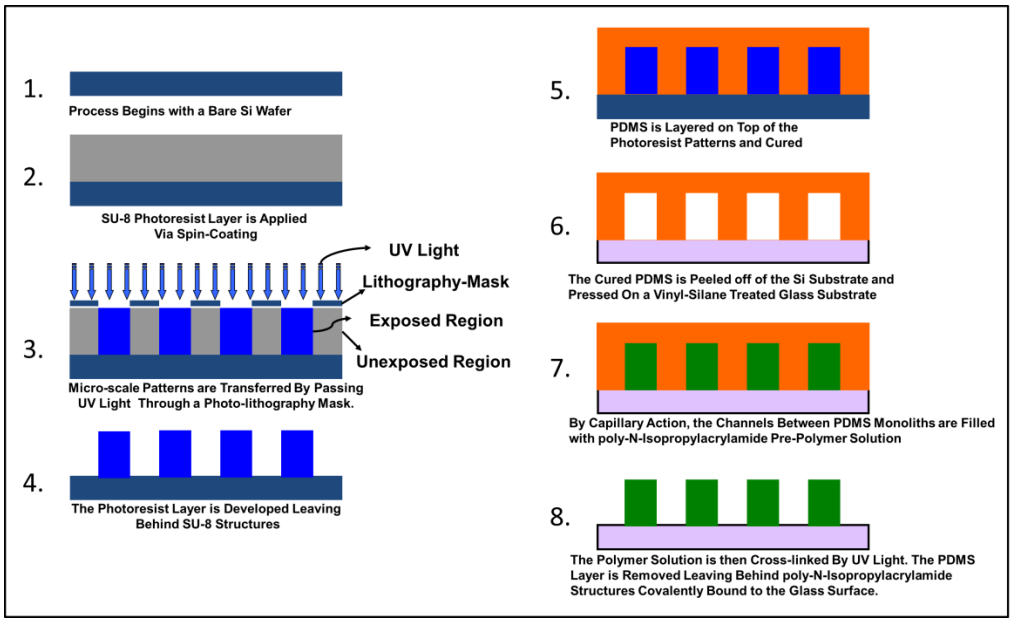

Figure 2-1: Process flow for fabrication of pNIPAAm structures

2.1.1 Design of Patterned Mask for Photolithography

Design of patterns which were to be translated into pNIPAAm structures began with the development of a chrome plated glass mask. Patterns that were transferred onto the glass mask were generated by use of AutoCAD software (Autodesk Inc.). Two-dimensional patterns were designed as arrays of long rectangular shapes, or beams, ranging from 1 - 5mm in length and from 5 - 100µm in width connected at both ends to large rectangular “pads”. For some patterns the width was varied across the beam length with the widest portion of the beam being at each terminus and the thinnest portion at the beam center. Varied width beams ranged from 40 - 100µm at the widest portion to 10µm at the thinnest. The large rectangular pads that bound each end of the beam patterns are included in the design to allow for easy visibility of the location of the pattern array as well as allow for an easy cutting point to allow for formation of capillaries which become important during the pre-polymer filling step described later. The general format of the

mask design and a close-up of a typical pattern array are provided in Figure 2-2. Mask designs were then patterned onto chrome plated glass masks manufactured by Advanced Reproductions, Inc. (Andover, MA).

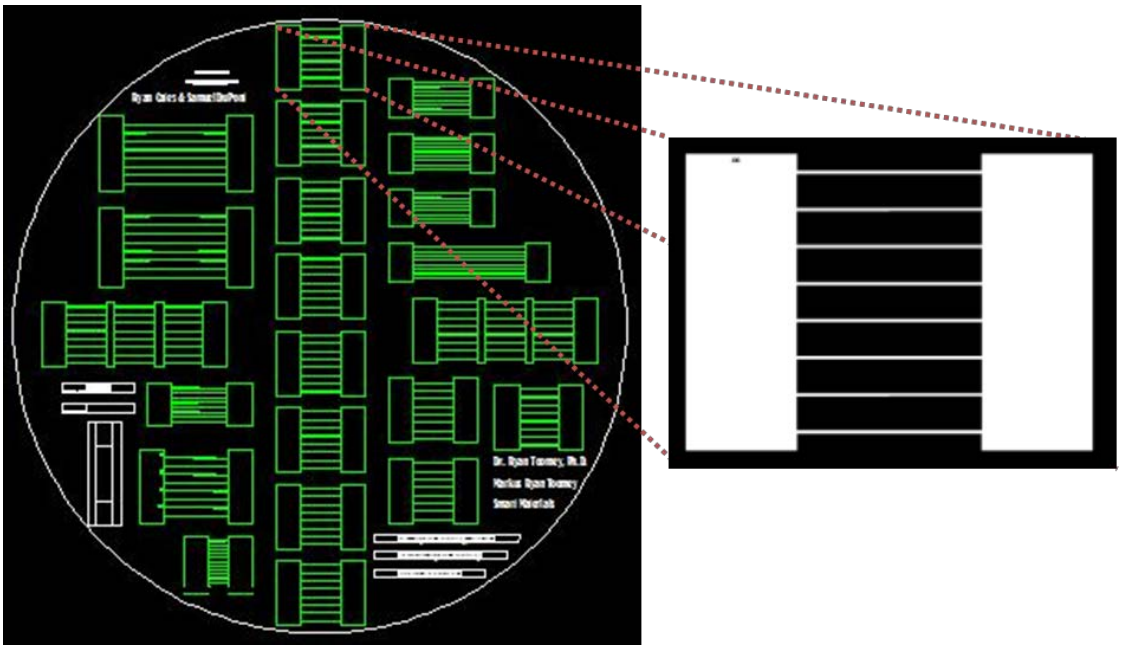

Figure 2-2: Sample schematic of a mask design for multiple pattern arrays including a close-up of a typical pattern array bounded by large rectangular pads.

2.1.2 Formation of Structures on Silicon

Two-dimensional patterns were transferred from chrome plated masks to three-dimensional structures on a silicon (Si) base via photolithography. In most cases, patterns were transferred into an epoxy-based photoresist (SU-8) designed for fabrication of micron-scale high aspect ratio structures. To achieve pattern transfer into the SU-8 material, 4” Si wafers were first cleaned through submersion in a freshly mixed 3:1 (volumetric) solution of sulphuric acid (H_2SO_4) and hydrogen peroxide (H_2O_2) for 15 minutes. This solution, sometimes referred to as a “piranha etch” undergoes a very

exothermic reaction and the formation of atomic oxygen which acts to remove, by oxidization, any organic contaminates on the Si surface. After removal of Si wafers from the piranha etch solution and rinsing in deionized water, the Si wafers were then dehydrated in an oven at 250°C for 30 minutes to ensure removal of excess water. The Si wafers were then coated with a negative SU-8 photoresist (MichroChem) by placing ~4mL of SU-8 solution in the wafer center and spin casting the photoresist on a Laurell spin coater (North Wales, PA). The thickness of SU-8 films, and ultimately the thickness of the pattern, was modulated by altering the viscosity of the SU-8 resist (SU-8 2025, SU-8 2035, and SU-8 2050) and spin-casting rotational velocity as recommended by the vendor. Film thickness ranging from 10μm to 60μm were achieved and verified using a Tencor alphastep 200 profilometer. Excess solvent was evolved from the film surface by performing a two-step soft bake on a level hotplate starting at 65°C for 3 minutes followed by baking at 95°C for 7 minutes. Patterns were transferred into the SU-8 film by using the previously described masks fitted into a Carl Suss Mask Aligner and a long pass Hoya UV-34 filter to remove UV radiation below 350nm. Exposure times varied depending on the film thickness and lamp intensity as suggested by the manufacturer (although it is important to note that dosages were increased by ~30% to accommodate loss of UV radiation due to application of the log pass UV filter). After UV exposure, Si wafers were again heated on a level hotplate by performing a two-step post exposure bake for 2 minutes at 65°C and 7 minutes at 95°C. Removal of uncrosslinked SU-8 material was performed by developing the samples under constant agitation in a bath of SU-8 developer (MicroChem) for durations recommended by the manufacturer. During the development process, development times were fine tuned for each sample by

constantly monitoring sample development using an optical microscope. After development was complete, samples were briefly rinsed in fresh SU-8 developer followed by rinsing with isopropyl alcohol. Samples were dried using dry N_2 and finally baked at 250°C for 30 minutes to cure the SU-8 structures increasing their mechanical strength and adhesion to the Si surface.

For structures having thicknesses (perpendicular to the Si surface) of between 1µm - 5µm, patterns were formed from a Shipley 1813 photoresist (Rhom and Haas) using a similar procedure to the procedure outlined above and following manufacturer's recommended conditions.

2.1.3 Formation of PDMS Molds

Negatives of SU-8 patterns were patterned into polydimethylsiloxane (PDMS) using a Sylgard® 184 silicone elastomer kit (Dow Corning). PDMS was mixed in a small plastic dish at 10:1 mass ratio of elastomer to curing agent and rigorously mixed for 3 minutes. Mixed PDMS was placed under vacuum for approximately 20 minutes to degas all trapped air bubbles which resulted from the rigorous mixing. PDMS was then poured over the surface of a level, preheated (65°C), Si wafer containing SU-8 patterns and allowed to cure for 1 hour. It takes approximately 20g of uncured PDMS mixture to fully cover the surface of the 4" Si wafer without spilling over the edge while still maintaining a thick PDMS film. After curing was complete PDMS films were allowed to cool on the Si wafers for 1 hour and then carefully removed with tweezers. The negatively patterned PDMS films were immediately placed in 150mm polystyrene dishes for storage to prevent contamination of the underlying PDMS surface.

2.1.4 Glass Coverslip Preparation

Glass coverslip substrates (~170μm thick) were surface modified with 3-(trichlorosilyl)propyl methacrylate (TPM, Sigma-Aldrich) using standard protocols [105]. The surfaces are treated with TPM to form a monolayer of vinyl groups on the glass surface. These vinyl groups participate in the free radical polymerization causing polymer chains at the surface to form covalent bonds to the surface and effectively anchoring the pNIPAAm patterned structures. Prior to TPM treatment, glass coverslips were cleaned by oxygen plasma treatment with either a Harrick PDC-32G plasma cleaner at 6.8W and 500mtorr for 15 minutes or a PE50 (Plasma Etch, Carson City, NV) using an oxygen plasma at 100W for 5 minutes. Cleaned coverslips were then submerged in a 1mM TPM solution in 4:1 heptane to carbon tetrachloride for 20 minutes followed by a five minute rinse in hexane and a subsequent five minute rinse in deionized water. The entire TPM treatment process, including addition of TPM to the heptane/carbon tetrachloride solution, was carried out in a N_2 environment contained in a plastic glove bag. After treatment, TPM treated glass coverslips were dried with a jet of N_2 gas and stored in a covered 35mm polystyrene petri dish stored under vacuum.

2.1.5 pNIPAAm Pre-Polymer Solution

The primary components in the pre-polymer solution include the primary monomer N-isopropylacrylamide (NIPAAm, 97%, Sigma-Aldrich), the crosslinking monomer N,N'-methylenebisacrylamide (BisAAm, Sigma-Aldrich), the photoinitiator 2-dimethoxy-2-phenylacetophenone (DMPA, Sigma-Aldrich), and in order to facilitate visualization using fluorescence and confocal microscopy the fluorescent monomer

polyfluor 570 (Methacryloxyethyl thiocarbonyl Rhodamine B) (Polysciences, Inc). Pre-polymer components were solvated and mixed in an acetone solution at the following concentrations: 200mg/mL NIPAAm, 2mg/mL DMPA, 1mg/mL polyfluor 570, while the concentration of BisAAm was adjusted between 2mg/mL and 8mg/mL to alter the overall crosslink density of the final polymer material. Additionally, to facilitate pNIPAAm hydrogels which have significantly increased swellability some samples were prepared with Acrylic Acid (AAc) ranging from 0 – 20% (by mass). To remove any dissolved oxygen which may interfere with the free-radical polymerization N_2 was bubbled through the solution in a N_2 environment prior to polymerization.

2.1.6 Polymerization of pNIPAAm Structures

In order to form patterned pNIPAAm structures a commonly employed soft lithography technique, micromolding in capillaries (MIMIC), was performed through customization of standard protocols [106-108]. Previously described PDMS pattern molds were cut from the PDMS film. Cuts were made perpendicular to the long axis of the rectangular beam patterns through the center of the rectangular pads which bound the patterned beams as shown in Figure 2-3. By making these cuts, small capillaries are revealed at each end of the pattern to allow fluid flow and filling of the PDMS mold with pre-polymer solution. Cut PDMS patterns are placed in good contact on TPM treated glass coverslips. In a N_2 atmosphere contained in a plastic glove bag, 10µL of pre-polymer solution (described above) is placed at one of the open edges of the PDMS causing the PDMS mold to be filled with pre-polymer solution due to capillary action. Immediately the filled molds are exposed to UV radiation (γ = 365nm) for 4 minutes to

initiate polymer formation by free radical polymerization. Following polymerization, samples are removed from the N_2 atmosphere and allowed to cool due to heating from UV exposure. After cooling, PDMS molds are gently removed revealing three-dimensional pNIPAAm patterns which are covalently bound to the glass surface. Excess polymer surrounding the intended pattern is removed by gentle scraping with a razor blade and samples are stored for pending analysis.

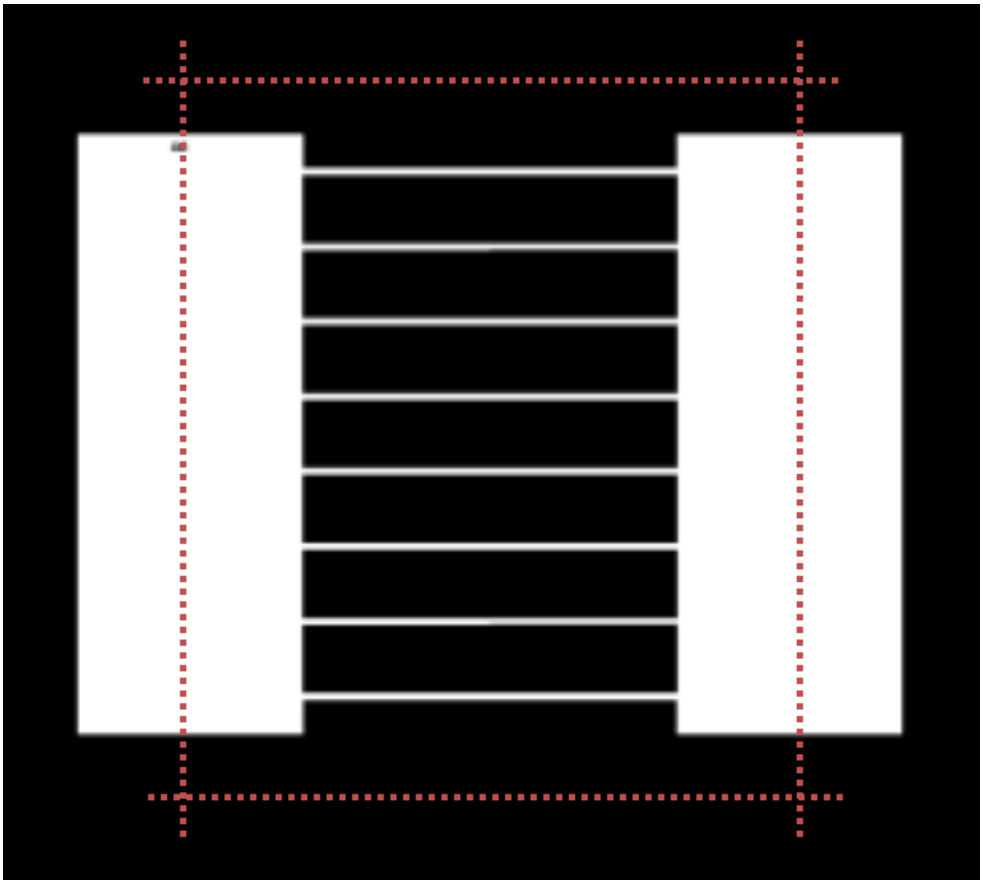

Figure 2-3: Schematic showing where cuts are made (red dotted line) to remove patterned array from PDMS film and opening capillary inlets at each end of the array for fluid flow.

2.2 Swelling Experiments

Typical swelling experiments involving pNIPAAm structures were performed using deionized water at room temperature (~27°C). For microscopy where imaging of pNIPAAm structures in the collapsed state was required, deionized water heated to ~50°C was used and temperature was maintained using a heat gun. For swelling of pNIPAAm-co-AAc samples a sodium hydroxide solution (pH = 8.5) was used to ensure complete ionization and maximum swelling of the gel. Swelling ratios were determined by either comparing the swollen height to the collapsed height $\alpha_h = \frac{h_{swollen}}{h_{collapsed}}$ of confined structures by image analysis of confocal acquired cross-sections or by breaking the structure from the surface and measuring the degree of elongation of the unconfined structure. Equilibrium swelling was accomplished by removing individual beams from the glass surface by delicate scraping using a handheld razor. The degree of swelling was measured by: $\alpha_{eq} = \frac{l}{l_0}$, where α_{eq} is the equilibrium elongation ratio and l is the length in the swollen state and l_0 is the length in the collapsed state. The results of α_{eq} for various crosslink densities and AAc concentrations are provided in Figure 3-4.

2.2.1 Swelling with NaCl

In order to induce controlled collapse of swollen pNIPAAm structures sodium chloride (NaCl) was used in concentrations ranging from 0 – 5M as NaCl has been shown to influence the LCST of pNIPAAm gels [109]. Tests involving addition of NaCl salt were performed at room temperature (~27°C). Samples were first submerged in a 5M NaCl solution and the salt concentration was incrementally reduced by dilution of the solution.

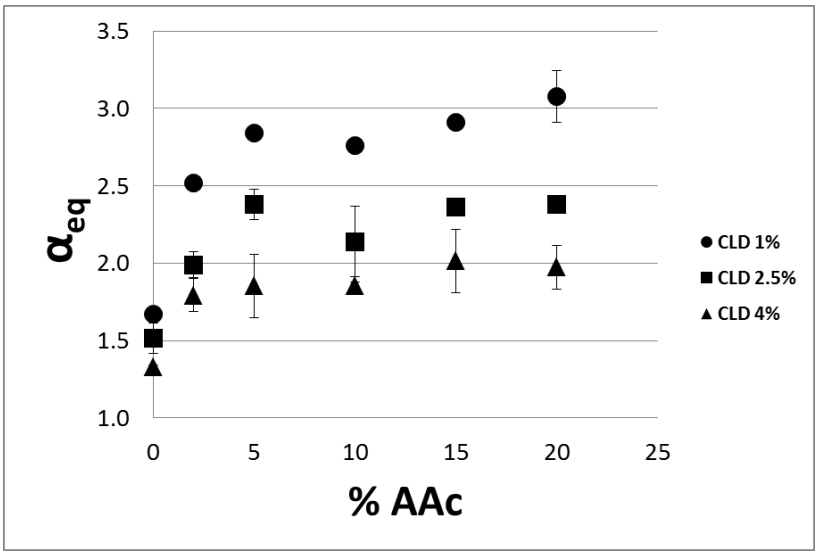

Figure 2-4: Elongation ratio for various polymerization conditions. Error bars represent one standard deviation.

2.2.2 Alcohol Swelling

The swelling ratio of pNIPAAm gels has been shown to be sensitive to solvent type [110]. As another method of controlling the swellability of pNIPAAm structures the following solvents were applied to the samples: Methanol (MeOH), Ethanol (EtOH), and n-Butanol (n-But).

2.3 Cell Culture

2.3.1 General Cell Culture

NIH3T3 murine fibroblasts (American Type Culture Collection, Manassas, VA) were maintained by culturing in complete growth media (CGM) containing 10% newborn calf serum (NCS), 1% penicillin-streptomycin (PS), and 89% Dulbecco's Modified Eagle's Medium (DMEM)) on regular tissue culture polystyrene (TCPS) dishes (Fisher) in a humidified incubator at 37°C and 5% CO2. Cells were passaged after cultured cell plates reached >80% confluency (typically after 2-3 days). Passaging of the

cells was performed by first enzymatically removing cells from the culture surface by treatment with 2mL of 0.5% trypsin/EDTA (Invitrogen) for 5 minutes after removal of CGM and rinsing with 10mL of Dulbecco's phosphate-buffered saline (DPBS) solution lacking calcium and magnesium ions (Ca(-)/Mg(-)). Enzymatically removed cells are then diluted in fresh CGM for a final dilution of 1:4 and then plated on fresh TCPS dishes for incubation. Cells were maintained between passage numbers 5 – 25. Upon reaching higher passage numbers a fresh cell line was cultured from cells stored in liquid N_2 to maintain availability of healthy cells.

2.3.2 Preparation of pNIPAAm Surfaces for Cell Culture

For culture-based experiments pNIPAAm was patterned on 22mm x 22mm glass coverslips. Coverslips containing pNIPAAm patterns were adhered to the bottom of 35mm TCPS dishes with a thin layer of PDMS to ensure immobilization of the glass coverslip during culture and microscopy. To accomplish this approximately 100µL of uncured PDMS (10:1 elastomer to curing agent) was applied to the underside of patterned coverslips and then placed in the center of a 35mm TCPS dish. Dishes were then cured in an oven at 65°C for 60 minutes on a level surface.

2.3.3 Sterilization of pNIPAAm Surfaces for Cell Culture

Patterned pNIPAAm surfaces were prepared for cell culture by a rinsing and sterilization process which ensured removal of excess unpolymerized monomer and deactivation of any biological contamination. This process included three 2 minute rinses in deionized water followed by a 5 minute rinse in a 80% ethanol solution, and finally

two 2 minute rinses in DPBS which included calcium and magnesium ions (Ca(+)/Mg(+)). Samples were air dried and kept sterile until cell seeding.

2.3.4 Cell Culture on pNIPAAm Structures

Cells from nearly confluent cultures (~80%) were used for seeding on pNIPAAm surfaces. Cells were enzymatically removed from TCPS plates as previously described. Removed cells were transferred into a 50mL conical centrifuge tube and diluted to 10mL final volume with fresh CGM. Cells were then centrifuged to separate cells from the trypsin/EDTA contaminated media and resuspended in CGM to reach the desired cell density for seeding. TCPS dishes containing pNIPAAm surfaces were seeded with 2.5mL of the cell suspension and immediately transferred to an incubator where samples were incubated under typical culture conditions. Seeding densities ranged from 500 cells/mm^2 to 1000 cells/mm^2. Samples were incubated between 12 and 96hrs depending on the experiment. For cells incubated greater than 48 hours media was replaced (75%) being sure to maintain sample temperature above 32°C. Dimensions of high aspect ratio pNIPAAm beams, for formation of cell fibers, were of 10-20μm in width and 20-30μm in height with a spacing of 1000μm between beams. Dimensions of straight and curved pNIPAAm structures, for formation of cellular ribbons, were 50-100μm in width and 20-30μm in height. Two groups of closely spaced pNIPAAm beam arrays were fabricated with dimensions for group 1 and group 2 of 4μm and 8μm widths and a beam spacing of 9μm and 12μm respectively, both having a height of 0.8μm as measured by atomic force microscopy in contact mode using a XE-100 AFM purchased from PSIA.

2.3.5 Cell Staining

In order to visualize cells for alignment analysis and to determine cell viability cells were stained with a 2μM solution of Calcein-AM (Invitrogen) in DPBS for 30 minutes. To prevent thermal actuation of the pNIPAAm surface all staining was performed at 37°C. For differential staining of cellular components following cell printing, cells were permeabilized with ice cold 0.5% Triton X-100 in complete DPBS for 10 min and fixed in 3.7% formaldehyde for 5 min and stained with Alexa Fluor® 488 C5 Maleimide (Invitrogen) and Hoechst-33242 (Histo-Line Laboratories).

2.4 Micro-Tissue Release

Micro tissue release was performed on cells grown between 16 and 24 hours. Samples containing organized micro-tissues were removed from the incubator and immediately placed on a microscope for large format imaging of the sample before thermal actuation of the surface. Organized micro-tissues grown atop of pNIPAAm structures were released from the surface by thermally induced swelling of the underlying pNIPAAm structures. This was accomplished by reducing the sample temperature to ~28°C through addition of 1 mL of ice cold DPBS Ca(+)/Mg(+). Sample surfaces were imaged 3- 5 minutes after swelling to determine the degree of cell detachment.

2.4.1 Strain Induced Detachment

Swelling of pNIPAAm structures results in a significant increase in the surface area of the structure's upper surface. In order to determine how this affects release of organized micro-tissues, the strain of pNIPAAm surfaces was modified by augmenting

the crosslink density through altering the concentration of BisAAm during pNIPAAm preparation. The concentration of BisAAm was altered by adjusting the polymerization chemistry from 1% – 4% which resulted in structures with exhibited swelling induced surface strains ranging from 0.1 to 0.7. Surface strain was calculated in the following manner:

$$e = \frac{\Delta w}{w_{collapsed}} = \frac{w_{swollen} - w_{collapsed}}{w_{collapsed}}$$

where e is the Cauchy strain, $w_{collapsed}$ is the width of the pNIPAAm beam in the collapsed state and $w_{swollen}$ is the width of the pNIPAAm beam in the swollen state.

2.4.2 Chemical Treatment of Cells on pNIPAAm Structures

In order to elucidate the mechanism of cell detachment from pNIPAAm surfaces, samples were treated with either sodium azide (NaN_3, Sigma-Aldrich) a compound known to decrease ATP production or Y-27632 (Sigma-Aldrich) a selective inhibitor of Rho-associated protein kinases [111, 112]. Seeded samples incubated for greater than 16 hours were treated with either sodium azide dissolved in 500µL of fresh CGM for a final sample concentration of 2mM or Y-27632 dissolved in fresh CGM for a final sample concentration of 50µM [43, 113]. Samples treated with Y-27632 were treated for at least 30 minutes prior to analysis and cells treated with sodium azide were treated for at least 60 minutes prior to analysis. In both cases treatments were performed under standard cell culture conditions until microscopic analysis. Testing of the effects these treatments had on cell release was performed in the same manner as standard cell release tests were performed.

2.5 Micro-Tissue Stamping

Organized micro-tissues formed on pNIPAAm surfaces were stamped on to PDMS films treated with human plasma fibronectin (Invitrogen). To ensure that PDMS surfaces were flat, PDMS films were cured (10:1 ratio of elastomer to curing agent) by pouring approximately 50g of the elastomer mixture (after removal of trapped air by vacuum treatment) onto a 4” Si wafer placed in the center of a 150mm polystyrene dish. The PDMS films were cured in an oven at 65°C for one hour and then allowed to cool at room temperature. Using a razor, the portion of the PDMS film that was atop the Si wafer was removed and small 1x1cm squares were cut. PDMS squares were then incubated with fibronectin (10µg/mL in DPBS) for 1 hour prior to stamping. Cell culture on pNIPAAm structures which had formed organized micro-tissues were removed from incubation and PDMS squares were placed over the pattern area and gently placed in contact with the pNIPAAm patterns. A 20g weight was gently placed atop the PDMS square to ensure good contact between the PDMS and pNIPAAm surface. Immediately 1mL of ice cold DPBS was added to induce swelling of the pNIPAAm structures, and thus release of the organized micro-tissue. After thermal activation of the pNIPAAm surface the PDMS stamp was allowed to remain in contact with the sample surface for 5 minutes to allow formation of new contacts between the organized micro-tissue and the receiving PDMS surface. After incubation, the 20g weight and the PDMS were gently removed and microscopy was performed on the PDMS square to image the stamped micro-tissue.

2.6 Microscopy

2.6.1 Sample Preparation for Microscopy

For bright field, phase contrast, and standard fluorescence microscopy samples were used as either glass coverslips of glass coverslips adhered to the bottom of 35mm TCPS dishes as described previously and without further modification. Samples used for analysis via confocal microscopy were prepared differently to accommodate the shorter working distance and narrow depth of field associated with the objectives used on these microscopes. In order to allow for sufficient submersion of the sample in solvent while maintaining a reduced thickness through which the objective must focus a "fluid cell" was fabricated. The design was fabricated around 75mm x 25mm coverslips containing pNIPAAm patterns as shown in Figure 2-5. Glass coverslips were joined to a piece of poly(methyl methacrylate) (PMMA) by three small rubber support rings and two larger fluid containment rings. All pieces were adhered using standard clear nail polish. Two ports were drilled into the PMMA backing of the cell to allow for injection of solvent and sealed with standard translucent tape to prevent leakage.

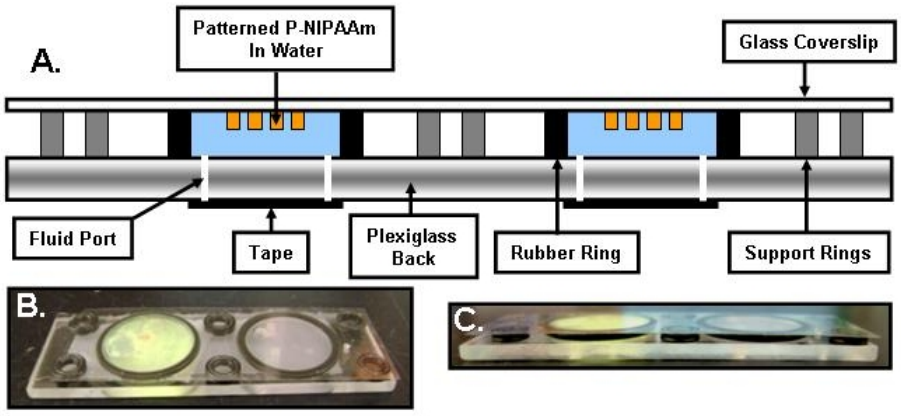

Figure 2-5: Schematic of the cross-section of a typical fluid cell (a) used for imaging of pNIPAAm structures on an upright confocal microscope. Actual images of the fluid cell are shown from both the objective side (b) and the fluid cell profile (c).

2.6.2 Bright Field, Phase Contrast, and Fluorescence Microscopy

Imaging of pNIPAAm structures and cell culture was performed at 4X, 10X and 40X with a Nikon eclipse Ti-U fluorescent microscope (Nikon Instruments, Melville, N.Y.) fitted with a motorized stage and NIS-Elements Advanced Research software (Nikon Instruments) using phase contrast or DIC for bright field images and fluorescence filters for selectively imaging rhodamine illuminated pNIPAAm beams and fluorescently labeled cells. In some cases, large format images were taken by using an imaging collection and stitching algorithm to rapidly capture large areas of a sample's surface while maintaining good resolution. Time lapse images were taken as a video file with a frame rate of 8 fps.

2.6.3 Confocal Microscopy

During the process of this research confocal microscopy was performed to collect images for thin slice fluorescence investigation of pNIPAAm structures and acquisition of X-Y image stacks for three-dimensional reconstruction of pNIPAAm structures using two types of confocal microscopes. For image acquisition where rapid imaging was required (for instance, collection of X-Y image stacks for three-dimensional reconstruction of an actively swelling gel) digital images were collected on a Zeiss Axiovert 200 fitted with a Perkin Elmer UltraVIEW ERS confocal imaging system based on the Nipkow spinning disc design using a 568 nm excitation laser with a cyan /red emission filter. Additionally, high resolution images were captured with a Leica TCS SP5 confocal laser scanning microscope (CLSM) with 20×/0.7NA and 40×/1.25NA objectives (Leica Microsystems, Germany). An Argon laser line, tuned to 543nm, was applied to excite the fluorescent pNIPAAm gels and an AOBS was used to filter the

emission. Image sections were taken at a constant z-spacing ranging from 0.25 μm to 1 μm and captured with photomultiplier detectors using the LAS AF software version 2.1.0 (Leica Microsystems, Germany). To induce collapse of pNIPAAm gel structures and capture time-based image stacks of the gel swelling, heat was applied to elevate the fluid temperature. Image stacks were sequentially taken as the water cooled resulting in the capture of image stacks during mid-transition. Time between X-Y image stacks varied depending on gel thickness and height with an average interval of approximately 20sec. Due to the requirement of rapid image capture all time-based image stacks were acquired from the Zeiss spinning disc confocal microscope.

Measurements were taken with a 20× air lens and a 40× oil lens, both of which produce aberrations in the vertical height due to mismatches in refractive index between the microscope objective and sample. Corrections for the refractive index mismatch were estimated by performing z-axis measurements of the dry and swollen polymer patterns with each objective. As the thickness must be the same with both objectives, a suitable correction factor was generated for each objective. The thicknesses of dry patterns were further verified with a Tencor Alphastep 200 Automatic Step Profiler. In the case of swollen gels, application of a previously described technique for estimation of a correction factor was performed [(114)]. The correction factors applied to z-axis measurements ranged from 0.8 to 1.4.

2.6.4 Localized Fluorescent Quenching

Fluorescence quenching tests were performed to elucidate the internal deformations of swelling pNIPAAm gels using a series of area of interest (AOI) tools in

the Leica software with the Leica CLSM. The laser was set to scan repeatedly over the AOIs until a reasonable reduction in fluorescent signal was achieved. Scans were taken over an 8hr period for low aspect ratio structures and a 2hr period for the high aspect ratio buckling structures. Image contrast and brightness modifications were made to maximize contrast between over exposed areas and the bulk of the structure.

2.7 Image Analysis

2.7.1 Swelling pNIPAAm Gels

Image stacks were rendered and analyzed using the Imaris 5.5.0 (Bitplane, Inc., St. Paul, Minnesota) software package to generate rotatable 3D objects. Raw image stacks were loaded into the software and background fluorescence was removed by thresholding and the resultant image stack was used to render iso-surfaces. X-Y image stacks were converted into X-Z image stacks using ImageJ v1.38x (NIH, USA). Distance measurements of all structures were made using Image-Pro Plus v6.2.0.424 (Media Cybernetics, Inc.). Pattern peripheries were determined by appropriate thresholding values and measurements of length, width, and thickness, were made to characterize the pattern cross-sections. Variations in pattern path-length and amplitude (irregular off-axis swelling) for buckling and wrinkling structures were measured using X-Y plane images at subsequent Z positions.

2.7.2 Cell Culture

Images acquired by microscopy were segmented via mono thresholding in NIS-Elements Advanced Research software v3.1 to determine alignment of individual cells. Objects segmented by intensity thresholding were subsequently separated using the

separation algorithm in the NIS-Elements software and alignment was determined by the orientation of the max-ferret diameter with respect to the orientation of the underlining SE array. Cell alignment data was normalized according to the orientation of the underlying pNIPAAm SE such that the SE axis was consistently at 0° or 90°. For alignment measurements, at least three samples were used for analysis for each of the investigated geometries including measurement of cells grown on glass controls. Analysis of images used to determine cell detachment where thresholded to increase contrast of individual cell bodies. Cell area was determined before swelling and 3 minutes after swelling by outlining cell bodies and calculating the aggregate cell are over the portion of the surface evaluated. In the post-swollen state, only cells which had not detached from the surface were included in the area calculation. Cell attachment was determined by comparing pre and post states. Cells which remained significantly spread on the surface were counted as attached. Some images acquired were contrasted to enhance distinguishing features and all enhancements were applied evenly throughout the entire field of the image.

Chapter 3: Swelling-Induced Instabilities in Confined pNIPAAm Structures[1]

This chapter focuses on non-uniform deformations which occur in confined materials capable of swelling due to solvent uptake. In order to establish the nomenclature and parameters presented in this chapter a schematic of a confined rectangular structure is presented in Figure 3-1 where the height of the structure (h) is the dimension perpendicular to the confining surface and extends along the z-axis, the width of the structure (w) is in a plane parallel to the attachment plane and extends along the x-axis, and the length (L) of the structure is in a plane parallel to the attachment plane and extends along the y-axis.

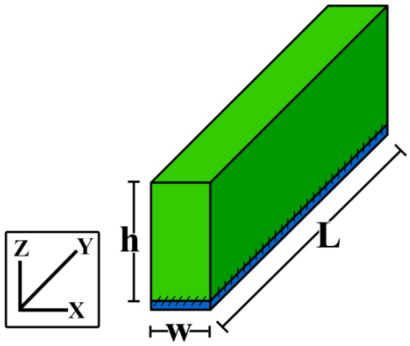

Figure 3-1: Schematic of the basic dimensions of a rectangular structure (green) confined to a rigid surface (blue). The geometric measurements of width (w), height (h), and length (L) are shown along the x, z, and y axes respectively.

[1] Portions of these results have been previously published (DuPont et al., 2010) and reproduced by permission of The Royal Society of Chemistry.

3.1 Confinement of Swelling Structures

The human body is comprised of a variety of diverse tissue types which each perform a specific, and essential, biological function ensuring the autonomy of a living system. Although supported by a rigid skeleton, nearly 80% of the human body mass is comprised of soft materials [115]. These materials are composed of numerous cell types which comprise functional tissues and protein structures which mechanically interact to allow biochemically driven processes to perform discrete functions contributing to the sustainability of the autonomous biological system. Soft materials are an emergent field in material science as their mechanical properties provide a unique platform for understanding and interfacing with biological systems. Native soft materials in a biological system are generally subject to mechanical constraints which are essential to their biological function. These constraints invoke a rich range of material geometry and behavior providing the capacity for complex motion and function. A few examples include the structure of brain gyri, the alveolar membrane in the lung, and smooth muscle in the esophagus [116-118]. In fact, disruption of these mechanical constraints can cause a change to the tissue morphology and lead to the onset of disease [119]. This provides motivation for understanding the behavior of soft materials in a mechanically constrained environment such that a greater understanding of these relationships can be derived.

Stimuli-responsive materials are a class of soft materials which provide unique flexibility in experiment and application. This flexibility is provided by the unique ability of these materials to change their properties in response to changes in their chemical and mechanical environment [4, 11, 13, 15, 120, 121]. Typically, these materials are hydrogels which interact with an aqueous environment such that water penetrates the material causing a

change in the material's geometry through a volumetric expansion [122-124]. Due to their responsive nature, the degree of water penetration can be dictated by external stimuli, providing a mechanism for enhanced control over the rate and degree of the volumetric expansion. Equilibrium of the volumetric expansion, or swelling, is dictated by two competing mechanisms. Expansion of the hydrogel, due to osmotic driven penetration of solvent, is balanced by the elasticity of the interconnected polymer chains which comprise it. Swelling of the gel continues until the solvent induced osmotic pressures both inside and outside the gel are balanced. When a gel is not influenced by any outside forces, such as confinement to a rigid surface, swelling is homogeneous and the final shape of the gel is an isotropic expansion of the initial geometry. Swelling under the influence of a mechanical constraint, however, reduces the dimensions available for expansion and leads to the formation of anisotropic stresses in the gel which results in a final shape very different from the initial geometry. This "shape-shifting" nature can provide enhanced flexibility in engineering design with applications in numerous fields [70, 125].

When a bulk hydrogel is exposed to a good solvent the initial phases of swelling can lead to the formation of non-uniformities or surface instabilities in the transient gel structure, if the swelling ratio of the gel is great enough. This was first described in an acrylamide gel by Tanaka et al [68]. Although non-uniformities arise during the swelling process, the non-uniformities fade as gel swelling approaches equilibrium and the resultant hydrogel has the same proportional geometry as the original gel although the volume has dramatically increased. When a portion of a bulk hydrogel is clamped or confined to a rigid surface, something very different occurs. Upon swelling, the clamped

hydrogel forms similar non-uniformities as in the unconfined case but these non-uniformities persist even after swelling equilibrium. These non-uniformities can result from a combination of both global and local differential swelling and is directly associated with the confinement of the material to a rigid surface [49, 64, 66, 67, 69, 71, 73, 126].

The physical manifestation of the swelling instability caused by differential swelling is strongly associated with the initial geometry of the material. For instance, a thin film comprised of a swellable material confined to a rigid substrate can lead to the formation of a wrinkled surface upon swelling. In contrast, a high aspect ratio beam-like structure can form an off-plane bulk buckling instability which arises due to its confinement to the rigid surface.

In an attempt to describe the formation of an off-plane buckling instability which arises due to swelling of a soft acrylamide gel bound to a stiff non-swelling surface, Mora et al. investigated the application of the Föppl–von Kármán equations for thin elastic plates [66]. The model developed was formed within the restraints of linear elastic theory such that there is a linear dependence between the in-plane stress tensor and the deformation tensor. The model developed in this study describes a buckling wavelength (λ) which arises due to compressive stresses generated in the gel along the y-axis due to confinement. In general, as the gel swells a compressive stress begins to accumulate in the gel due restricted lengthening along the y-axis. This stress, which can be described as a non-dimensional compressive stress (P), reaches a critical value $P_c = 10.4$ which results in a critical wave number $q_c = 1.39$, the point at which P(q) is minimum and represents the minimum P required to cause an instability in the structure. This results in bending which leads to buckling of the structure. This analysis yielded two critical relationships

which describe the onset and length-scale of the buckling instability. First, this model suggests that the wavelength of the buckling instability is dependent upon the height (h) of the structure only such that:

$$\lambda = \frac{2\pi}{q_c} = 3.256h \qquad \text{(Eq. 3.1)}$$

Additionally, the critical strain (k_c) at which the structure becomes unstable leading to bulk structural buckling is a function of the aspect ratio ($AR = \frac{h}{w}$) and the non-dimensional compressive stress such that:

$$k_c = \frac{P_c w^2}{12h^2} = 0.867\frac{w^2}{h^2} \qquad \text{(Eq. 3.2)}$$

The general assumptions which arise in the framework of the linear elastic theory include the assumption of low magnitude strains as well as a linear relationship between stress and strain. Within this framework, and for values of k_c between 0.15 and 0.8, it was shown that swelling of thin acrylamide strips agreed well with the model.

Another study aimed to explore buckling in thin nanometer-scale pNIPAAm lines. Tirumala et al. first recognized the formation of "wriggles" in nanometer-scale pNIPAAm lines fabricated by a novel direct e-beam polymerization technique [127]. Later, a model was adapted from a framework developed to describe the formation of different shapes during leaf growth [69, 72]. In this model, a scaling relationship similar to that presented by Mora et al. was defined to address the onset of a bulk buckling type instability where the critical differential swelling strain (β^*) is proportional to $\frac{1}{AR^2}$ such that $\beta^* \sim \frac{w^2}{h^2}$. Although the scaling relationship is similar, the compressive stress which is defined to dictate the onset of the instability differs from the previous model as β^* is defined along the structure's width as opposed to its length.

3.2 Non-Uniform Swelling of Confined pNIPAAm Structures

The primary aim of this chapter is to evaluate the effects of confinement on the swelling of pNIPAAm structures of various geometries. The structures presented here consist of a rectangular geometry similar to that shown in the schematic in Figure 3-1. Primarily, pNIPAAm structure widths and heights are modulated in confined structures having very long lengths. The aim is to test the formation of confinement-induced instabilities which arise due to swelling of the structure. Structures designed of pNIPAAm offer a good platform for understanding these phenomena as they can easily be patterned on the micron-scale for direct observation and measurement by microscopy. Additionally, the swelling can be controlled by numerous approaches such as cross-link density, gel ionization, solvent quality, salt concentration, and temperature. Also, direct observations of the three-dimensional structure can be made through incorporation of a fluorescent monomer and confocal microscopy. The following sections will outline the results acquired by swelling pNIPAAm structures with various chemistries, geometries, and solvent conditions in an effort to understand the behavior of these structures and gain further insight into the incorporation of these materials in engineering design.

3.2.1 Forms of Confinement-Induced Swelling Instabilities

Throughout this research four primary forms of instabilities were observed in confined pNIPAAm materials: bulk structural buckling, differential lateral swelling, localized edge buckling, and surface wrinkling. Images collected by confocal microscopy were used to reconstruct the three dimensional geometry of these instabilities, an example of each is provided in Figure 3-2. Formation of each of these instabilities depends

strongly on the geometry of the pNIPAAm structure. Bulk buckling is observed in high aspect ratio rectangular structures, both differential lateral swelling and localized edge buckling is observed in low aspect ratio rectangular structures, and surface wrinkling on both thick and thin structures of considerable lateral dimensions.

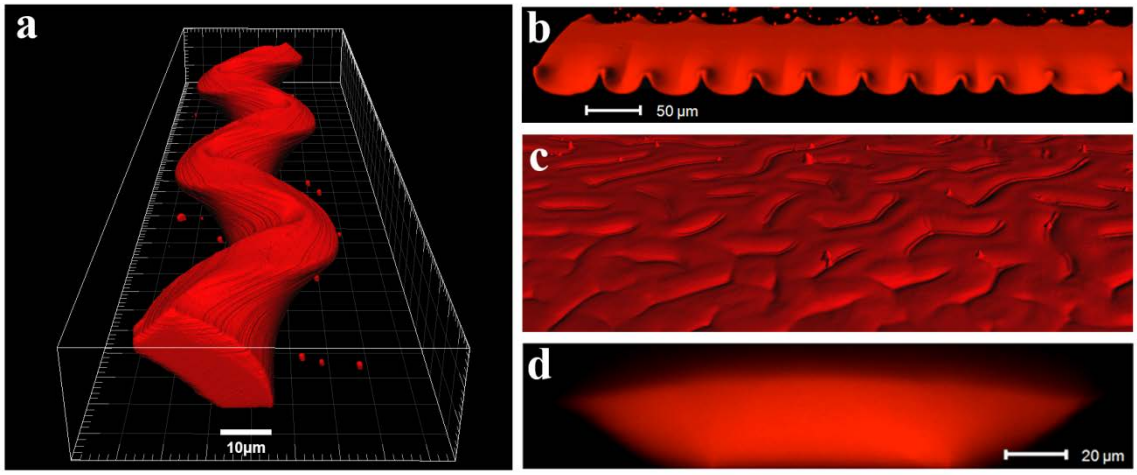

Figure 3-2: The four primary forms of confinement induced instabilities which arise from swelling of pNIPAAm surfaces. Image stacks acquired by confocal microscopy were used to recreate the three-dimensional geometry of bulk buckling (a), localized edge buckling (b), and surface wrinkling (c) and a cross-sectional profile to show differential lateral swelling [(49)].

3.2.2 Onset of Instabilities in pNIPAAm Structures

From general experimental observations it is recognized that the emergence of a bulk buckling instability is a function of geometry and the degree of compressive stress accumulated within the gel. To test the geometric and mechanical conditions which lead to bulk buckling in micron-scale pNIPAAm structures gel swelling was modulated through a combination of gel ionization by inclusion of acrylic acid during polymerization and alterations of cross-link density. Additionally, surface confined pNIPAAm structures were fabricated having constant height and a gradient in width

along the length of the structure. This provides a convenient way to test the effect of aspect ratio as the structure will have a gradient of aspect ratios. An image of such a structure is provided in Figure 3-3 where the structure height is 21.4μm ±3.0μm and the gradient in width ranges from 100μm to 10μm resulting in an aspect ratio gradient ranging from 0.21 to 2.1.

These structures were designed to decrease in width with an angle of -0.4° with respect to the structure's center axis. The resulting dimensionless width gradient and aspect ratio gradient for these structures is: $\frac{dw}{dL} = -1.4 \times 10^{-2}$ and $\frac{dAR}{dL} = 2.9 \times 10^{-4}$ respectively. The width gradient is negative as the width is decreasing along the y-axis which leads to an increasing aspect ratio gradient.

Swelling of descending width pNIPAAm structures was performed on a series of surface confined gels fabricated with various degrees of swelling. The degree of swelling was calculated as the elongation ratio (α) and was measured by detaching a portion of a structure from a constant width sample fabricated under identical conditions and measuring the length in the dry state (L_0) and the swollen state (L). With these data values of α were calculated by:

$$\alpha = \frac{L}{L_0} \qquad \text{(Eq. 3.3)}$$

Swelling was performed on constant height, descending width, structures over various degrees of swelling with α ranging from 1.3 to 3.2. At values of α exceeding 3.2 analysis was difficult as swelling of the pNIPAAm structures led to delamination from the surface therefore this was chosen as the upper bound for these tests. Upon swelling of descending width structures a distinct transition marking the onset of bulk buckling was observed in every sample. Figure 3-4 shows images of two descending width structures

of different degrees of swelling where bulk buckling is seen on the right portion of each image.

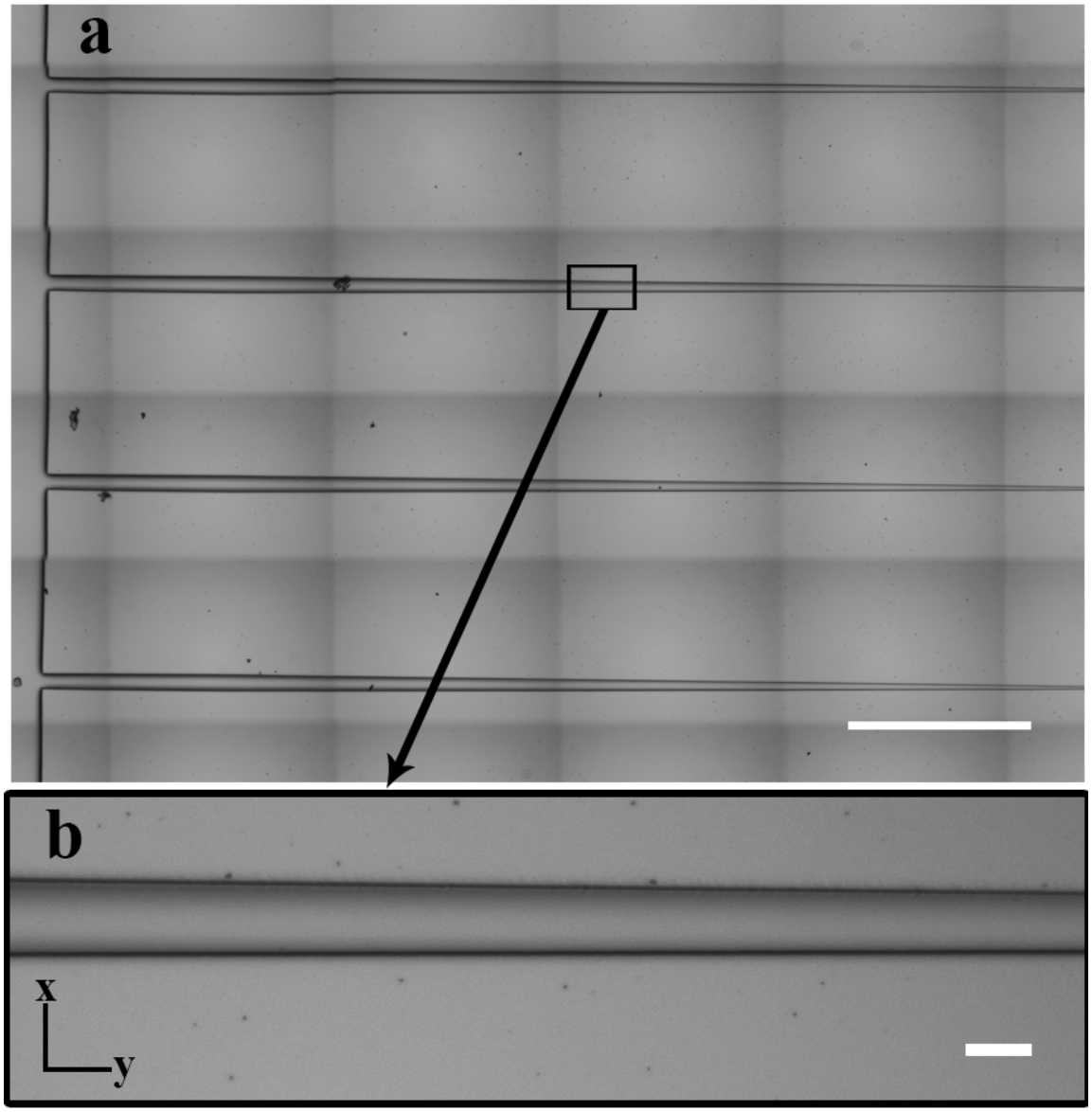

Figure 3-3: Example of a descending width pNIPAAm structure array (a) and a close-up of a segment (b). Size bars represent 1,000μm (a) and 50μm (b).

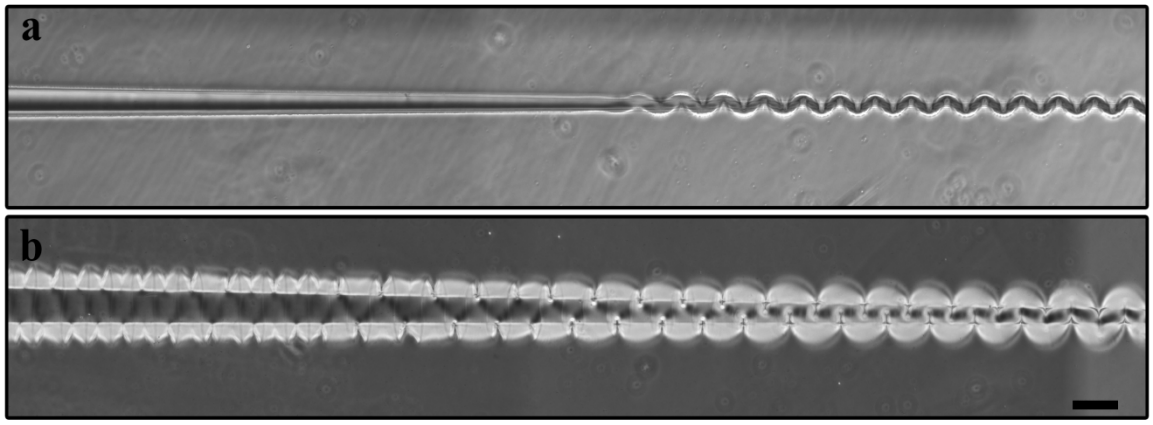

Figure 3-4: Phase contrast images of surface confined, descending width, pNIPAAm structures post-swelling. (a) a structure with a low degree of swelling ($\alpha = 1.33$) and (b) a high degree of swelling ($\alpha = 2.14$). Size bar represents 100μm.

The images presented in Figure 3-4 not only demonstrate the onset of bulk buckling but also reveal four primary instabilities: bulk buckling, localized edge buckling, differential lateral swelling, and surface wrinkling. Confined pNIPAAm structures which exhibit a low degree of swelling (Figure 3-4a) show a sharp transition between bulk buckling (right) and differential lateral swelling (left). Meanwhile, structures which exhibit a high degree of swelling (Figure 3-4b) show well-formed bulk buckling (far right) but the transition to differential lateral swelling (far left) is non-uniform, occurs over a long range, and includes the emergence of localized edge buckling and surface wrinkling.

In all samples there was found to be two distinct points in the transition between differential lateral swelling and bulk buckling as the transition occurred over a range of structure widths. For structures where swelling results in a low elongation ratio the transition region was typically less than the length of a single wavelength in the bulk buckling region and the difference between the width of the structure at each point in the transition was minimal and therefore the aspect ratio at the transition was similar. In

contrast, structures which swell with a large elongation ratio exhibited a transition which existed over a long range of widths therefore the aspect ratio was significantly different at each end of the transition. As there was no known precedence for distinguishing between these two primary forms of instability the following rules were established to clarify the transition region from regions of pure differential lateral swelling or bulk buckling. Images outlining the defined transition regions for a high elongation ratio structure are provided in Figure 3-5. Bulk buckling was defined as a structure in which non-uniform deformations lead to structural bending where points on the edge of the bulk structure cross over the central axis of the confinement region at the greatest degree of x-axis deformation. Defining the onset of differential lateral swelling in low elongation ratio gels is simple as this is the region where bulk buckling is absent. In higher elongation ratio gels this is less straightforward because in addition to differential lateral swelling, localized edge buckling and surface wrinkling instabilities arise. Qualitatively, the transition from the bulk buckling region and the differential lateral swelling region in high elongation ratio structures begins when the arch of the buckles begin to squeeze into one another and bending across the bulk of the structure slowly fades as the structure width increases resulting in a structure possessing a more cusp-like external geometry. Furthermore, as the width continues to increase these cusp-like structures begin to press into one another resulting in the formation of edge cusps with a shorter length scale. This final pattern remains consistent as width continues to increase, this is the region defined as differential lateral swelling. In a later section the three-dimensional geometry of these cusps is explored revealing the formation of localized edge buckling.

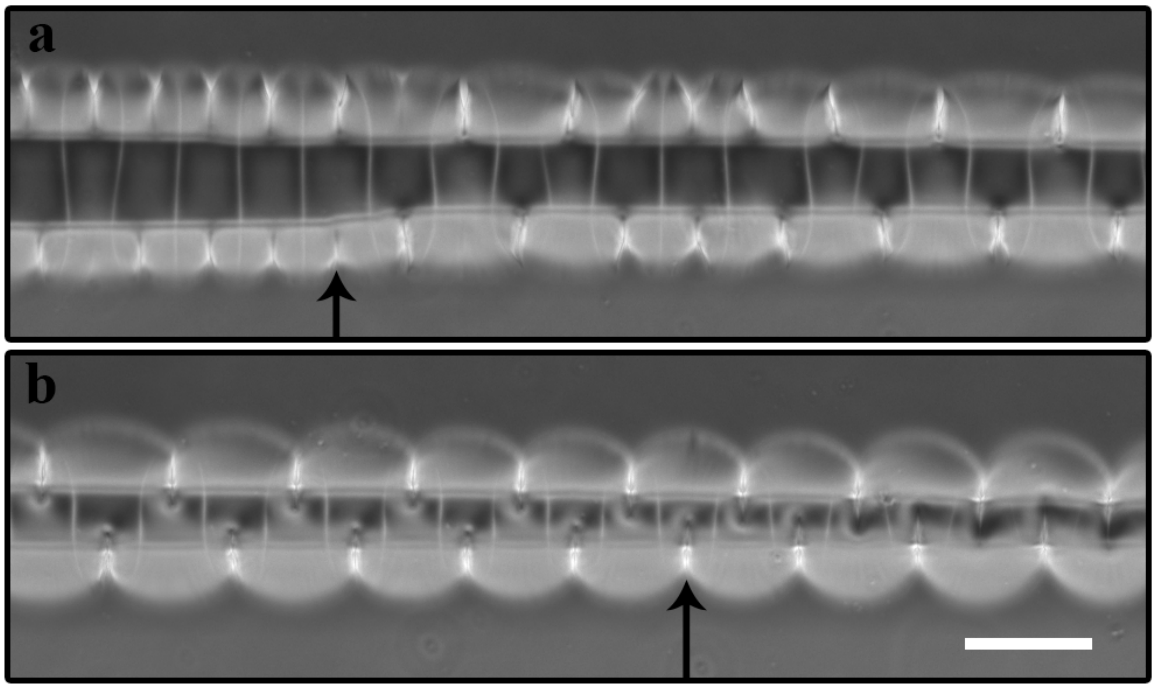

Figure 3-5: Arrows representing the locations assigned to the onset of (a) differential lateral swelling and (b) bulk buckling. Images taken from a descending width structure having an elongation ratio of $\alpha = 2.36$. The size bar represents 100μm.

Previous studies have suggested that the onset of bulk buckling occurs at a critical aspect ratio depending on the degree of swelling induced deformation [66, 69]. To test agreement of the micron-scale pNIPAAm structures with these models, data was collected by observing the bulk buckling transition in descending width structures and measuring the aspect ratio of the dry gel at that point. Figure 3-6 presents the results of this analysis. The data presented here represents the aspect ratio at the onset of pure bulk buckling and its dependence on the degree of swelling represented by the elongation ratio. In general this data suggests that structure aspect ratio must be high in order for bulk buckling to occur in a structure with a low degree of swelling expressed by a low elongation ratio. Furthermore, as the degree of swelling increases the aspect ratio at which bulk buckling is observed is reduced drastically. In fact, it appears that below an

elongation ratio of approximately 1.9 the aspect ratio required to induce bulk buckling rapidly increases.

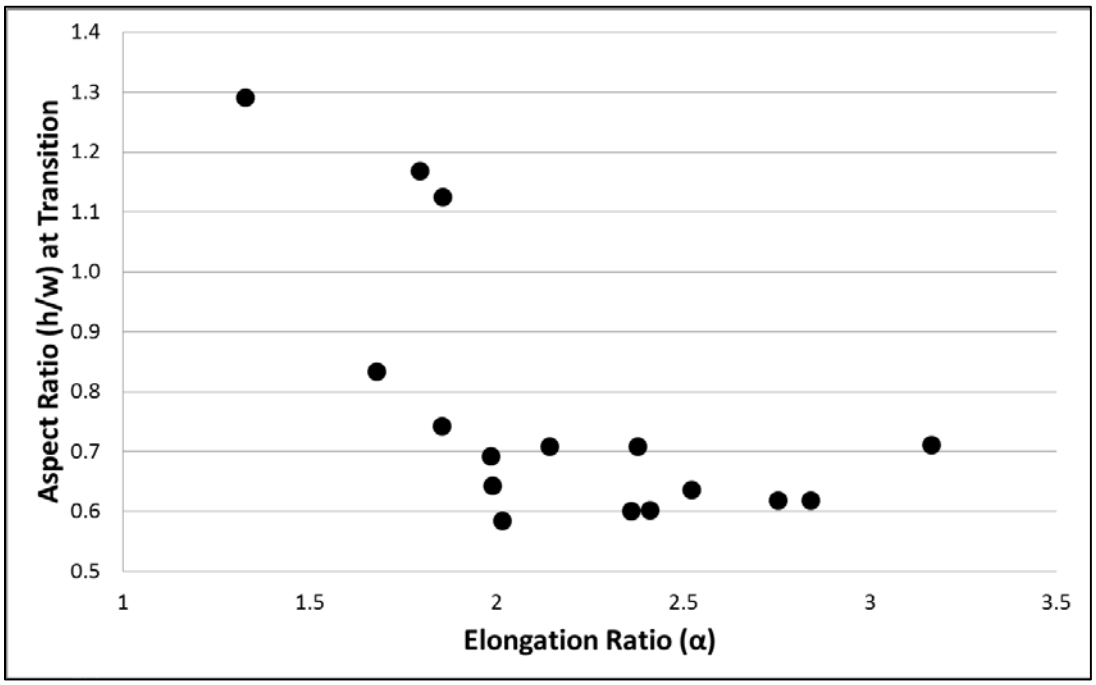

Figure 3-6: Plot of the aspect ratio of descending width pNIPAAm structures at the onset of pure bulk buckling as a function of the elongation ratio (α).

Figure 3-7 presents data describing the relationship between the elongation ratio and the onset of differential lateral swelling. The trend here is very similar to that described for aspect ratio data at the onset of bulk buckling except the aspect ratio at which the transition begins is significantly lower, especially at higher degrees of swelling.

Data from each extreme of the transition were linearized and plotted (Figure 3-8) in the form of:

$$\left(\frac{1}{AR}\right)^2 = f(\alpha - 1) \qquad \text{(Eq. 3.4)}$$

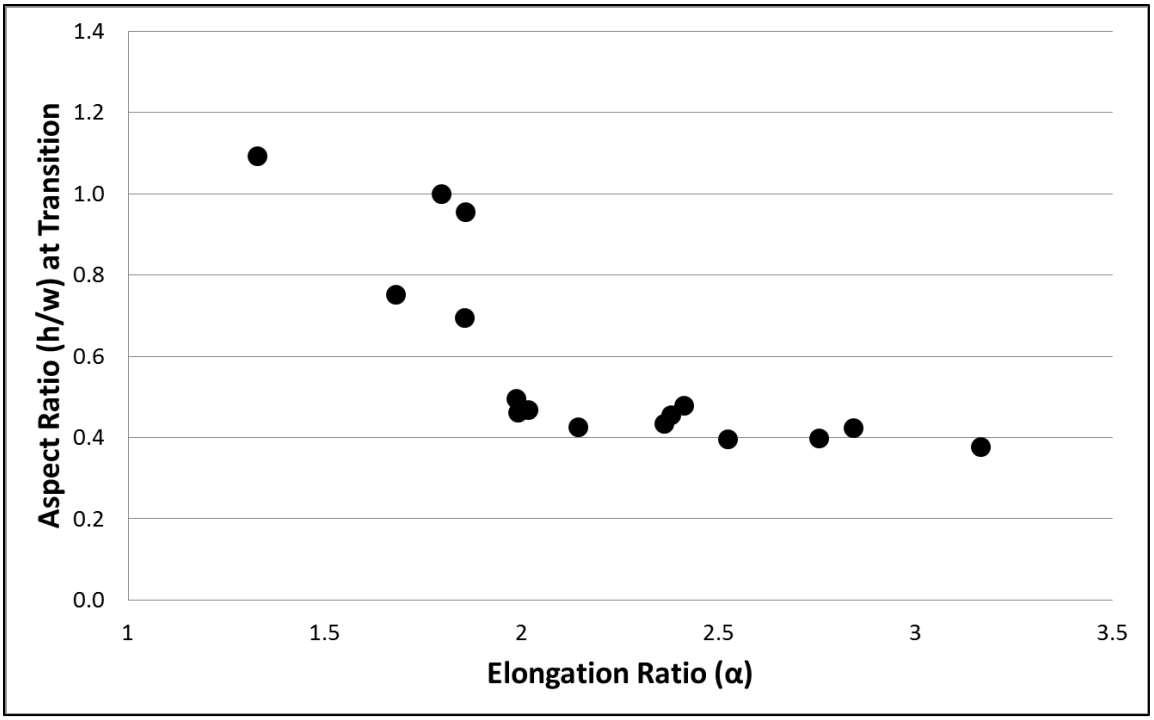

Figure 3-7: Plot of the aspect ratio of descending width pNIPAAm structures at the onset of differential lateral swelling as a function of the elongation ratio (α).

This was performed to directly compare these results to predictions from the model developed by Mora et al. where $k_c = \alpha - 1$ and $\frac{w^2}{h^2} = \left(\frac{1}{AR}\right)^2$. According to this model, the slopes of the plots presented in Figure 3-8 represent the quantity $\frac{P_c}{12}$ where P_c, as defined earlier, is the critical, non-dimensional, compressive stress acting along the length of the structure capable of overcoming the energy required to bend the structure and thus induce a bulk buckling instability. In the study it was found that under the assumptions of the linear elastic model the first lowest value of P(q) for which a wavenumber (q) can exist occurs at $P_c = 10.40$ and therefore the theoretical slope would be 0.867.

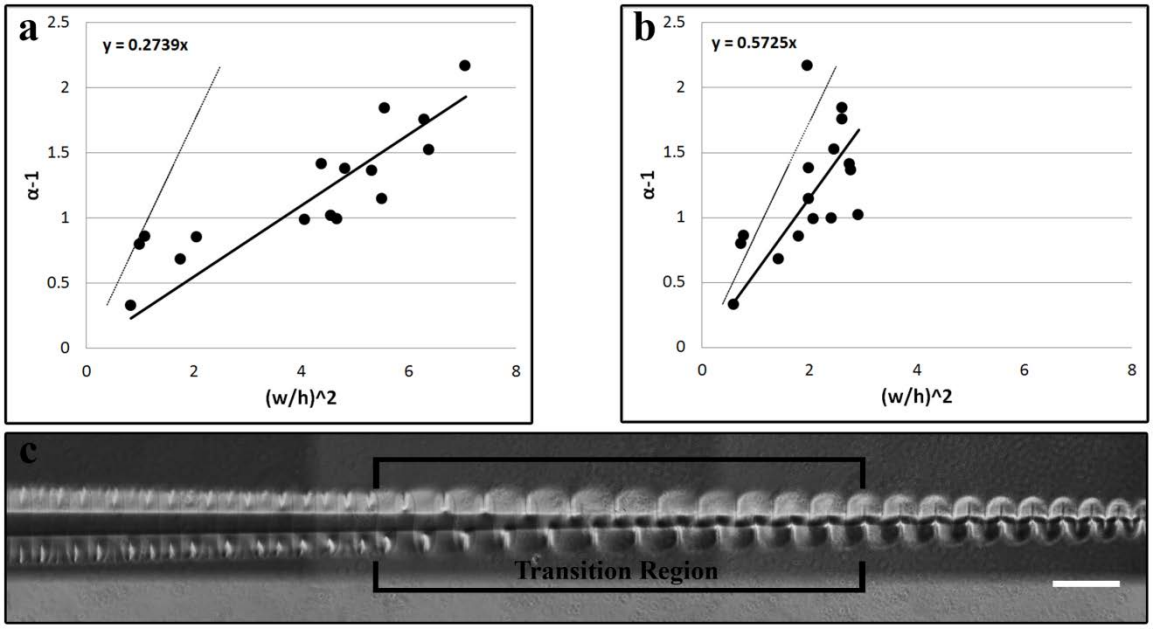

Figure 3-8: Data from descending width pNIPAAm structures of various degrees of swelling plotted to compare results with a model developed by Mora et al. (dotted lines) [66]. Plots were generated from data acquired at the onset of differential lateral swelling (a) and the onset of bulk buckling (b) which are shown in the left and right portions (respectively) on a structure (c) possessing an extended transition region and having an elongation ratio of $\alpha = 2.76$. Size bar represents 200μm.

The data presented in Figure 3-8 shows the comparison of data collected at the onset of differential lateral swelling (Figure 3-8a) and bulk buckling (Figure 3-8b) to the predictions of the Mora model. Most interestingly, data acquired at the onset of differential lateral swelling is fairly linear within the framework of the Mora model suggesting that the general relationship between variables associated with predicting the onset of buckling may also hold in predicting the onset of other instabilities such as localized edge buckling. The discrepancy between these data and the linear model may be explained by changes in the effective aspect ratio at the early stages of swelling resulting in an aspect ratio at the onset of the instability which is significantly different than that measured in the dry state. This could be caused by elongation of the structure height at a

rate which exceeds elongation across the structure width prior to the destabilization of the structure and the onset of bending.

To better understand the transition between local and global buckling, a descending width structure of constant height in the dry state (40μm) was evaluated (Figure 3-9). The elongation ratio for this structure was $\alpha = 2$. Confocal microscopy was used to measure the swollen height of the structure after swelling. Upon swelling, a transition from local buckling to global buckling was observed at a width of 55μm and the maximum height of the structure was roughly 96μm. Linear elastic theory predicts that the transition into bulk buckling for this structure would occur at AR = 0.93 or a structure width of ~43μm. If the dry height is used as a reference, the point at which the transition occurs is at AR = 0.73 and if the swollen height is used as a reference the transition occurs at AR = 1.7. Interestingly, the predicted AR lies between the dry and swollen height references. This suggests that the location of the transition point may be accurately described by the linear theory and the discrepancy could be explained by formation of the instability at some point mid-swelling. When performing these swelling tests, gel swelling is typically observed for a short period before the emergence of any noticeable instability. Therefore it could be plausible that the transition marking the onset of bulk buckling could be determined at a mid-swelling geometry where increases in structure height grow at a rate which is greater than increases in structure width until the critical criteria are met. It would make sense for this to be the case as confinement affects stretching across the structure width but has little impact on stretching perpendicular to the confining surface. Using the dry width at the transition as a reference, this would suggest that the transition point in the gel described above may have been determined at a

point in mid-swelling where the gel reached a critical height of approximately 51μm, or 20% of total swelling.

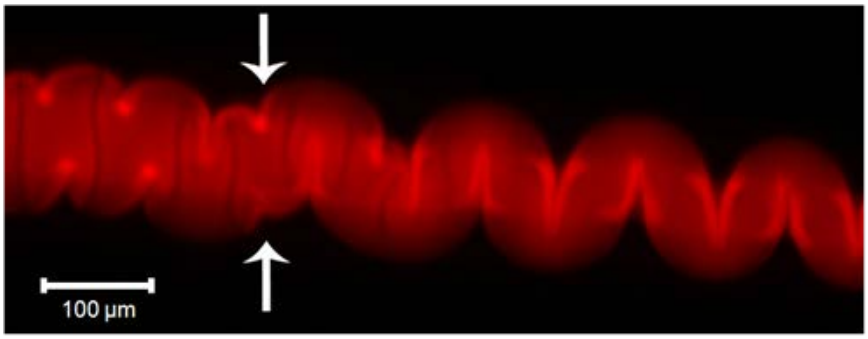

Figure 3-9: Fluorescence microscopy image of a descending width pNIPAAm structure ($\alpha = 2$) at the onset of buckling (arrows) [49].

One final result from this analysis involves the appearance of localized edge buckling and surface wrinkling in descending width structures. As previously shown in Figure 3-4, the emergence of buckling occurs at specified widths as a function of both elongation ratio and aspect ratio, but emergence of localized edge buckling and surface wrinkling appears to be either present or seemingly absent. After evaluation of these structures over a range of elongation ratios it was observed that only structures which possessed an elongation ratio of $\alpha > 2.0$ exhibited profound localized edge buckling and surface wrinkling while structures having $\alpha < 1.9$ exhibited differential lateral swelling and presence of localized edge buckling was either absent or at an extremely diminished length scale which gradually increased with increasing width while surface wrinkling was not observed. Another interesting result is presented in Figure 3-10 where a constant width structure having an elongation ratio of $\alpha = 2.4$ shows the formation of both surface

wrinkling and localized edge buckling (Figure 3-10a) which rapidly disappear as the gel buckles and reaches equilibrium swelling (Figure 3-10b).

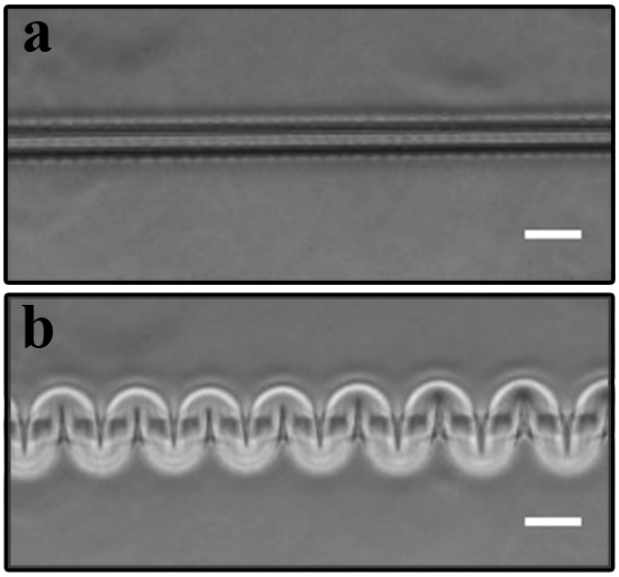

Figure 3-10: Phase contrast images of a constant width pNIPAAm structure (30μm width, dry) with an elongation ratio of $\alpha = 2.4$ in the initial stages of swelling (a), exhibiting localized edge buckling and surface wrinkling, and at equilibrium swelling (b), exhibiting bulk buckling. Size bar represents 50μm.

Although it is unclear exactly how these instabilities may be related, in cases of low degree of swelling this phenomenon is not observed and may suggest that this is the result of swelling kinetics and is dependent upon swelling rate as gels with a greater equilibrium swelling ratio will exhibit more rapid deformation rates in the early stages of swelling as it is a diffusion controlled process [128, 129].

3.2.3 Bulk Buckling of pNIPAAm Structures

For swelling of a structure possessing a sufficient aspect ratio and degree of swelling a bulk buckling instability arises leading to in-plane bending of the bulk

structure. The general characteristics which can be used to define such a structure are similar to those which describe waves. A buckled structure will possess a wavelength and amplitude. Also, the degree of change in path length and structure width can give insights into the geometry of the buckled structure. In this section a combination of fluorescence, phase contrast, and confocal microscopy was used to query the three-dimensional geometry of buckled pNIPAAm structures (Figure 3-11).

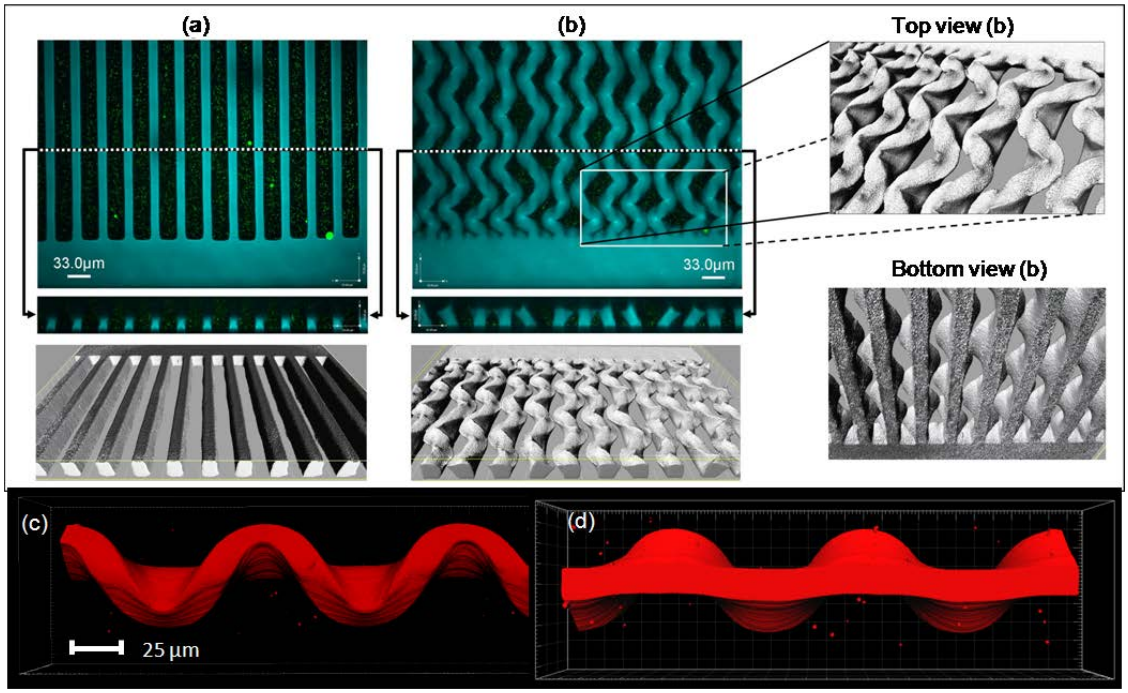

Figure 3-11: An array of pNIPAAm structures in the collapsed state (a) which experience bulk buckling upon swelling (b) due to surface confinement. Top (c) and bottom (d) views of a small buckled segment [49].

In the previous section, data collected testing the onset of buckling was compared to a linear elastic model and found to be similar in nature although some discrepancies did arise. Mora et al. applied a linear elastic model to buckling in thin polymer strips and found that the first wavelength to become stable is $\lambda = 3.2h$, where h is the structure

height [66]. To further test the validity of the linear model, in regards to instabilities which arise in confined pNIPAAm structures, the buckling wavelength at a variety of structure heights was measured. The relationship between the characteristic wavelength as a function of both the dry and swollen height was plotted and compared to the theoretical prediction in Figure 3-12.

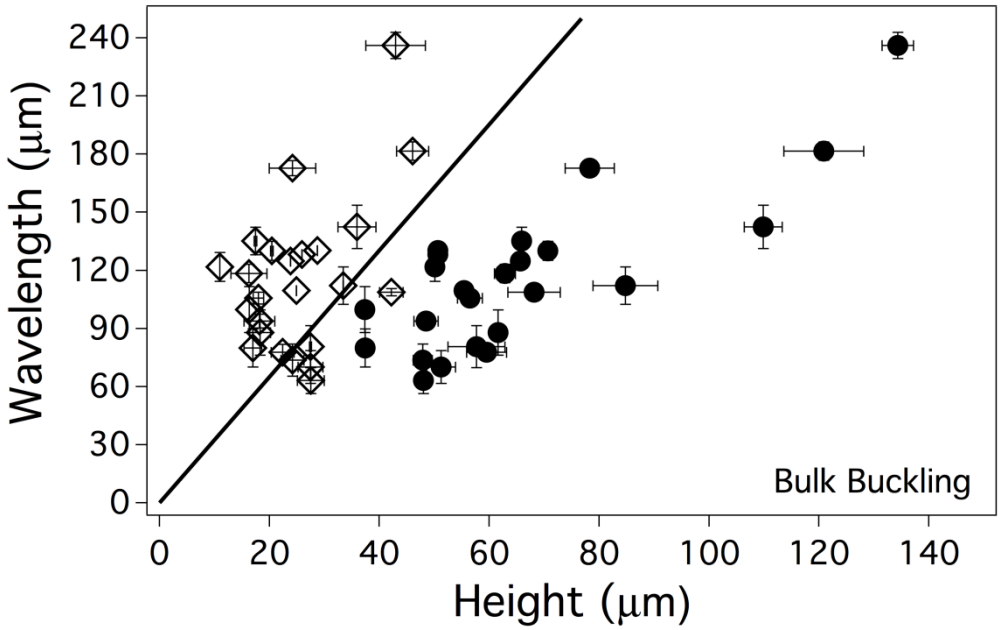

Figure 3-12: Relationship between the characteristic wavelength in globally buckled structures with reference to the dry structure height (◊) and the swollen structure height (●). The solid line represents the theoretical relationship ($\lambda = 3.2h$) given by linear elastic theory [66]. Error bars represent one standard deviation [49].

From the data presented in Figure 3-12 it appears that although the wavelengths measured with respect to both the dry structure height and swollen structure height appear to follow a trend similar to the linear elastic model there is a discrete difference between the two measurements. Most data referenced to the dry structure height show a characteristic wavelength much greater than predicted by the linear theory while data

referenced by the swollen height possess a wavelength much less than predicted. As was observed in the previous section, it appears that the geometry which dictates the characteristics of the buckled structure may be attained at some point in mid-swelling. This may suggest that the degree of swelling may play a role in determining this mid-transition geometry. Swelling was measured in pNIPAAm structures by comparing the dry height (h_d) to the maximum swollen height (h_s), to determine the swell ratio, and plotted against the resultant wavelengths. The data presented in Figure 3-13 shows these results on three separate plots where each plot represents a specific range of measured swell ratios.

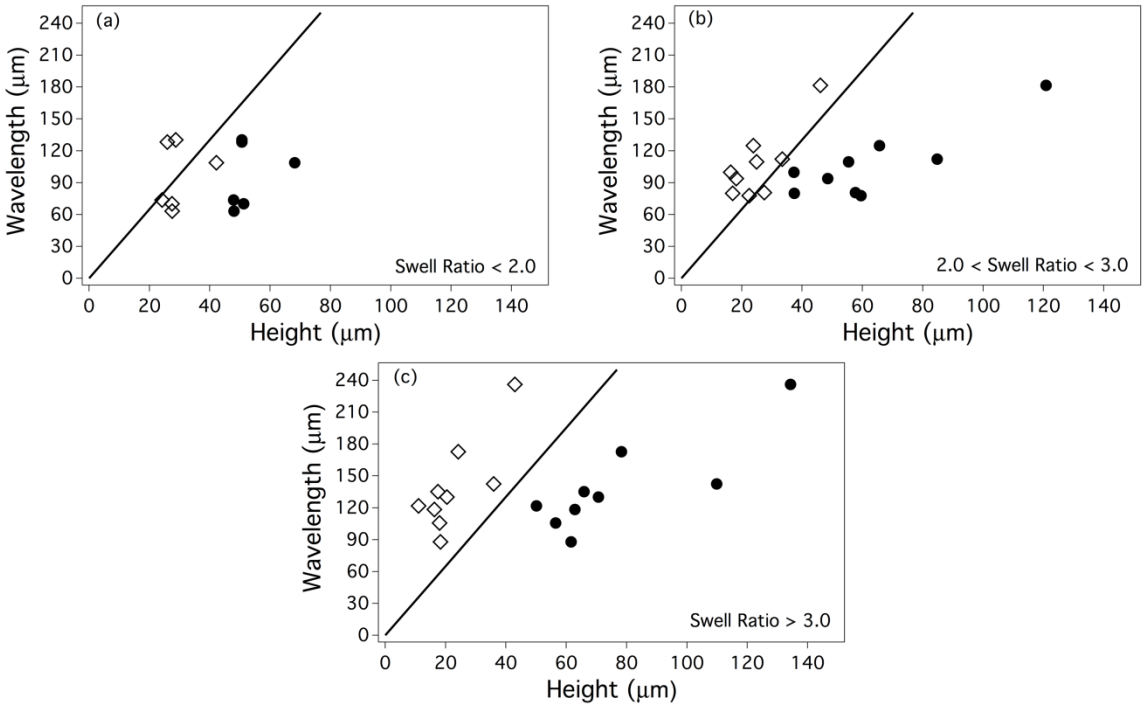

Figure 3-13: Data from global buckling gels with referenced height in the collapsed state (◊) and the swollen state (●) and separated by swelling ratios. (a) swelling ratio < 2.0, (b) swelling ratio between 2.0 and 3.0, and (c) swelling ratio between 3.0 and 4.0. The solid line represents the theoretical relationship ($\lambda = 3.2h$) given by linear elastic theory [49, 66].

From these graphs, it can be seen that only at the lowest swelling ratio does the dry thickness fit the theory. At the medium swelling ratio, however, the wavelength vs. dry thickness shifts to the left of the theoretical prediction. Finally, at the highest degree of swelling, there is an even further shift in the wavelength vs. dry thickness. Therefore, as the swelling ratio increases the dry height less accurately predicts the wavelength of the instability. This finding suggests that gels with a greater degree of swelling are able to swell further in the vertical direction before the onset of the instability, inferring that the geometry of the gel at which the instability wavelength emerges is reached during the swelling process and depends highly on the degree of swelling [49]. Additionally, this may suggest that the aspect ratio of the structure is changing which could be due to non-uniform expansion in height with respect to width.

In order to further understand the discrepancies between experimental observations and the linear elastic theory derived by Mora et al. a relationship between the structural aspect ratio and the resultant wavelength was developed following a few simple assumptions. The model presented in Eq. 3.1 and Eq. 3.2 which describe the characteristic wavelength (Eq. 3.1) and critical deformation at the onset of buckling (Eq. 3.2) are referenced to the dry state geometry and depend on h and $\left(\frac{w}{h}\right)^2$ respectively. Additionally, this model assumes that the elongation ratio (α) is equal in all dimensions. In order to combine these two equations it was assumed that the critical deformation (k_c) that is reached at the onset of buckling is equal to the deformation which establishes the buckling wavelength (α_h) such that α_h and k_c can be related by:

$$k_c = \alpha_h - 1 \qquad \text{(Eq. 3.5)}$$

In order to adjust the model to account for the emergence of an instability due to an intermediate geometry, the dimensional components of height and width were modified such that $h = h_0\alpha_h$ and $w = w_0\alpha_w$. This leads to modification of Eq. 3.1 and 3.2 into the following:

$$\lambda = 3.256 h_0 \alpha_h \quad \text{(Eq. 3.6)}$$

$$\alpha_h - 1 = 0.867 \left(\frac{\alpha_w}{\alpha_h}\right)^2 \left(\frac{w_0}{h_0}\right)^2 \quad \text{(Eq. 3.7)}$$

Equations Eq. 3.6 and Eq. 3.7 can be rearranged to form the following relationship:

$$\frac{\lambda}{h_0} = 2.823 \left(\frac{\alpha_w}{\alpha_h}\right)^2 \left(\frac{w_0}{h_0}\right)^2 + 3.256 \quad \text{(Eq. 3.8)}$$

If the elongation ratio of the structure is assumed the same in all dimensions at the onset of the buckling instability ($\alpha_h = \alpha_w = \alpha$) and Eq. 3.8 simplifies to:

$$\frac{\lambda}{h_0} = 2.823 \left(\frac{w_0}{h_0}\right)^2 + 3.256 \quad \text{(Eq. 3.9)}$$

Data acquired from a series of constant height and constant width pNIPAAm structures with values of α ranging from 1.6 to 3.8 and exhibit a bulk buckling instability were plotted in the form of Eq. 3.9. This was applied to further test agreement between experimental observations and the theoretical prediction resulting from the linear elastic model regarding the dependence of the buckling wavelength and the initial dry structure geometry of the pNIPAAm structure. The results of this analysis are provided in Figure 3-14, where experimental data is plotted and compared to the predictions of the linear elastic model such that the non-dimensional wavelength (λ/h_0) is a function of the dry-state geometry $(w_0/h_0)^2$.

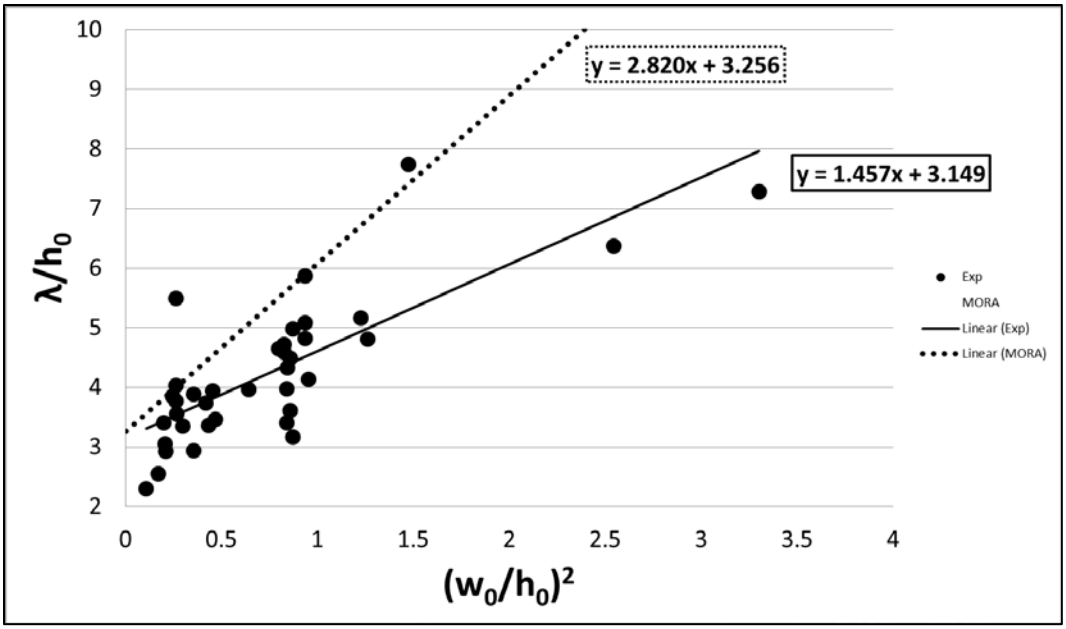

Figure 3-14: Geometric data from constant height and constant width structures taken in the dry state. Data plotted against the non-dimensional wavelength observed upon swelling compared to a linear elastic model developed by Mora et al. (dashed line)[66].

The data presented in Figure 3-14 shows a wide distribution although an increasing trend is noticeable in the region predicted by the linear elastic model. Linear regression was performed resulting in a linear model based on the data of the form: $\frac{\lambda}{h_0} = 1.457\left(\frac{w_0}{h_0}\right)^2 + 3.149$. The goodness of fit for this linear regression model was R^2 = 0.60. Interestingly, the data presents a y-intercept of 3.149 which is in good agreement with the linear elastic model and fundamentally represents the proportionality constant found in the original model equation for predicting the instability wavelength (Eq. 3.1) where this constant is defined in terms the critical wave number (q_c) such that $\frac{2\pi}{q_c} = 3.256$. The slopes, however, are very different. The slope calculated by linear regression of the data (1.457) is approximately 50% of the slope from the linear elastic model. The slope from the linear elastic model represents two distinct quantities, the first being a

function of q_c $\left(\frac{2\pi}{q_c}\right)$ and the second being a function of P_c $\left(\frac{P_c}{12}\right)$ such that: $= \left(\frac{2\pi}{q_c}\right)\left(\frac{P_c}{12}\right) = 2.82$. The discrepancy between this data and the linear elastic model could be explained by the assumption made in deriving Eq. 3.9. It was assumed that α was equal in all dimensions such that $\alpha_h = \alpha_w = \alpha$. If this condition is relaxed, the slope would account for differences between the elongation in height and width at the onset of the instability such that the slope would have the form presented in Eq. 3.8: $\text{slope} = 2.82\left(\frac{\alpha_w}{\alpha_h}\right)^2$. Due to confinement, swelling parallel to the confining surface ($\alpha_{L,}$ α_w) is diminished compared to swelling perpendicular to the confining surface (α_h) resulting in the residual stress which ultimately leads to bending and formation of bulk buckling. Therefore, the discrepancy between experimental observations and the linear elastic model which assumes these deformations to be constant may be reconciled by examining the ratio $\left(\frac{\alpha_w}{\alpha_h}\right)^2$. Adding this term to the slope and solving for the ratio of elongation factors results in a value of $\frac{\alpha_h}{\alpha_w} = 1.39$. This suggests that elongation may be approximately 40% greater in the height dimension than the width dimension at the point which the instability and its characteristic wavelength is established. This data was taken over a range of α-values which may also have added to spread in the data. As the previous analysis suggests that elongation in the height dimension may exceed elongation in the width dimension, the equilibrium value of α (α_{eq}) may play an important role in fixing the structure's geometry at the onset of the buckling instability. In order to evaluate the effect of α_{eq} on the discrepancy between experimental observation and the linear elastic model, data collected from variable width structures, previously used to evaluate the AR at the onset

of buckling, were used to collect wavelength data at variable width and constant height for a series of α_{eq} -values as presented in Figure 3-15.

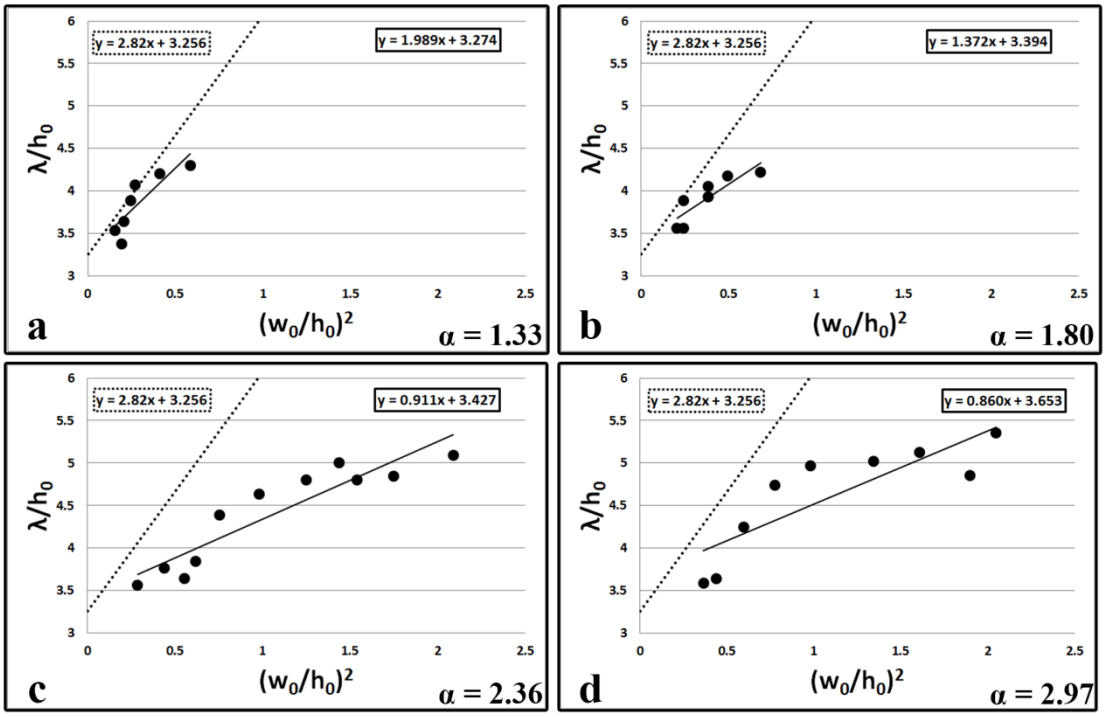

Figure 3-15: Geometric data from constant height and variable width structures taken in the dry state at various values of α_{eq}. α_{eq} = 1.33 (a), α_{eq} = 1.80 (b), α_{eq} = 2.36 (c), and α_{eq} = 2.97 (d) plotted against the non-dimensional wavelength observed upon swelling in a form adapted from a linear elastic model developed by Mora et al. (dashed line) [66].

For each value of α_{eq} there appears to be a distinct linear trend in the non-dimensional wave length ($\frac{\lambda}{h_0}$) as a function of $\left(\frac{w_0}{h_0}\right)^2$. The intercepts of the $\frac{\lambda}{h_0}$ axis, as estimated by linear regression, remain in close proximity to the theoretical value (3.256) with the intercept from the lowest α_{eq} value (3.274) being in the closest agreement. As α_{eq} increases the $\frac{\lambda}{h_0}$ axis intercept increases with a maximum observed value of 3.653 at α_{eq} = 2.97. For the eight α_{eq} values tested which ranged from 1.33 to 2.97 the mean intercept

was 3.324 ± 0.310. Although α_{eq} did not exhibit much influence on the $\frac{\lambda}{h_0}$ intercept, there does appear to be a strong correlation with the slope. The slope of these plots represents the change in the non-dimensional wave length as a function of the inverse aspect ratio squared: $\frac{d\left(\frac{\lambda}{h_0}\right)}{d\left(\frac{w_0}{h_0}\right)^2}$. For each value of α_{eq} tested, the slope was plotted to investigate the potential relationship (Figure 3-16).

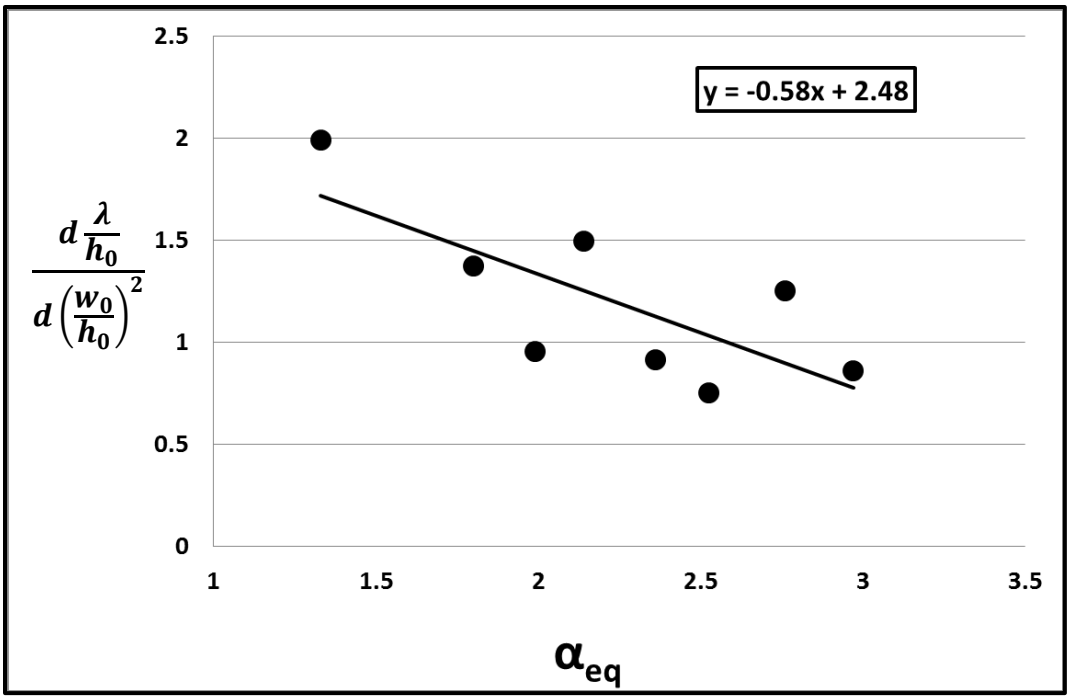

Figure 3-16: A plot of $\frac{d\left(\frac{\lambda}{h_0}\right)}{d\left(\frac{w_0}{h_0}\right)^2}$ as a function of various values of α_{eq} calculated from measurement of constant height and variable width pNIPAAm structures.

From this data it appears that there is a strong correlation between α_{eq} and the slope in Eq. 3.8. This suggests that the equilibrium degree of swelling has a strong influence on the relationship between the dry state geometry of a structure and the characteristic wavelength of the buckling instability. The previous investigation

suggested that this could be due to non-uniform swelling such that swelling in the height dimension (α_h) is greater than in the width dimension (α_w) resulting in a mid-transition geometry which dictates the characteristic geometry of the instability. To test this, the $\frac{\alpha_h}{\alpha_w}$ component of the slope was calculated from the modified linear elastic model and plotted as a function of α_{eq}. The results of this analysis are provided in Figure 3-17.

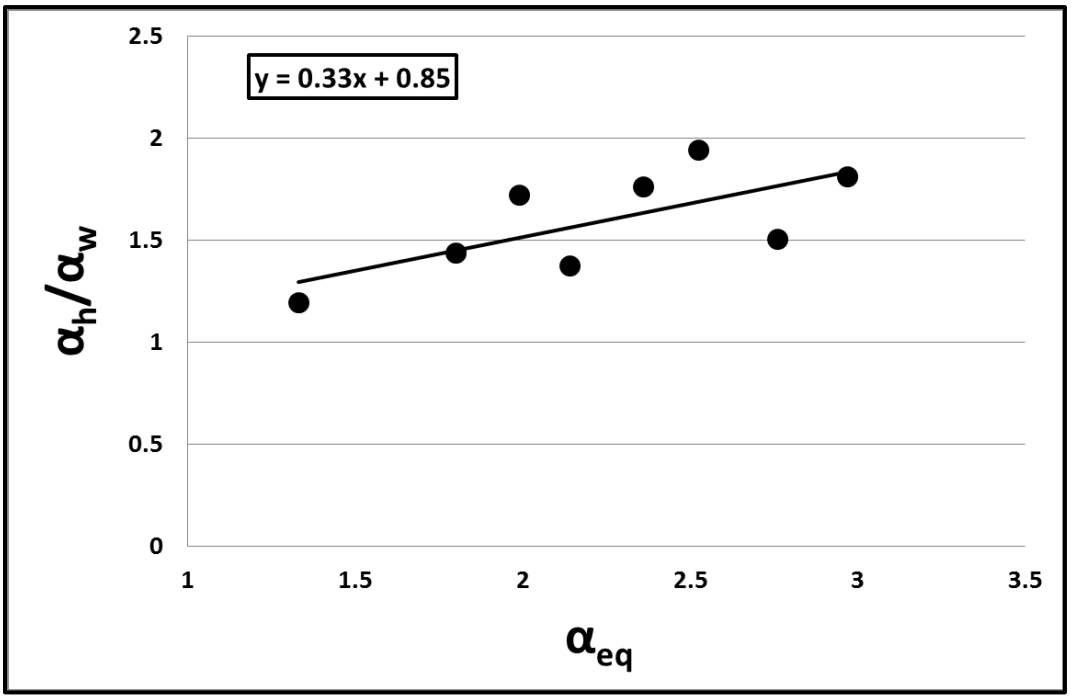

Figure 3-17: Plot showing the measured relationship between the equilibrium swelling ratio (α_{eq}) and the ratio between elongation in the height (α_h) dimension and width (α_w) dimension.

A distinct linear trend is observed between the predicted ratio of elongation factors $\frac{\alpha_h}{\alpha_w}$ at the point the characteristic wavelength is established and the unconfined elongation ratio α_{eq}. The values of $\frac{\alpha_h}{\alpha_w}$ range from 1.2 to 1.9 over the range of α_{eq} values tested suggesting that as the unconfined degree of swelling increases elongation in the

height dimension increases more rapidly than elongation in the width dimension. This finding provides additional evidence that discrepancies between the model suggested by Mora et al. and the results of these studies could be due to the assumption that swelling is uniform prior to the onset of the instability. Additionally, the data presented in Figure 3-17 predicts that at $\alpha_{eq} = 1$ the value of $\frac{\alpha_h}{\alpha_w}$ closely approaches unity, having a predicted value of 1.18, as would be expected.

Over the course of evaluating the swelling-induced buckling of pNIPAAm structures an interesting phenomenon was observed in structures fabricated to have a high degree of swelling with $\alpha > 2$. During the swelling process, structures having constant width revealed the formation of discrete intermediate instabilities which emerged throughout the swelling transition, ultimately resulting in the formation of a buckled structure upon reaching equilibrium swelling. In Figure 3-18 a constant width (20μm), and constant height (22μm) structure with an elongation ratio of $\alpha = 2.97$ is seen forming an edge buckling instability which begins with a mean characteristic wavelength of 19.8μm (Figure 3-18b) which, upon further swelling, snaps into a longer edge buckling wavelength of 32.2μm (Figure 3-18c), finally forming a bulk buckling structure at equilibrium swelling with a mean characteristic wavelength of 89.5μm (Figure 3-18d). This observation reinforces two previously discussed observations regarding the formation of these instabilities. First, the formation of localized edge buckling in structures possessing a high degree of swelling occurs prior to the onset of bulk buckling during the swelling process. Second, significant swelling can occur before the onset of bulk buckling such that the dry geometry is not a suitable reference to predict the characteristics of the swollen geometry. This also suggests that the geometry of the

localized edge buckling instability is sensitive to structure geometry and in the case of the structure in Figure 3-18 the structure reached multiple critical states which led to the rapid snapping of the swelling structure geometry into three stable modes with distinct characteristics until being locked into the last stable state due to a rapid decrease in structure deformation, ultimately reaching equilibrium swelling.

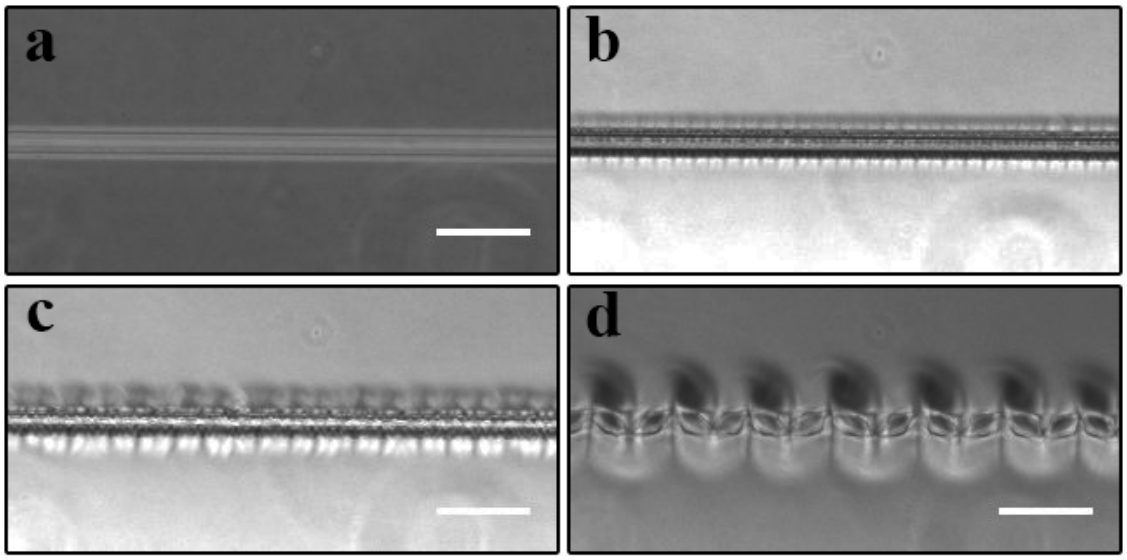

Figure 3-18: Phase contrast images of a pNIPAAm structure having dimensions of 20μm width and 22μm height in the dry state (a) showing the swelling-induced formation of discrete intermediate structures (b,c) until swelling equilibrium is reached (d). Size bars represent 100μm.

In addition to the observation of the formation of localized edge buckling prior to the formation of a final bulk buckled structure, confined structures which snapped between multiple bulk buckling wavelengths was also observed during transient swelling. A structure of constant height (22μm) and width (30μm), and having an elongation ratio of $\alpha = 2.4$, was observed over the course of swelling as shown in Figure 3-19. Like the structure shown in Figure 3-19, this structure exhibited localized edge buckling at the

onset of swelling with a characteristic wavelength of 15.2µm (Figure 3-19b). But, unlike the previous structure, the structure in Figure 3-19 began to exhibit bulk buckling in the early stages of swelling (Figure 3-19c) with a mean characteristic wavelength of 21.4µm and subsequently snapped into a second mean wavelength of 38.5µm (Figure 3-19d) before finally adopting its equilibrium mean wavelength of 70.1µm (Figure 3-19e). The transition from each subsequent wavelength was not gradual but rather very rapid as the structure snapped into each wavelength it remained for a period as the amplitude grew and subsequently snapped into the next wavelength until finally reaching equilibrium swelling. Interestingly, upon drying and subsequent swelling of samples which exhibited multiple intermediate wavelengths in their first swelling, the phenomenon was not observed again in the subsequent exposures to solvent.

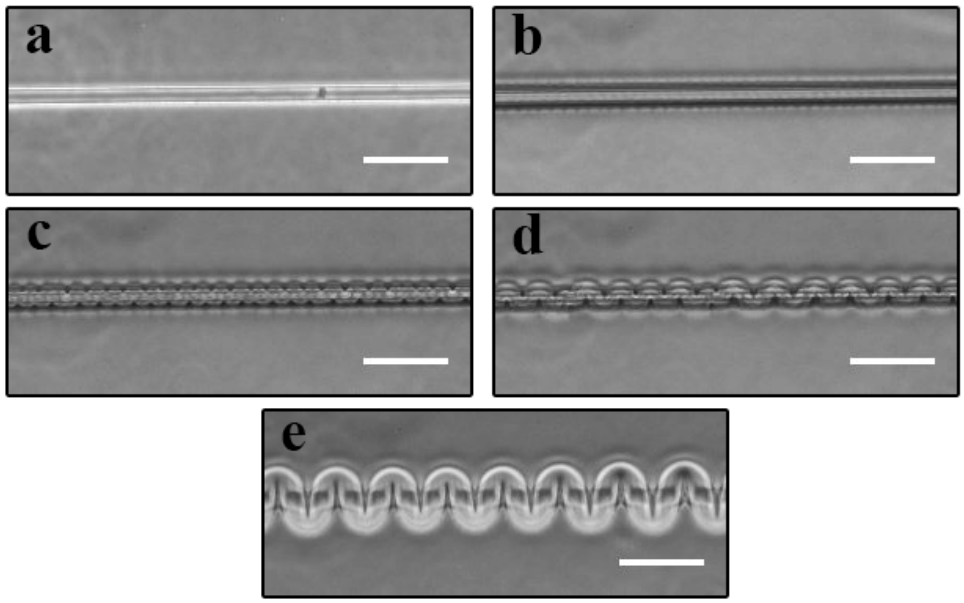

Figure 3-19: Phase contrast images of a pNIPAAm structure having dimensions of 30µm width and 22µm height in the dry state (a) and exhibiting swelling induced localized edge buckling (b) followed by the formation of a bulk buckled structure which snapped into three characteristic wavelengths (c-d) before reaching swelling equilibrium. Size bar represents 100µm.

Another pNIPAAm structure having the same elongation ratio and height as the structure presented in Figure 3-19 but fabricated with a larger width (40μm) demonstrated a third type of transient structure which arose during the swelling process. This structure exhibits an instability (Figure 3-20b) which is extremely similar to localized edge buckling but is distinctly different in that the edge cusps fold into the bulk structure as previous observations only show the edge buckling occurring on the periphery of the structure where the bulk of the structure maintains its rectangular shape.

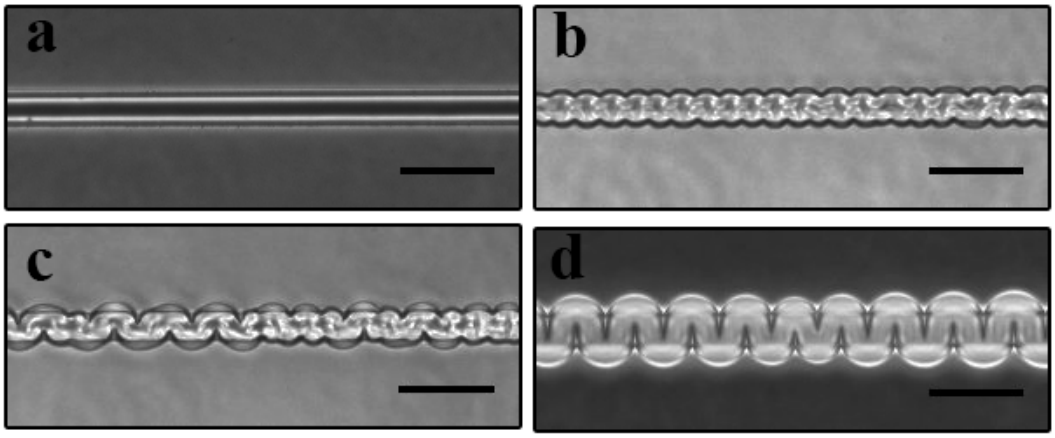

Figure 3-20: Phase contrast images of a pNIPAAm structure having dimensions of 40μm width and 22μm height showing mid transition modes. Images provided in the dry state (a) exhibiting a periodic pattern on the edge during the swelling process (b,c) and ultimately leading to the formation of a bulk buckled structure (d). Size bars represent 100μm.

To illuminate whether a buckled pNIPAAm structure can fully be described by linear theory, a localized fluorescence quenching test (Figure 3-21) of a structure having an equilibrium elongation ratio of $\alpha = 2$ was performed by quenching fluorescence in the dry structure and generating lines absent of fluorescence both perpendicular and parallel to the structure axis. This test reveals that lines parallel to the beam axis (Figure 3-21c)

remain parallel after deformation. Lines perpendicular to the beam axis (Figure 3-21a) remain straight after deformation, however only at the apex of a bend. Near the inflection point, slight curvature is observed as demonstrated by the mismatch in the arrow directions at point B. The arrows are drawn parallel to the quench line at both sides of the beam such that if the line remained straight the arrow lines would overlap. While this observation is qualitative in nature, the curvature of the quench line suggests that linear theory may not completely capture the final geometric characteristics of a buckled beam.

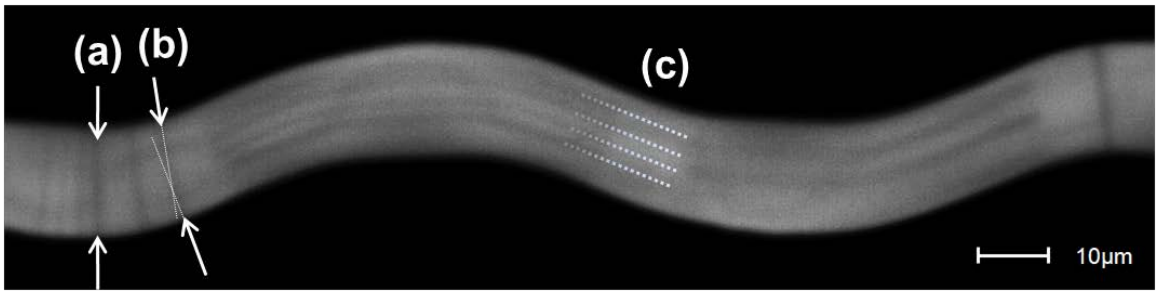

Figure 3-21: Localized fluorescence quenching test for a bulk buckling structure performed in the dry state and imaged after swelling. Arrows (a) and (b) refer to quenched lines perpendicular to the beam axis and are drawn parallel to the quenched lines on both sides of the beam. Point (c) refers to quenched lines parallel to the beam axis [49].

Further investigation into the three-dimensional geometry of buckled pNIPAAm structures reveals other phenomena which, to date; have not been previously reported in experimental observations. Figure 3-22 presents a three-dimensional reconstruction derived from images taken by confocal microscopy of a 10μm width structure having a height of 13μm and an elongation ratio of $\alpha = 2.5$. Upon visual observation, it can be seen that the tallest point of the structure exists at the apex of the buckle. At the tallest points, the width (x-dimension) is much smaller than most of the structure and this does not occur over the structures mid-axis, but over the edge of the structure closest to the center-

line of confinement. In general, the structure appears to be non-uniformly bending as the amplitude grows leading to a structure buckled structure where the original upper surface plane is no longer parallel to the confinement plane leading to surface cusps. In fact, it only appears that the region where the original upper surface plane is still parallel to the confinement plane is at the inflection point between buckles.

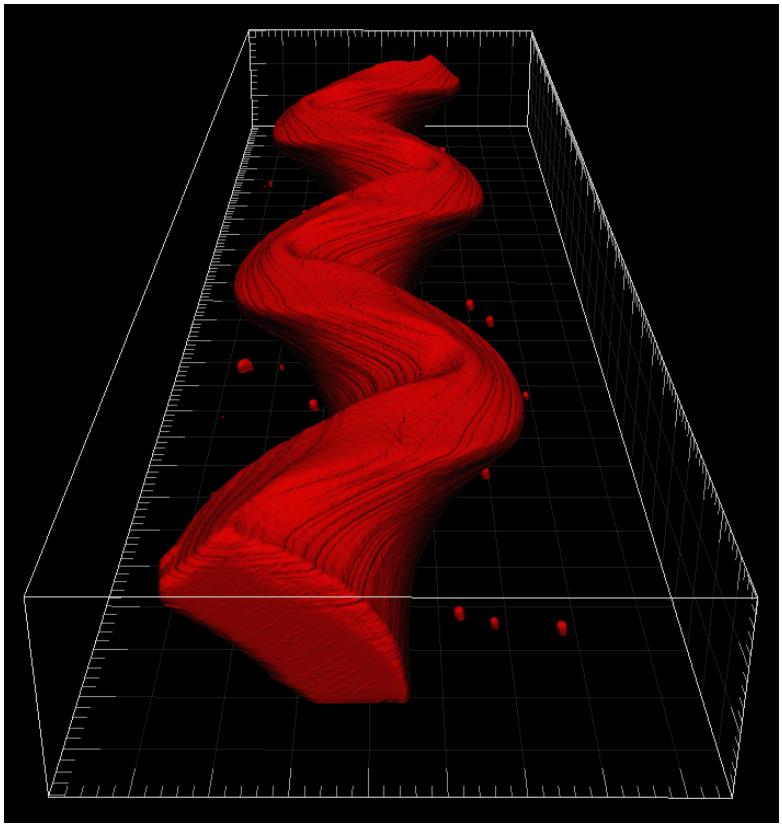

Figure 3-22: A three-dimensional reconstruction of the surface geometry using images taken by confocal microscopy of a surface confined pNIPAAm structure exhibiting a bulk buckling instability.

To measure these observations measurements were made to gather data regarding the buckled structure's three-dimensional geometry. Using image slices from various points along the z-axis (height) of the structure taken by confocal microscopy the

following measurements were made in subsequent x-y planes as a function of height: mid-structure path length, buckle amplitude, structure width at buckle apex (at the center of amplitude), and structure width at inflection point. Details regarding the location of these measurements are provided in Figure 3-23.

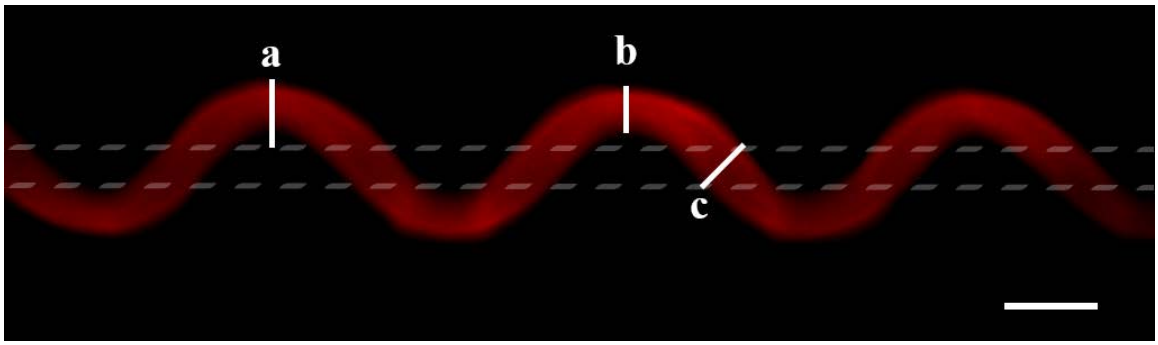

Figure 3-23: An x-y plane image slice taken by confocal microscopy showing the location of the following measurements: buckling amplitude (a), width at buckle apex (b) and width at inflection point. Dashed lines represent region of confinement at the base of the structure. Size bar represents 20µm.

Data collected from this experiment is presented in Figure 3-24. From these results we can see direct quantitative validation of the previously described observations regarding the three-dimensional structure of the buckled pNIPAAm structure. From Figure 3-24a, a linear increase in structure path length is seen as a function of internal height until a maximum is reached at approximately 30µm or about 70% of its total swollen height after which it remains relatively constant. Overall, the path length increases by approximately 30% throughout the height of the buckled structure. This analysis also reveals that the x-y plane width of the structure is very different when measured at the apex of the buckling amplitude (Figure 3-24b) and the inflection points between buckles (Figure 3-24c). For measurements made at the apex of buckling

amplitude, a gradual increase in x-y plane width is measured and at approximately 30µm within the structure height a drastic drop in width is measured. This quantitatively describes the aforementioned surface cusps, or low width regions in the x-y plane at peripheral z-positions due to bending of the structure. In contrast, the width of the swollen structure changes very little at the inflection point between buckles. A slight increase is measured within the first 5µm of height and remains relatively constant throughout the remaining portion of the structure height for a 36% increase in structure width at the inflection. Finally, measurement of the buckling amplitude shows a trend similar to widths measured in that domain (Figure 3-24d). Buckling amplitude increases linearly with height (z-position) until reaching approximately 70% of the x-y plane height of the structure at which it decreases linearly.

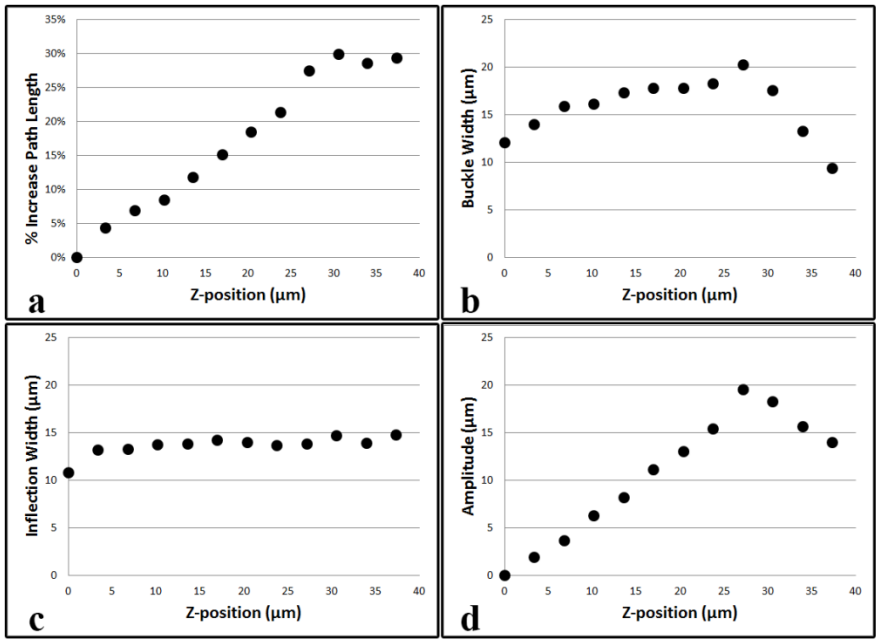

Figure 3-24: Plots of various key measurements as a function of z-position. Data includes measurements of path length increase (a), structure width at the apex of buckling amplitude (b), structure width at the inflection between amplitudes (c) and amplitude (d) made at various x-y planes along the z-axis in a buckled pNIPAAm structure.

In order to further evaluate the three-dimensional geometry of buckling pNIPAAm structures a simple method was applied to incrementally control the degree of swelling in order to perform measurements as the final equilibrium structure evolves. Previous studies have shown that addition of certain types of salt, such as sodium chloride, to the aqueous environment can greatly influence the phase transition in pNIPAAm gels [109, 130-133]. At room temperature (~28°C) pNIPAAm exists in a highly swollen state but in the presence of high salt concentrations swelling is negligible. As the salt concentration is reduced swelling gradually increases making this a good method for modulating pNIPAAm structure swelling. This effect was exploited by swelling polymer structures with similar dry state dimensions as that presented in Figure 3-22 in order to control the swelling behavior of the structure and perform measurements as the final buckled structure evolves. Sodium chloride was used at concentrations ranging from 5.0M to 0M resulting in a structure in its fully collapsed state and fully swollen state respectively. The data collected from these experiments is presented in Figure 3-25. Data collected for salt concentrations above 2.5M were excluded as the geometry was nearly identical to the dry geometry and provided no further insights. Changes in the % increase in path length continue to show a linear relationship throughout most of the structure height finally reaching a maximum and remaining constant although the slope decreases with increasing salt concentration (Figure 3-25a). The width at the buckling apex also follows a similar trend as presented previously although reaching a reduced maximum width at higher salt concentrations (Figure 3-25b). Additionally, the reduction in width at increasing z-position throughout the structure was much more gradual at higher salt concentrations and began at approximately 50% of the total structure height in contrast to

25% observed in the absence of salt. The inflection width of the pNIPAAm structure in pure water shows a slight increase within the first 5-10μm and remains constant throughout the remainder of its height. At a high salt concentration (2.5M) very little expansion of the width is measured staying nearly constant at its fabrication geometry throughout the structure's height. Oddly, for salt concentrations of 1.8M and 0.6M the inflection width appears to be slightly thinning near the top of the structure, something that is not observed in either the fully collapsed or swollen structure. The buckling amplitude follows the same trend for 0.0M, 0.6M, and 1.8M where buckling amplitude increases, reaches a peak and drops off. The buckling amplitude only slightly increases at 2.5M showing that a distinct wavelength was adopted although the magnitude of swelling was low. Another important piece of information can be derived from the results of this test. Although the structure width remained relatively constant at the fabrication/dry state width throughout the structure height at 2.5M ($\alpha_h \approx 1$), the structure height increased by approximately 35%. This provides additional data which suggests that the aspect ratio at which the length-scale of the instability is adopted may be greater than what is measured in the dry state as structure height extends more rapidly than width throughout the swelling process. This is to be expected as the confinement plane should impact elongation parallel to the surface, while elongation perpendicular to the surface should be impacted to a lesser degree. As these dimensions are changing non-uniformly, the point at which an instability manifests would not be easily predicted by the dry-state dimensions of the structure alone and would most likely be established at a mid-swelling geometry.

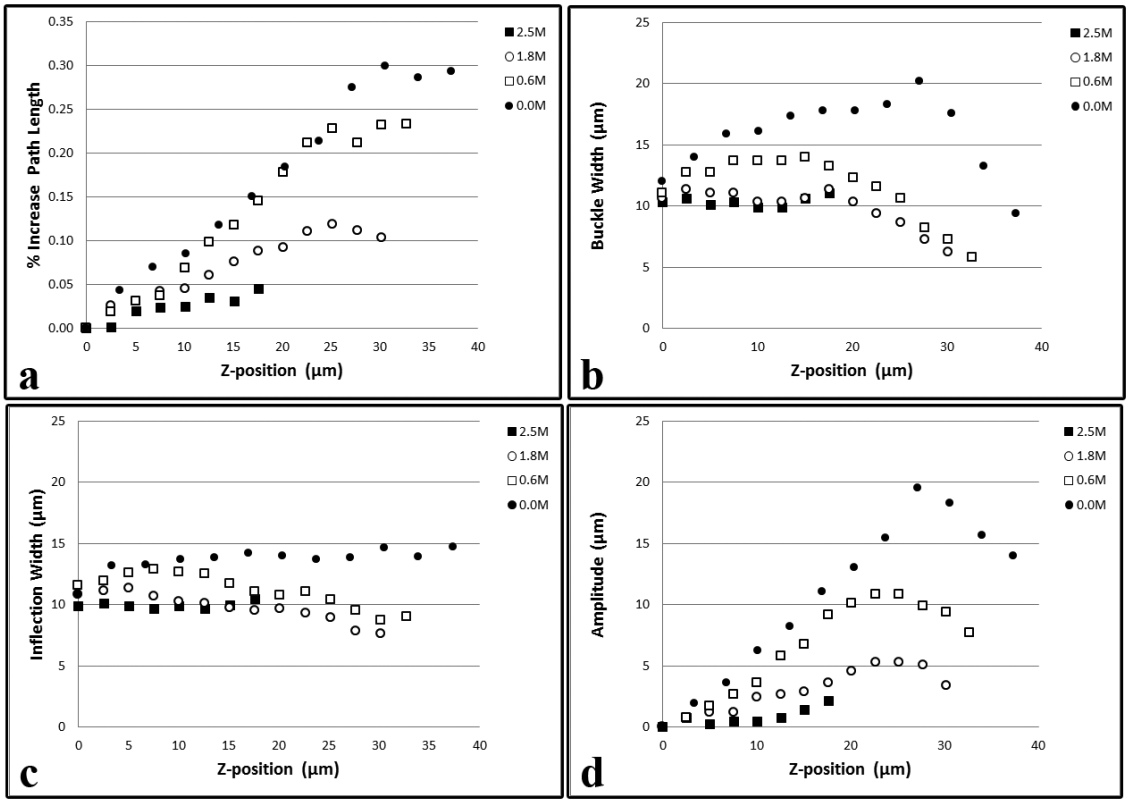

Figure 3-25: Plots showing various measurements made at different points in the structure height (z- axis) at various sodium chloride concentrations. Measurements include: increase in path length (a), buckle width (b), inflection width (c), and amplitude (d) at sodium chloride concentrations of 0.0M (●), 0.6M (□), 1.8M (○), and 2.5M (■).

In order to test whether the establishment of a swollen buckled geometry from a virgin sample (never in the presence of a solvent post fabrication) has an effect on subsequent swelling in a solvent of differing quality, samples were swollen in one solvent twice and then subjected to a second solvent and measurements of wavelength and amplitude were performed. Samples were completely dried between swellings and n-butanol was chosen as a secondary solvent to water. Although n-butanol has a stronger influence on the swelling ratio in a pNIPAAm gel, the structures used in this study were co-polymerized with acrylic acid (20%) such that swelling in water greatly exceeds swelling in n-butanol [(110)]. The results of this test, presented in Figure 3-26, show that

solvent history, and thus degree of swelling, has little impact on the established wavelength of the buckling instability regardless of the order of swelling. Measurement of buckling amplitude shows the greatest value when expanded in water regardless of solvent history. In contrast, the amplitude in structures initially expanded in n-butanol was slightly greater than after expansion in water. This provides some evidence that solvent history may have an impact on the geometry adopted by pNIPAAm structures at swelling equilibrium.

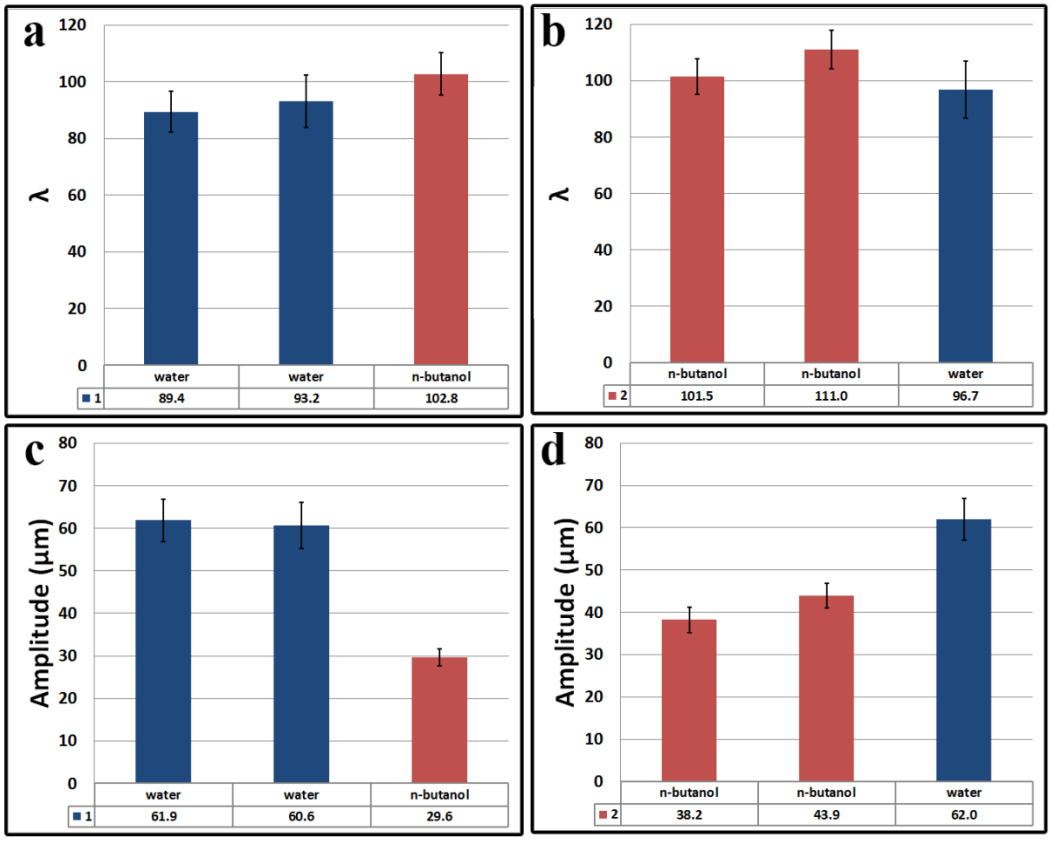

Figure 3-26: Effects of subsequent swelling in solvents of differing quality and its effect on the buckled state geometry. Structures swollen initially in water (a,c) compared to structures initially swollen in n-butanol (b,d) taking measurements of bulk buckling wavelength (a,b) and amplitude (c,d). Error bars represent one standard deviation.

During the course of these experiments, an unexpected anomaly was witnessed for structures which were exposed to n-butanol after having been previously exposed to water (Figure 3-27). Typically, swelling of a micron-scale pNIPAAm structure in water reaches near-equilibrium swelling, such that the swollen geometry is unchanging, within approximately one minute of exposure to solvent. Swelling of a virgin, or newly fabricated, sample in n-butanol possessed the same behavior suggesting that the native diffusion rate is similar to that in water. In contrast, swelling of these structures in n-butanol, after exposure to water revealed an interesting phenomenon. Structures that were first exposed to water, dried, and then exposed to n-butanol exhibited the formation of an irregular "cracking" pattern in both rectangular structures and wide micron-scale films. These "cracking" patterns persisted throughout swelling but eventually dissipated upon equilibrium formation of the buckling structure. Most interestingly, the time required to reach an equilibrium structure was significantly increased to approximately 15 minutes in 20μm wide structures having a height of 21μm and in thick pNIPAAm films. In contrast, this phenomenon was not observed in structures initially exposed to n-butanol, dried, and subsequently swelled in water. This could be due to residual trapped water in the dry state structure. If this is the case, exposure to a new solvent, such as n-butanol, may cause a temporary gradient of mixed water and butanol to develop and may remain within and surrounding the gel until all trapped water is released into the bulk. Previous reports have demonstrated how mixtures of water and alcohols can significantly impact the swelling of pNIPAAm gels [(134)]. It could be some form of this effect which causes what was observed in Figure 3-27.

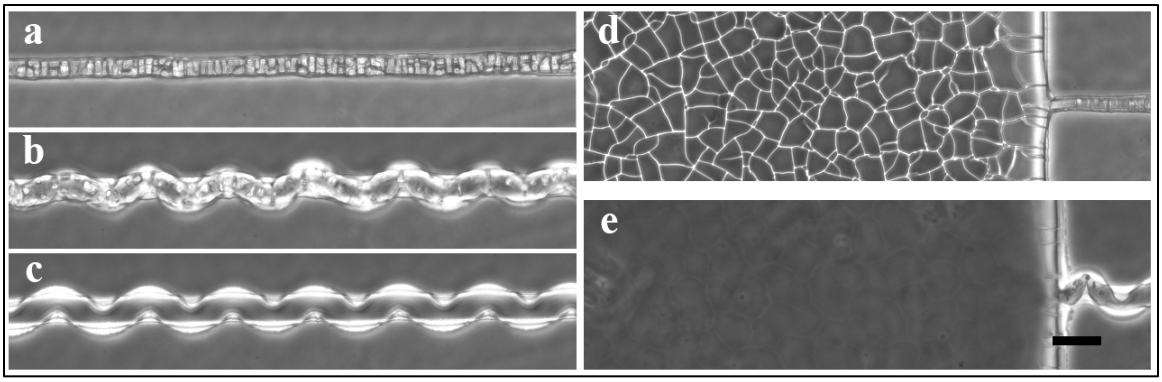

Figure 3-27: Swelling of a pNIPAAm structure in n-butanol after swelling and drying in water. Swelling of the structure after exposure to n-butanol for 3 minutes (a,d), 10 minutes (b), and 15 minutes (c,e). Size bar represents 50μm.

One final observation made in samples which had experienced multiple swelling/drying cycles was the presence of an oscillating pattern observed in the dry state. These patterns, which were observed by examination of fluorescent images taken of the structures, appear within the bulk of the dry gel and are similar to a buckled pattern but possess a different periodicity. This was only observed in some samples after drying and a complete investigation of this phenomenon was not performed. The periodicity of the oscillating pattern is about 1/3 of the swollen, buckled, wavelength. While it is unclear why these patterns emerge and there was no clear rationale for their emergence, this may be due to effects on the internal gel structure as a result of the non-uniform stresses which manifest due to confinement of a swollen structure. Although most samples observed after drying did not appear to exhibit this behavior, it was observed frequently enough to make note of it here and may be more ubiquitous than what was observed as this phenomena was not a focus of this work, but may warrant more exclusive attention.

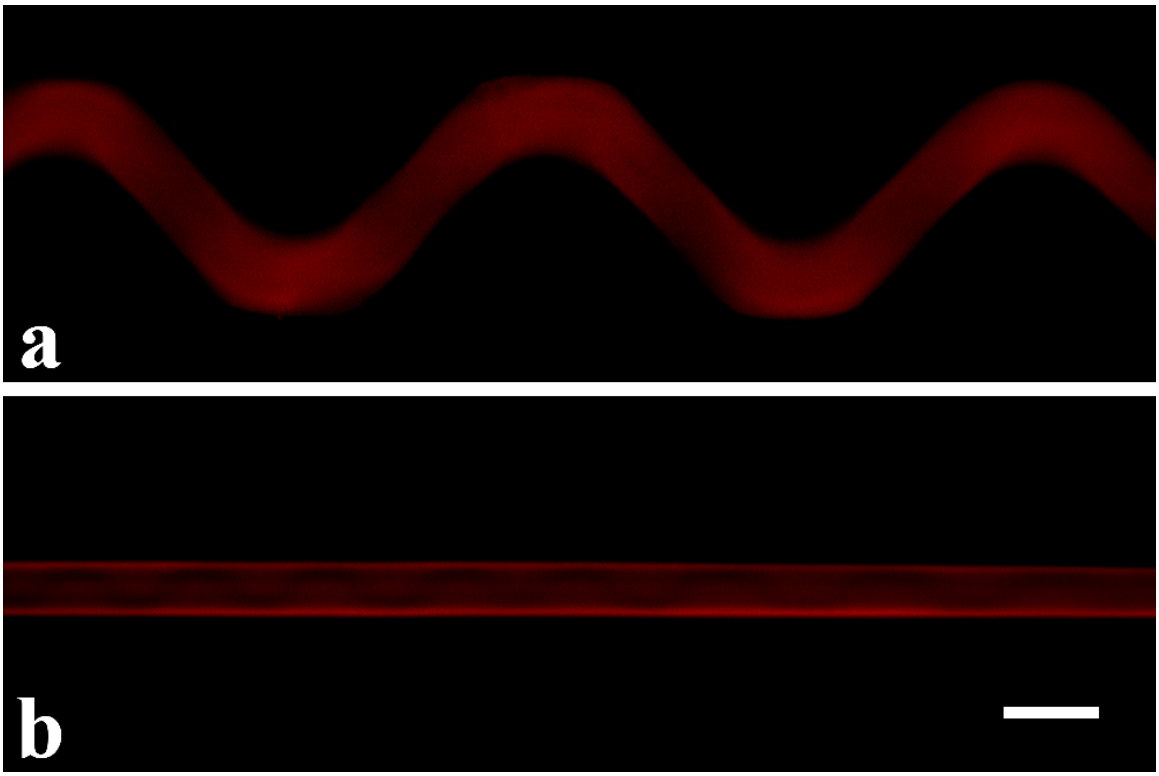

Figure 3-28: Presence of an internal pattern in a pNIPAAm structure after multiple swelling/deswelling events. A 10μm wide structure in the swollen state (a) compared to the structure after removal of solvent (b) showing an internal pattern with a periodicity of approximately 1/3 the buckled wavelength. Size bar represents 20μm.

3.2.4 Differential Lateral Swelling and Edge Buckling

As discussed previously in section 3.2.2, a swelling pNIPAAm structure which does not meet the critical criteria required to induce a bulk buckling instability still experiences non-uniform swelling. Perhaps the most simple manifestation of this is occurs as the gel swells outwards along its width in a non-uniform fashion as shown in Figure 3-27. This will be referred to as differential lateral swelling as elongation of the structure's width is near zero at the plane of confinement and increases with increasing distance from the confinement plane. This form of instability has been observed in previous studies and has even been exploited for particle capture and release [49, 70, 71].

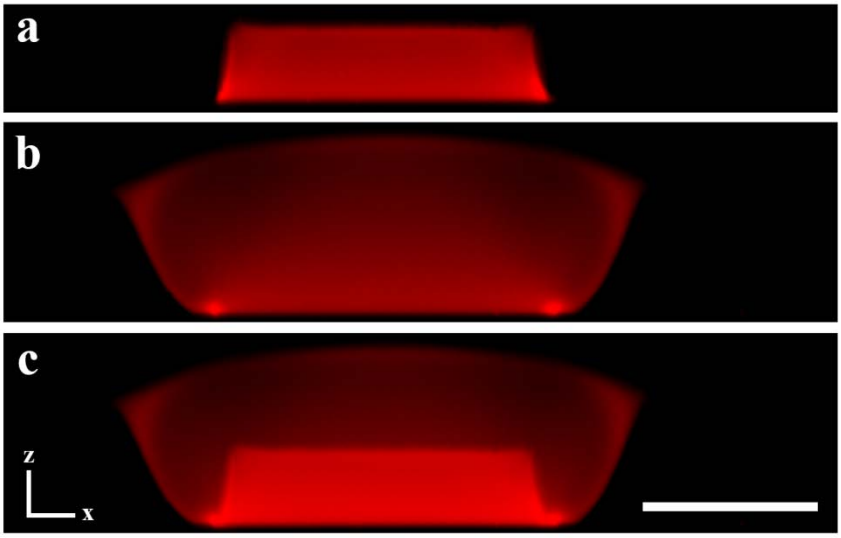

Figure 3-29: Cross-sectional image of a pNIPAAm structure showing differential lateral swelling. Images were taken by confocal microscopy and show the x,z-plane of a 100µm wide and 20µm height pNIPAAm structure cross-section in the dry (a) and swollen (b) states including an overlay of the two states (c). Size bar represents 50µm.

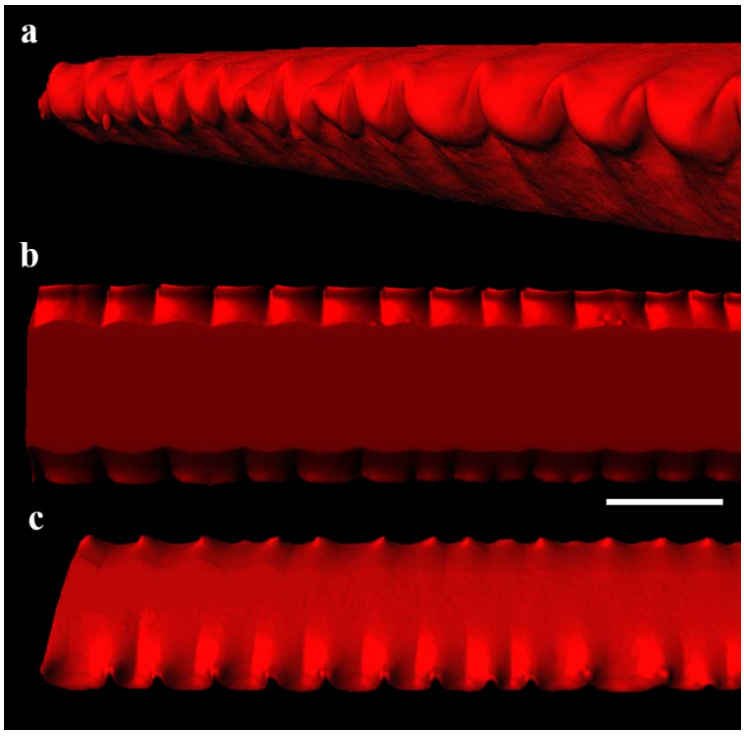

Figure 3-30: Surfaces rendered from confocal microscopy image slices showing localized edge buckling in low aspect ratio structures. Arbitrary side view (a), bottom view showing the confinement plane (b), and arbitrary top view. Size bar represents 100µm (b).

For structures with dry dimensions below the critical geometric requirements for bulk buckling, and at sufficiently low degrees of swelling (α below approximately 1.9), this is the primary form of non-uniform swelling observed. At higher degrees of swelling, a second non-uniformity emerges in the form of localized edge buckling (Figure 3-30).

From a typical microscope view (top down), localized edge buckling structures appear as a rectangular structure near the central axis with protruding cusps on the periphery with a defined periodicity, or wavelength, and amplitude (Figure 3-31). These features are similar to those observed in the Mora et al. study at geometries which did not result in bulk buckling structures [66].

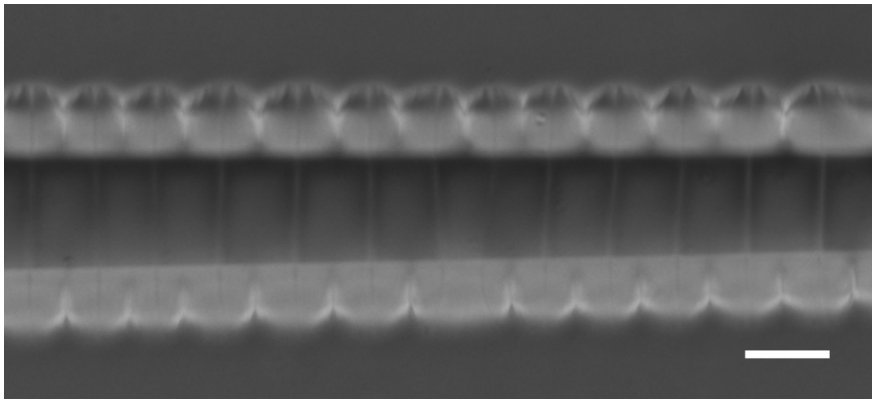

Figure 3-31: Localized edge buckling in a variable width pNIPAAm structure with a degree of swelling of α = 1.99. Size bar represents 50μm.

A closer view of the localized edge buckling instability is provided in Figure 3-31. This form of non-uniform swelling manifests at the upper edge of the structure's width and appears as a buckled, or undulating, pattern which propagates down the structure's length. Unlike bulk buckling, this pattern is not wave-like, as its undulating protrusions are asymmetric about the y-axis, or the length axis, of the structure. Most interestingly, in Figure 3-31, surface wrinkling is observed marked by the lines which

periodically propagate across the structures width. These lines appear to align with the center of the cusps, or undulations, which manifest on the structure's periphery. Although pure conjecture, it is possible that stresses which cause the periodic lines, or wrinkling of the surface, play a role in the formation of the localized edge buckling instability. This could be potentially similar to the increased localized tension caused by compression of a drawn window curtain's top resulting in a rippled effect at its base.

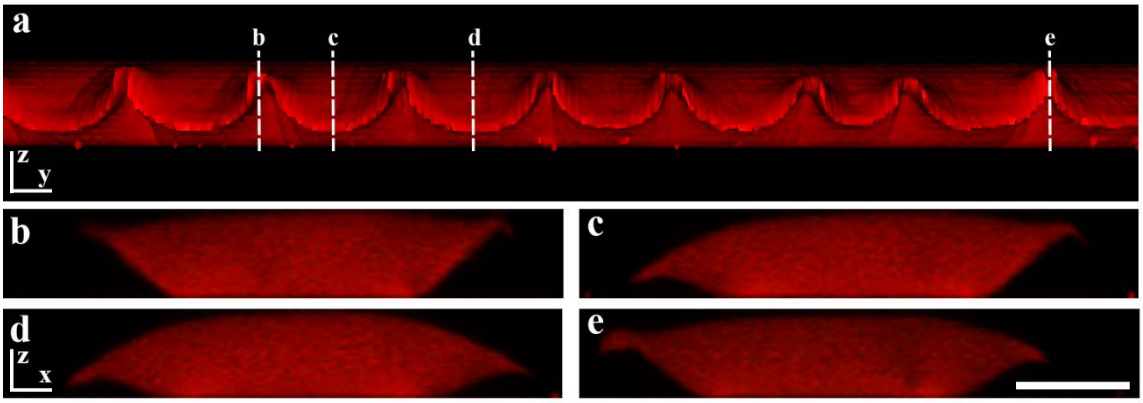

Figure 3-32: Localized edge buckling from a side view with cross-sections. A rendered surface from confocal image slices showing a side view of localized edge buckling (a) with cross-sections along various portions of the structure (b-e). Size bar represents 50μm.

Analysis of edge buckling structures was performed on variable width pNIPAAm structures in order to gain further insight into the nature of this form of instability. As previous data has shown that the measureable onset of this instability is a function of the degree of swelling, measurements of the edge buckling periodicity, or wavelength, (λ) and the lateral extension, or amplitude, where collected on a number of variable width structures at various degrees of swelling ranging from $\alpha = 1.99$ to $\alpha = 2.97$ (Figure 3-32).

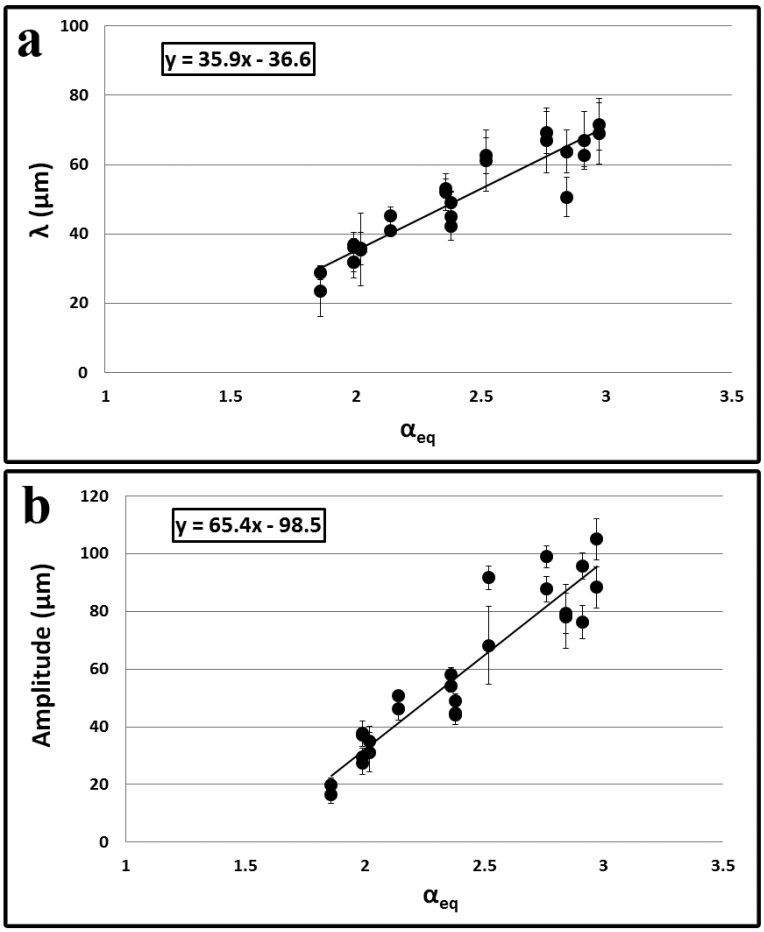

Figure 3-33: Plots of the wavelength (a) and amplitude (b) of edge buckling structures at various degrees of swelling.

No meaningful correlation could be made between changes in width with respect to λ or edge buckling amplitude. The degree of swelling (α_{eq}), however, showed a strong linear correlation with both of these measurements. Evaluation of the linear relationship between λ and α_{eq} reveals that this data shows a linear decrease in λ at decreasing α_{eq} and predicts at $\alpha_{eq} = 1$, where the structure is undeformed and swelling is zero, that λ goes to a value of nearly zero as would be expected (Figure 3-33a). Additionally, the edge buckling amplitude decreases linearly with decreasing α_{eq} (Figure 3-33b). This relationship predicts that the amplitude diminishes to zero at $\alpha_{eq} \sim 1.5$ which could

explain the perceived absence of the edge buckling instability in structures with $\alpha_{eq} < 1.9$ as the observable amplitude of this instability limited the capacity to measure its characteristic geometry.

3.3 Discussion of Results

Confinement of a swellable structure leads to anisotropic swelling of the structure over the course of solvent penetration due to a non-uniform distribution of compressive stresses generated by an anisotropic expansion of the structure. As swellable materials are becoming increasingly applied in engineering designs of many types, it is important to have a simple method for predicting the impact of non-uniform swelling on the behavior and equilibrium geometry of a confined structure. Recently, many attempts have been made to model the effects of confinement on the equilibrium geometry achieved upon completion of the swelling process [66, 69, 71, 126]. Of these, a simple model developed by Mora et al. was shown to agree well with buckling instabilities observed in an acrylamide gel bound to a rigid surface [66]. This model generated two simple relationships regarding the shape and onset of the buckling instability (Eq. 3.1 and Eq. 3.2). The onset of the bulk buckling instability was predicted to be dictated by a critical compressive stress which is a function of the dry state aspect ratio. The applicability of this model to confined pNIPAAm structures was tested in section 3.2.2. Tests were performed by using a series of variable width structures at constant height. Samples of differing degrees of swelling were tested and the width at the onset of the bulk buckling instability was recorded to obtain the aspect ratio at which the instability manifested for a given degree of swelling. It was found that the aspect ratio at which the onset of buckling occurred did follow a

linear trend with respect to the degree of swelling as Mora et al. predicted; however, the proportionality was not in agreement. In section 3.2.3 it was suggested that discrepancies between experimental measurements and the model may arise due to anisotropic expansion during the swelling process such that the onset of the instability occurs mid-swelling. This would result in a critical aspect ratio which is proportional, but not equal, to the dry state geometry. The proportionality between the dry state geometry and the critical state geometry can be described by introducing an anisotropic swelling factor such that: $\frac{w_c}{h_c} = \left(\frac{\alpha_w}{\alpha_h}\right)\left(\frac{w_0}{h_0}\right)$, where w_c and h_c denote the geometry at the onset of the instability and w_0 and h_0 denote the dry geometry. Within this framework, the experimentally observed onset of the bulk buckling instability occurs at $\left(\frac{\alpha_h}{\alpha_w}\right) = 1.23$ suggesting that elongation of the structures height (α_h) is 23% greater than its width (α_w) at the onset of the instability. This result is consistent with the expected influence of structural confinement as elongation in the structure's width is strongly influenced by the confining boundary condition while elongation in structure's height is free from constraint. Another possible explanation for this discrepancy is similar to the previous postulation but includes a material property component, the modulus of elasticity. Previous studies have shown that the elastic, or Young's, modulus of a pNIPAAm gel changes dramatically between its swollen and unswollen states [135, 136]. In an anisotropically swelling structure it would be expected that the elastic modulus would also become anisotropic resulting in directionally dependent deformations in response to an applied stress. The model used for comparison does not take these differences into account, in fact, the condition which predicts the onset of the bulk buckling instability is predicted by a constant non-dimensional compressive stress. Swelling-induced strain

throughout the gel structure dictates the resultant stress which, in a linear framework, is directly proportional to the elastic modulus. If deformations are anisotropic then it would be expected that the elastic modulus would be directionally dependent and the non-dimensional compressive stress, which dictates the onset of the bulk buckling instability, would occur at both a geometry which differs from the initial state and be strongly influenced by an anisotropic modulus. Further evidence points to the onset of bulk buckling at a mid-transition geometry in a structure where height was measured in both the dry and swollen state. The results show that the theoretical aspect ratio prediction lied between experimental measurements of structure height made in the dry and swollen states, again suggesting that the critical geometry is established mid-transition. In one study a non-linear finite element method was developed to predict the formation of crease-like instabilities at a low aspect ratio and bulk buckling at high aspect ratios. The model predicted that the degree of swelling, represented in the model by the crosslink density, played a large role in predicting the formation of both forms of instability but could not resolve the value of the wavelength [71]. Interestingly, this model does agree with the general trend observed in data obtained from variable width structures where the formation of surface wrinkling and localized edge buckling were observed at low aspect ratios and higher degrees of swelling suggesting that the creases predicted by this model may arise from conditions similar to the formation of localized edge buckling.

Similar discrepancies arose when evaluating the geometry established in bulk buckling structures. The linear framework suggests that the characteristic wavelength is purely a function of the structure's height such that $\lambda = 3.2h$. Data from experiments performed on pNIPAAm structures showed that at low degrees of swelling such that $\alpha <$

2, the dry state height was in close agreement with the theoretical prediction. In contrast, as the degree of swelling increased, measurement of the dry height under predicted the theory while measurement of the swollen height over predicted the theory. This again provides evidence for establishment of a mid-transitional geometry which fixes the characteristic wavelength. It is important to note that the experimental data used by Mora et al. to test the model was within the range of $1.15 < \alpha < 1.85$. Agreement of their data and the data in this study at low α fall in line with the general assumptions in the linear elastic framework such that a linear model is typically valid for systems where deformations are small. Furthermore, the buckling wavelength was measured on variable aspect ratio structures and compared to the dry state geometry. It was found that $\left(\frac{\alpha_h}{\alpha_w}\right)$ increased with increasing equilibrium degree of swelling such that: $\frac{\alpha_h}{\alpha_w} \approx \frac{1}{3}\alpha_{eq} + 0.85$. As one should expect, at a zero degree of swelling (α_{eq} = 1) differences between elongation in height (α_h) and width (α_w) vanish and $\frac{\alpha_h}{\alpha_w} \approx 1$. Although this is an empirical approximation derived under the assumption that $\alpha_h \approx \alpha_{eq}$, it could still prove as a simple method by which to understand the characteristic geometry adopted by a buckled structure for materials subject to large deformations. A study performed by Sultan et al. tested a stiff swelling gel clamped to a soft non-swelling surface and found that the mismatch in Young's modulus for the two materials impacted the observed equilibrium wavelength in comparison to that predicted by the linear Mora model [67]. It was found that the wavelength scaled as $\left(\frac{E_{stiff}}{E_{soft}}\right)^{\frac{1}{3}}$h, where E_{stiff} and E_{soft} are the respective Young's moduli and h is the height of the structure. Although a quantitative comparison cannot be made, it is expected that during the swelling of a pNIPAAm structure the elasticity of the

material changes as the material expands [135, 136]. Since expansion of the base portion of the structure is highly confined compared to the top, it is expected that a similar discrepancy in elasticity would exist throughout the structure. In contrast, it would be expected that the mismatch in elastic properties would not occur at a specific point but be continuous both during the swelling process and at swelling equilibrium making the findings in this study difficult to directly compare although the general trend is consistent.

Another interesting result from these studies was the observation of multiple mid-swelling structures as shown in Figures 3-18 through 3-20. These observations show that the characteristic wavelength of the transient structures increase from state to state and finally adopt a permanent wavelength at equilibrium swelling of the bulk buckled structure. Interestingly, the formation of these intermediate structures was not smooth but the structures "snapped" from one state to the next at various points in the swelling process. These observations suggest that as the swelling process proceeds the structure may reach various transient geometries which meet the critical criteria for instability formation. During the formulation of the model presented by Mora et al., the most unstable wave number was used to predict the dimensions of the final buckled structure (Figure 3-33) [66]. The formation of transient wavelengths observed in this study may suggest that as the structure swells multiple critical points are met such that the relationship between P_c and q_c is changing. This may arise from the formulation which led to the prediction of these critical values. The non-dimensional compressive stress, P, has the form: $P = 12(\alpha_{eq} - 1)\left(\frac{h}{w}\right)^2$. As P is a function of both swelling and geometry, and previous results suggest that swelling is not equal in h and w, snapping between

multiple intermediate states could be explained by changes in the function P(q) driven by transient changes in the effective aspect ratio such that $\left(\frac{\alpha_h}{\alpha_w}\right) = f(\alpha)$ as suggested by data in Figure 3-17.

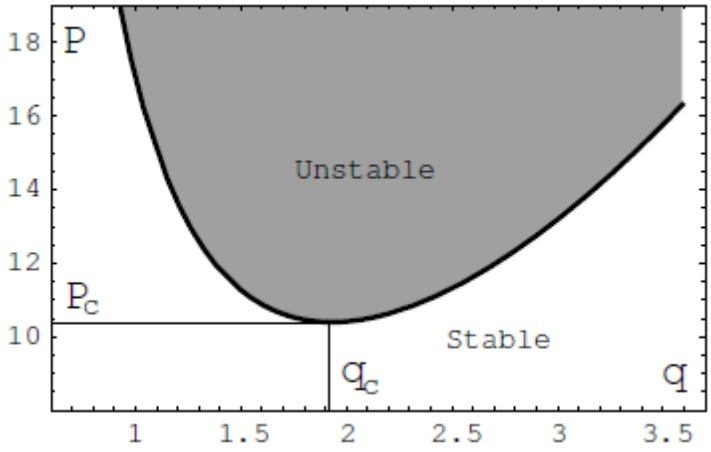

Figure 3-34: Stability diagram presented by Mora et al. This diagram shows the general relationship between the non-dimensional compressive stress (P) as a function of the non-dimensional wave number (q) [66].

Localized edge buckling was observed in non-bulk buckling structures at increased degrees of swelling (α above approximately 1.9). This phenomenon is similar to that observed in corona type geometries [65, 66, 126]. It was also shown that structures similar to those seen in locally buckling structures appear in the initial phases of swelling which leads to bulk buckling of a structure (Figure 3-19). The instability can be described by buckling perpendicular to the confining surface on the top edge of a structure. The periodicity of the instability and the in-plane amplitude scale linearly with the equilibrium degree of swelling. Analysis of this data suggests that at equilibrium swelling below α = 1.5, the amplitude is non-existent providing further evidence that this form of instability only manifests at large degrees of deformation. Although the importance of

this is not yet understood, it provides some basic guidelines to predicting the formation and geometry of these structures.

3.4 Summary

Swelling of confined structures, fabricated by simple two-dimensional techniques, can lead to a variety of rich three-dimensional geometries which emerge as a result anisotropic swelling and non-uniform stresses. Gaining additional data to understand the formation of these geometries is critical to further understanding the important parameters required to develop simple and applicable models for engineering design. Formation of four basic types of non-uniform swelling were seen to manifest in rectangular, surface confined, pNIPAAm structures: bulk buckling, differential lateral swelling, localized edge buckling, and surface wrinkling.

It was shown that at small degrees of swelling ($\alpha < 2$) the data was in general agreement with a simple linear elastic model in predicting the onset and geometry of bulk buckling. As swelling increased, the linear model became increasingly divergent from experimental observations, most likely due to non-uniformities in structure elasticity and deformation during the swelling process. This analysis suggests that the geometry which dictates the final equilibrium structure is attained during the swelling process at an aspect ratio which is dissimilar from the dry state. A simple modification to the linear model which accounts for uneven swelling in height with respect to width was applied. This led to the formulation of a simple linear relationship between the equilibrium degree of swelling and the ratio of elongation in height and width. This modified linear elastic model can serve as a useful tool for predicting the geometric effects of swelling on

confined structures which is extremely important in applying swellable materials in engineering design. Additionally, various stable structures were observed throughout the swelling process before the final instability geometry was reached further giving evidence of the importance of the transient geometry of a swelling structure under large deformations.

Chapter 4: pNIPAAm Structures for Culture of Organized Micro-Tissues

4.1 Traditional Cell Culture

Culture of eukaryotic cell types has been practiced for over half a century with an increased emphasis on animal and, more specifically, mammalian cell lines as these cell types provide the greatest insights into human health. Cell culture ultimately aims to serve as a primary or secondary platform for understanding the fundamental relationships between cells of different types and their chemical and physical environment in addition to interactions between cells. Cells can be cultured in two basic environments; as cell suspensions or adherent cultures. This research focuses on the growth of adherent cells; therefore adherent cell culture will be the primary focus of subsequent discussions. Typical growth, proliferation, and maintenance of adherent cells is performed on flat, two-dimensional, surfaces primed for cell culture. Polystyrene is a common substrate used for the culture of adherent cells although modification of the surface chemistry is usually essential to promote suitable cell attachment, spreading, and proliferation [(137)]. Typically, cells grown on two-dimensional surfaces, such as polystyrene, are used to maintain cell cultures, observe the stages of cell attachment and proliferation, or test cellular response to chemical treatments [(138)]. In the context of tissue engineering, where development of complex well-organized tissues is paramount, two-dimensional culture methods are generally utilized for cell proliferation.

The primary aim of tissue engineering is to form cellular constructs which mimic or reproduce the complicated functions of native tissues. In light of this goal, two major complications arise when applying traditional cell culturing techniques: lack of cell organization and translocation of cultured tissues. Adherent cells grown on standard tissue culture polystyrene (TCPS) surfaces adhere to the surface, flatten, spread along the surface, and begin to undergo mitosis leading to cellular proliferation on the surface. In this case, the orientation and organization of the cells is completely absent and cells within the culture are positioned and oriented randomly as shown in Figure 4-1a.

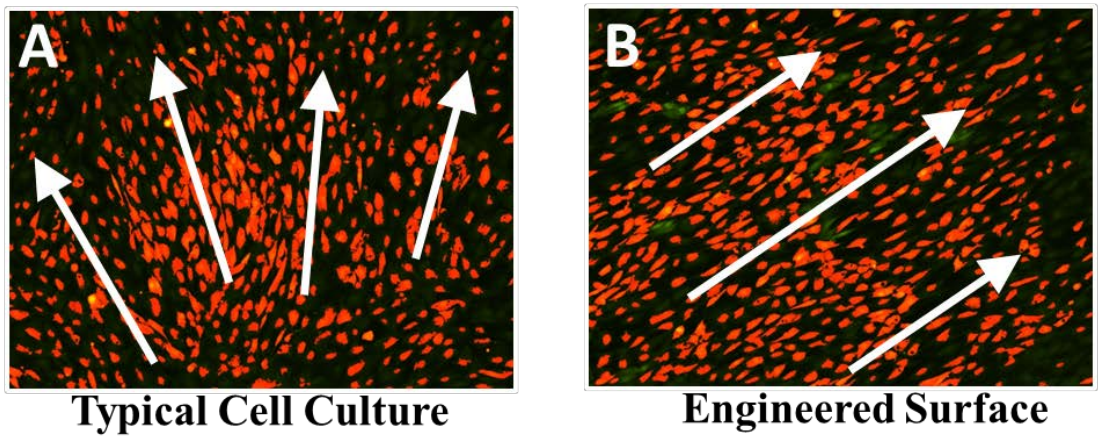

Figure 4-1: NIH 3T3 Fibroblasts dyed with calcein-AM (thresholding/masking performed to highlight cell bodies) on a standard TCPS dish (a) with no long range order compared to cells on an engineered pNIPAAm surface (b) designed to induce cell alignment.

To address this failure in controlling cell behavior numerous engineering approaches have been developed to induce control over cell orientation (Figure 4-1b) and develop organized micro-tissues. These methods will be described in more detail in subsequent sections of this chapter.

In addition to directing cell organization, translocation of organized micro-tissues is typically desired for further testing, delivery *in vivo*, or for subsequent construction of increasingly complex tissues. In standard culture, removal of adherent cells is typically accomplished through enzymatic digestion of ECM proteins to which the cells are attached. This is typically initiated by the serine protease trypsin and often accompanied by the chelating agent ethylenediaminetetraacetic acid (EDTA) to scavenge calcium and magnesium ions. This method of cell removal is not preferred for cells which have been organized into ordered micro-tissues because the digestion of ECM proteins may result in release of cells bound to the surface but also disrupts cell/cell contacts and destroys the matrix which holds the micro-tissue together effectively disaggregating the entire tissue and resulting in well dispersed individual cells which have a rounded appearance [(139)].

4.2 Engineering Approaches to Cell Organization

Development of complex tissues *in vitro* which possess all aspects of native tissues is paramount for the general aims of tissue engineering. An important challenge to the development of these tissues is that of cell organization. Many of the tissues in our body are designed of multiple cell types combined together with a very specific organized structure which is essential to the proper function of the tissue [(140)]. A few examples of tissue types that require a high degree of organization include vascular tissue [(141)], intervertebral discs [(142)], skeletal muscle [(143)], and myocardial tissue [(144, 145)] to name a few. In order to develop tissues which properly mimic the function of native tissues, the organization of cultured cells must be achieved in a simple and controllable way. The most common method of inducing spatial organization and alignment of cultured cells is

to exploit the natural phenomena of contact guidance [146-149]. Contact guidance is a general term used to describe the propensity for a cell to orient itself during spreading and/or migration in response to an anisotropic surface. It has been shown that the anisotropy of the surface can be topological [148, 150], mechanical [151, 152], or chemical [153-155] in nature. Cellular response to surface anisotropy is not restricted to cell organization, but has also been shown to have a significant impact on cellular function [146, 151]. Most of the techniques used to culture cells for tissue engineering purposes either directly or indirectly harness the power of contact guidance in order to develop tissues with directed organization. The following sections outline current approaches to inducing cell organization in culture, and introduces a new approach to cell organization on micron-scale pNIPAAm surfaces.

4.2.1 Scaffolds

Scaffolds are possibly the most widely used type of surface for tissue engineering applications today. Modern scaffolding material design and their application was pioneered in the late ‘80s by Vacanti and Langer, and have since led to a wide variety of scaffolding materials, designs, and applications [156]. Typically scaffolds are comprised of synthetic polymer materials such as polylactic acid (PLLA), polyglycolic acid (PGA), and polycaprolactone (PCL) to name a few [157-159]. Scaffold style materials are attractive for tissue engineering-based cell culture as they allow for attachment, migration, differentiation, and growth of cells in a three-dimensional environment. This becomes important as it has been shown that some aspects of cell function and behavior can only be imitated in three-dimensional environments. For instance, it was shown that adhesion

of human foreskin fibroblasts was significantly different on tissues derived from three-dimensional matrices in comparison to culture on two-dimensional surfaces [160]. Design and application of scaffold-based tissue engineering has been successfully applied to a multitude of tissue types such as bone [161, 162], nerve [163, 164], cartilage [161, 162, 165], and vascular tissue [166, 167]. Although scaffold-based tissue engineering shows great clinical promise it is not without its challenges. The primary challenges facing this method of cellular organization include biocompatibility, biodegradability, vascular integration [87], diffusive limitations [88, 168], and mechanical limitations [169].

4.2.2 Decellularized Matrices from Native Tissues

Expanding upon the concept of non-native scaffold materials, research into the application of decellularized tissue matrices as a platform for cell growth has become increasingly studied [170-172]. The ultimate goal of this technique is to remove cell bodies from a native tissue while having minimal impact on the chemical, physical, and biological properties of the remaining ECM. The structure which remains has the overall geometric and chemical properties which could allow for recellularization with cell types derived from a patient's own tissues and thereby increasing the success of transplantation by minimizing potentially troublesome immunological responses. In general, tissues are removed from a host after which they are subjected to a number of processing steps both chemical and physical in nature such as sonication, freezing-thawing, enzymatic treatment, detergent rinsing, and treatment with ionic solutions [173]. Each step in the process acts to remove all cellular components from the protein matrix while leaving the connective ECM structure intact. Recellularization of decellularized matrices has met

with some success in many complex tissue types such as lung tissues [174, 175], liver tissues [172, 176], urological tissues [177], and vascular tissues [170, 178]. Use of decellularized matrices is in its infancy as a technique and still faces many technical challenges such as minimization of decellularization effects on ECM structure and composition, availability of appropriate tissues for decellularization, and cell seeding strategies to accommodate growth of complex tissue structures [173, 179].

4.2.3 Patterned Two-Dimensional Surfaces

Patterning of two-dimensional surfaces to form anisotropic geometric and chemical topographies has been widely applied to cell culture for directing cell spreading, organization, and migration[180]. This method of controlling cell behavior has been applied to numerous material surfaces such as poly-L-lactide/trimethylene carbonate [181], polycarbonate (PC) [182], polycaprolactone (PCL) [182], collagen [183], poly-(D,L-lactide-co-glycolide) (PLGA) [183], quartz [184], poly(methyl methacrylate) (PMMA) [185, 186], photosensitive polyimide [187], PDMS [186, 188], and pNIPAAm [155, 189, 190]. Additionally, this method of inducing cellular organization has been shown to be applicable to an extremely large library of cell types including C2C12 myoblasts [181], MC3T3-E1 osteoblast-like [191], mouse fibroblasts (NIH 3T3) [182], chick heart fibroblasts [184], human endothelial (HGTFN) [182], vascular smooth muscle cells (VSMCs) [183, 186], mouse epithelial (HC11) [192], cardiac myocytes [193], and neurological tissue (PC12) [187]. In each case anisotropic patterns, usually formed of an array of nano-scale to micro-scale rectangular shapes, are used to direct cell orientation causing cells to elongate and spread in the direction of the anisotropy. The surface anisotropy has been demonstrated by both

chemical patterning of the surface [155, 185, 190, 191] or through formation of three-dimensional topographies [182, 185, 191]. Chemical patterning of surfaces is usually accomplished by generating cell-adhesive and non-cell-adhesive domains through selective protein adsorption or modulation of surface hydrophobicity by micro-contact printing or lithography. Studies have been performed to determine the effects of three-dimensional geometry on the alignment of cells with particular focus placed on the periodicity or width of the anisotropy and the depth between extrusions. In general it has been shown that cell alignment favors increased depth of extruded structures and alignment is slowly reduced as structure width is increased [148, 194-196]. One study demonstrated the lower limits on topographical alignment of rat dermal fibroblasts suggesting that alignment was lost for extrusions with depths below 35nm and widths of less than 100nm [197]. Although a wide variety of geometries have been studied and some fundamental relationships between geometry and cell alignment have been observed, it appears that no studies to date have been performed on structures with large depths (>10μm).

In addition to induction of cell organization, these surfaces have been shown to impact cellular function and gene expression. One study demonstrated that anisotropic topographies significantly affected collagen deposition and matrix-metalloproteinase levels in human fibroblasts [195]. It was also noted that the anisotropy of the surface was not the only factor which adjusted the cellular function but the geometry, more specifically the depth, also played a key role. Additionally, it was shown that surface topographies can have an impact on gene expression as it was noted to have an effect on fibronectin mRNA levels in human gingival fibroblasts [198]. Also, anisotropic surfaces

have also been shown to allow for formation of more complex tissues through cellular differentiation. For instance, differentiation of aligned myoblasts into multinucleated fibers or myotubes has been demonstrated by multiple groups [181, 188, 196].

In one study an anisotropic PDMS surface was used to organize skeletal myoblasts (C2C12) into a well aligned micro-tissue which could be differentiated into multinucleated myotubes. Upon subsequent cell seeding, additional layers of myotubes could be formed resulting in a complex three-dimensional micro-tissue. Although alignment of the first layer of myotubes was favorable, alignment of subsequent layers was increasingly diminished making this a limited approach to highly organized three-dimensional micro-tissues [196].

4.3 Organization of Cells on Micron-Scale pNIPAAm Structures

Although organization of cells has been accomplished on many material surfaces, it has yet to be applied to micron-scale three-dimensional topographies comprised of pNIPAAm. Also, as mentioned before, it appears that little to no research has been performed on the culture of cells on anisotropic three-dimensional surfaces extruded from two-dimensional foundations which exhibit length scales above 10μm in depth (extrusion height above surface). Additionally, a major drawback of applying existing strategies for development of complex and relevant tissues for tissue engineering is the lack of a simple mechanism for micro-tissue translocation. In order to apply engineered micro-tissues for use as transplantable tissues for regenerative medicine or subsequent construction of increasingly complex tissues a method of cell harvesting must be built into the culture platform such that translocation of micro-tissues is practical while enduring minimal

augmentation to micro-tissue structure and cellular activity. For these reasons a new platform for cellular organization, which embodies previously validated methodologies, has been applied to micron-scale pNIPAAm patterned surfaces of various depths, spacing, and width. Thermally induced expansion of the pNIPAAm hydrogel structure leads to a significant increase in the surface area of micron-scale pNIPAAM patterns which can facilitate mechanically mediated removal of organized micro-tissues [(49)]. The finer points of micro-tissue release from pNIPAAM surfaces will be discussed in later chapters, for now the discussion will focus on the formation of organized micro-tissues mediated by topological cues engineered into the design of three-dimensional pNIPAAm patterned surfaces. In order to test the capacity for micron-scale pNIPAAm patterned structures to induce cellular organization and alignment two primary types of surfaces were examined. The first test surface is comprised of an array of closely spaced rectangular, beam-like, surface extrusions. The pNIPAAm arrays had dimensions of approximately 4μm in width and 1μm in depth, with spacing of 9μm or 8μm in width and 1μm in depth, with spacing of 12μm (Figure 4-2a). The second group consisted of isolated structures with greater depth, width, and spacing. Structures were spaced by 1000μm with a depth of 21.4μm ±3.0μm and widths ranging from 20μm to 100μm (Figure 4-2b). Each surface was cultured with NIH 3T3 mouse fibroblasts to examine the potential of these surfaces to induce organization and alignment.

4.3.1 Cellular Organization on Arrays of pNIPAAm Structures

Fibroblast alignment on arrayed surfaces of pNIPAAm was significantly improved over control surfaces. Qualitatively, cells cultured on the arrayed surfaces

formed nearly confluent aligned cell sheets where cell alignment followed the long axes of the underlying arrayed structures. Figure 4-3 shows calcein-AM stained fibroblasts cultured on pNIPAAm surfaces after 24 hours of culture while Figure 4-4 shows a composite image of the cells captured in phase contrast. Seeding densities used were high (~500 cells/mm^2) in order to assure rapid population of the surface without need for lengthy proliferation steps. From visual observation of the samples it is quite clear that both 4µm wide structures and 8µm wide structures were capable of aligning the cells.

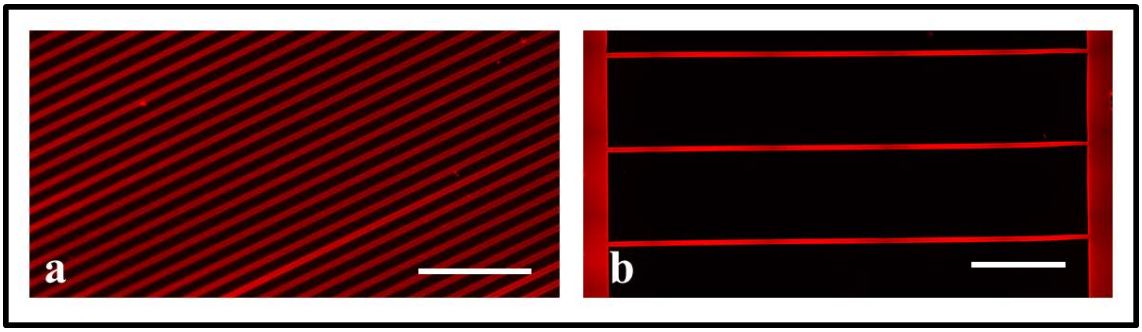

Figure 4-2: Arrayed (a) and isolated (b) three-dimensional pNIPAAm surfaces for cellular organization and alignment shown using fluorescence microscopy to excite embedded rhodamine-b co-monomer. Scale bars represent 100µm (a) and 1000µm (b).

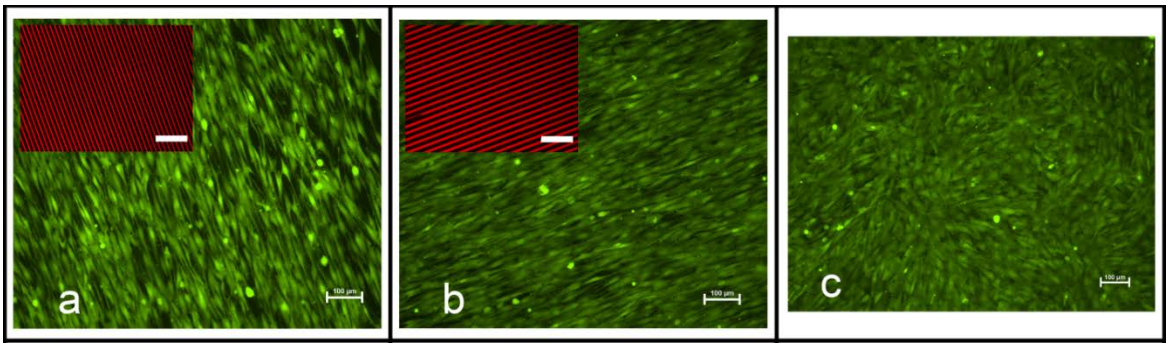

Figure 4-3: Alignment of NIH3T3 mouse fibroblasts stained with calcein-AM cultured on arrays of pNIPAAm structures with widths of 4µm (a) and 8µm (b) in comparison to cells grown on a glass surface (c). Insets (a,b) show alignment of the underlying pNIPAAm structures. Images taken 10X and size bars represent 100µm.

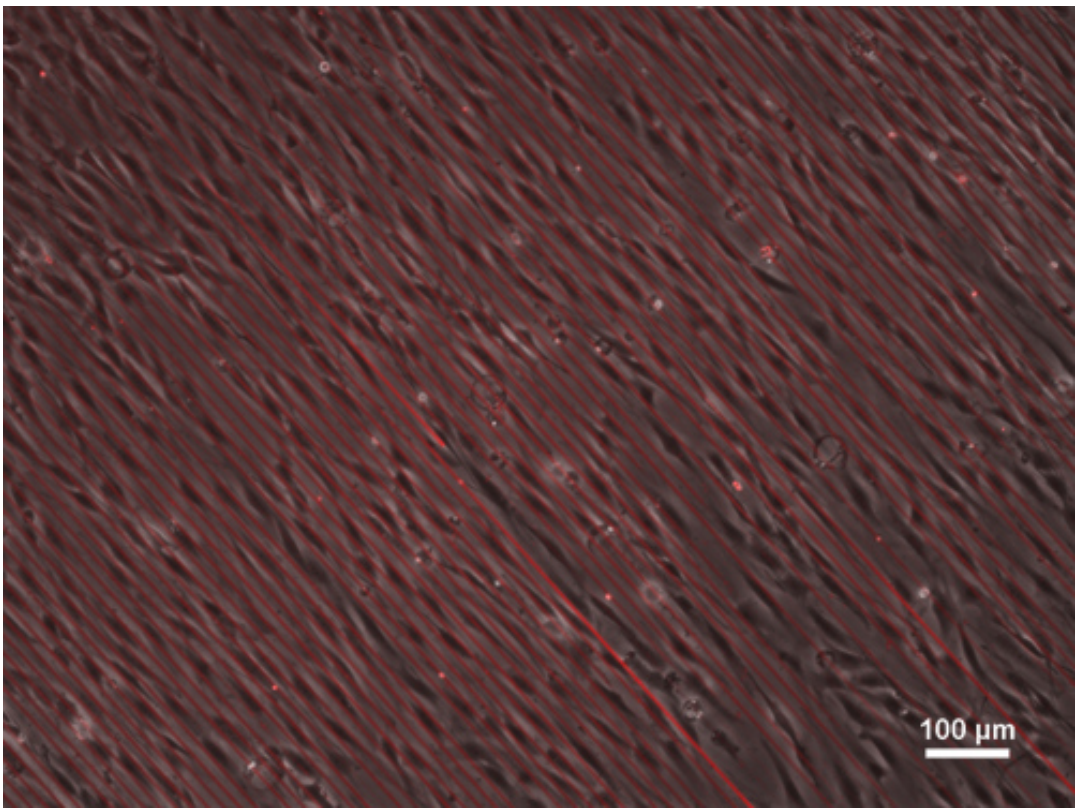

Figure 4-4: Alignment of NIH 3T3 mouse fibroblasts on an array of pNIPAAm structures (4µm width) taken in phase contrast and composited with a fluorescent image of the underlying structures (red). Images taken at 10X and scale bar represents 100µm.

Data collected from image analysis was used to generate angular histograms showing the distribution of cell alignment on both geometries of arrayed surfaces after 24 and 96 hours in culture and is compared to alignment of cells grown on a glass surface in Figure 4-5. All data was normalized such that the orientation of the underlying anisotropy was positioned at 0°. Cell alignment on arrays of 4µm widths was found to be -0.8°±16.8° after 24 hours of culture and 6.0°±28.3° after 96 hours of culture. Additionally, alignment on arrays 8µm widths was found to be -1.3°±13.9° after 24 hours of culture and 7°±25.4° after 96 hours of culture. In contrast, alignment of cells on glass surfaces was found to be -5.3°±52.1°.

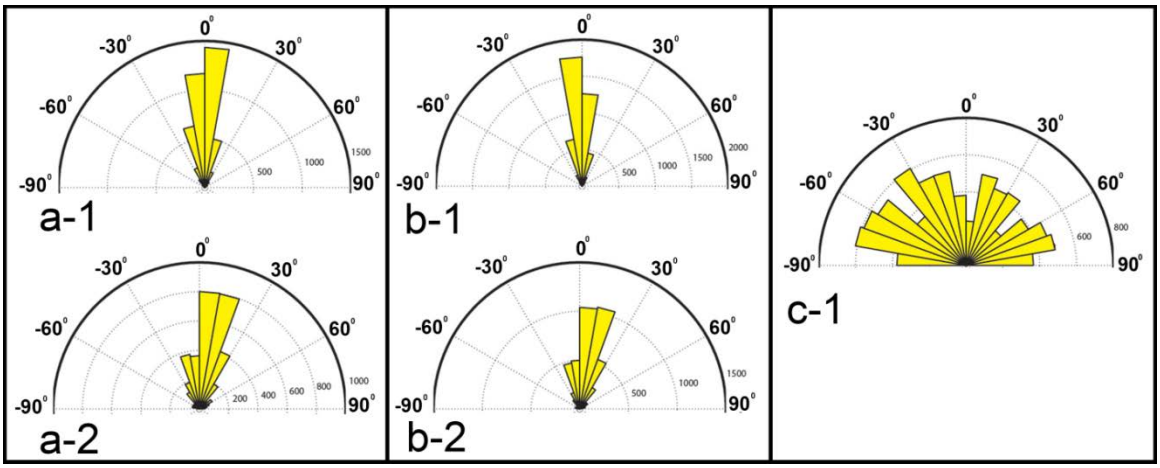

Figure 4-5: Angular histograms showing the orientation of NIH 3T3 fibroblasts on pNIPAAm structures of 4µm (a) and 8µm (b) widths after 24 hours (1) and 96 hours (2) in culture compared to orientation of cells grown on glass control surfaces (c). For patterned surfaces the pNIPAAm structures had an alignment of 0°.

A simple two-sample t-test was performed to assess the comparison between alignments using a significance level (α) of 0.05. From this analysis it was found that mean orientation was unaffected by the difference in pNIPAAm structure width and spacing while there was a significant difference in mean orientation between 24 hours and 96 hours of culture. Although mean values of cell orientation for 24 hour pNIPAAm samples are similar to the mean orientation of cells on the control glass surfaces it is important to note that the angles allowed for measure of cell alignment were in the range from -90° to 90°. It would be expected that anything that is randomly measured in this range would have a value close to the mean of the range (0°) but possess a large variance which can easily be interpreted from the angular histograms in Figure 4-5.

The characteristics of cell shape were evaluated by seeding surfaces, both pNIPAAm arrays and glass, at low cell densities (Figure 4-6). Cell orientation on pNIPAAm arrayed surfaces with widths of 4µm alignment was similar to densely populated surfaces having a mean orientation of -2.9°±14.0° in comparison to control

surfaces, 5.3°±51.6°. In order to elucidate any augmentation of cell shape imposed by the pNIPAAm array the spreading area, minimum ferret, maximum ferret, and circularity of spread fibroblasts was measured after 24 hours of culture. The results of these measurements on pNIPAAm arrayed surfaces can be found in Table 4-1 and are as follows: average spreading area (776.6μm^2), average minimum ferret (18.3μm), average maximum ferret (83.2μm), and average circularity (0.33). In contrast the following was measured on glass surfaces: average spreading area (882.9μm^2), average minimum ferret (24.5μm), average maximum ferret (70.3μm), and average circularity (0.43). In each case comparison of the metrics between pNIPAAm arrayed surfaces and glass surfaces using a two-sample t-test showed that means were significantly different using $\alpha = 0.05$. The results suggest a significant impact on cell shape due to culture on pNIPAAm structures. Spreading area and minimum ferret is reduced by 12% and 25% respectively while maximum ferret is increased by 18%. A decrease in minimum ferret and increase in maximum ferret suggests that cells grown on pNIPAAm structures are more elongated which is in line with the 23% reduction in mean cell circularity.

4.3.2 Cellular Organization on Isolated pNIPAAm Structures

The second series of experiments tested the ability for highly spaced (essentially isolated) pNIPAAm structures to direct alignment of NIH 3T3 fibroblasts. These structures had dimensions of between 50μm, 75μm, and 100μm with heights of approximately 21μm. Qualitatively, culture of cells on these surfaces yielded cells aligned to the long axis of the structure forming “ribbon-like” micro-tissues that extend the length of the beam and are approximately four to 8 cells in width. Analysis of cell

orientation was performed after 24 hours of culture. Cells cultured atop the various widths of pNIPAAm structures are shown in Figure 4-7.

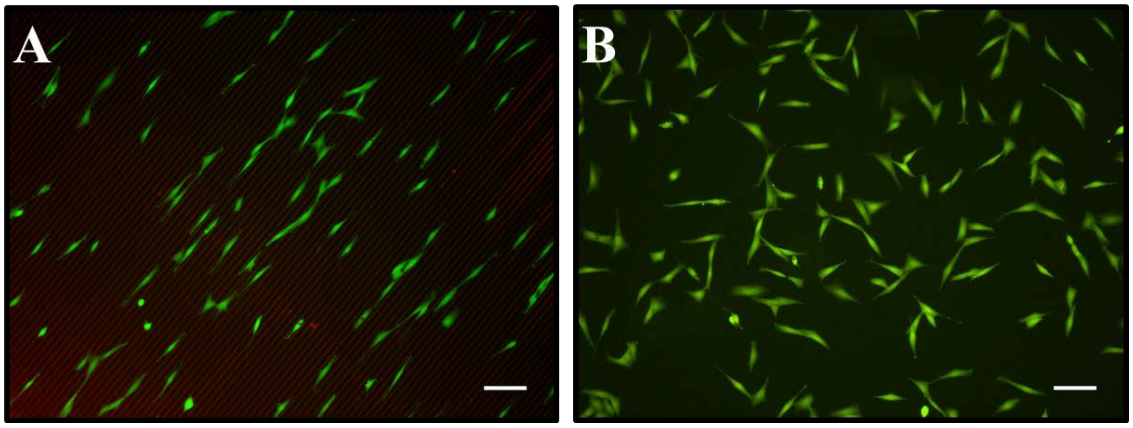

Figure 4-6: Calcein-AM stained NIH 3T3 fibroblasts cultured at low density on pNIPAAm arrays (a) and glass surfaces (b) after 24 hours. Images taken at 10X and size bars represent 100µm.

Table 4-1: Comparison of cell spreading area and shape between fibroblasts cultured on pNIPAAm arrays (4µm width) and glass control surfaces.

	pNIPAAm Array (4µm)	Glass
Avg. Spreading Area (µm^2)	**776.6**	**882.9**
Min. Ferret (µm)	**18.3**	**24.5**
Max. Ferret (µm)	**83.2**	**70.3**
Circularity	**0.33**	**0.43**

For alignment of cells on wide pNIPAAm structures, data was adjusted such that the main axis of the structure lies on 90° and the data ranges from 0° to 180°. Average orientation of fibroblasts on 50µm, 75µm, and 100µm structures was found to be 88.4°±14.2°, 90.8°±11.7°, and 90.3°±13.2° respectively. Histograms showing the distribution of cell orientations are provided in Figure 4-8.

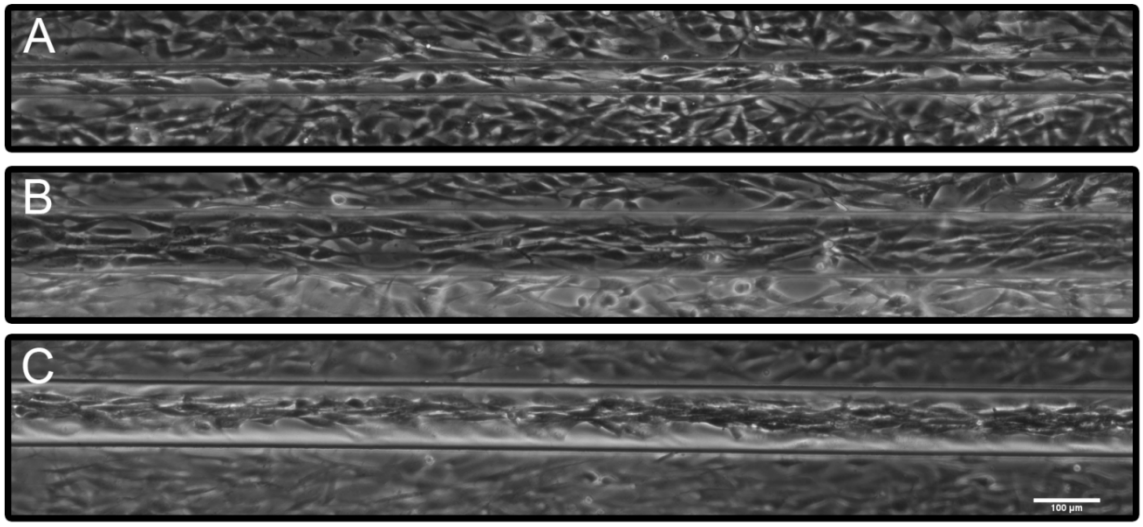

Figure 4-7: Alignment of NIH 3T3 on isolated pNIPAAm beams of varying widths 50µm (a), 75µm (b), and 100µm (c). Images taken at 10X in phase contrast with size bar representing 100µm.

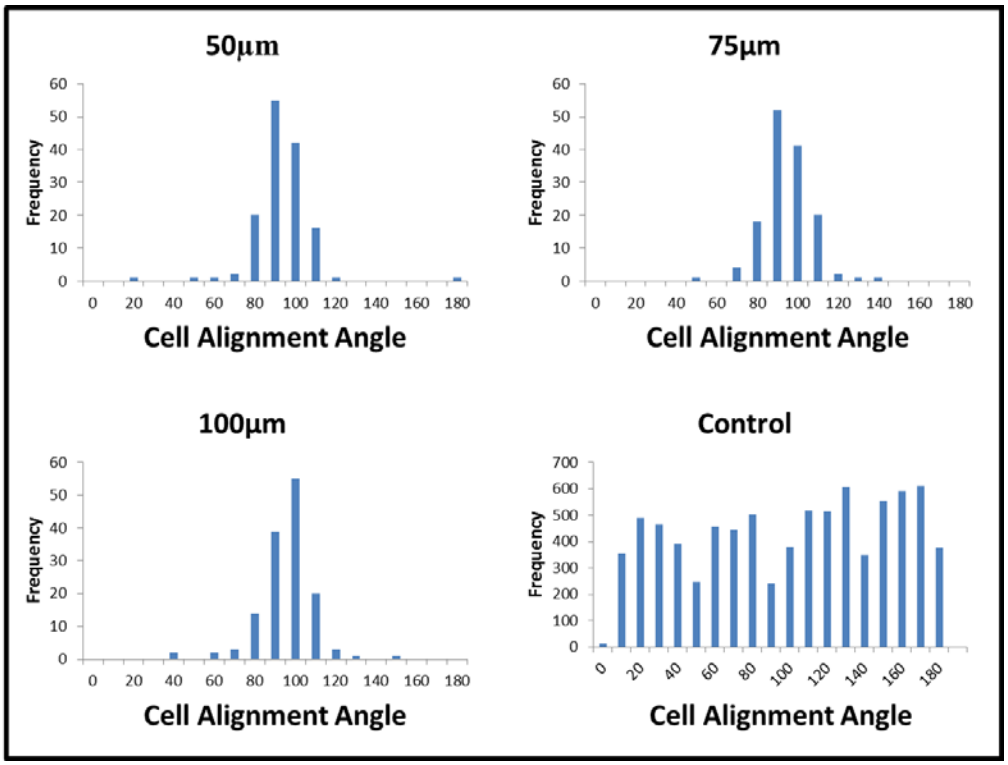

Figure 4-8: Histograms showing the distribution of cell orientation after 24 hours of culture on 50µm, 75µm, and 100µm wide pNIPAAm structures in comparison to glass controls. The orientation of pNIPAAm structures was 90° in each case.

As was performed on orientation data for pNIPAAm arrays, a two-sample t-test was used to determine if there was any significant correlation between mean orientation and structure width on wide structures. It was found that mean orientation was not affected by beam width between 50µm, 75µm, and 100µm wide pNIPAAm structures.

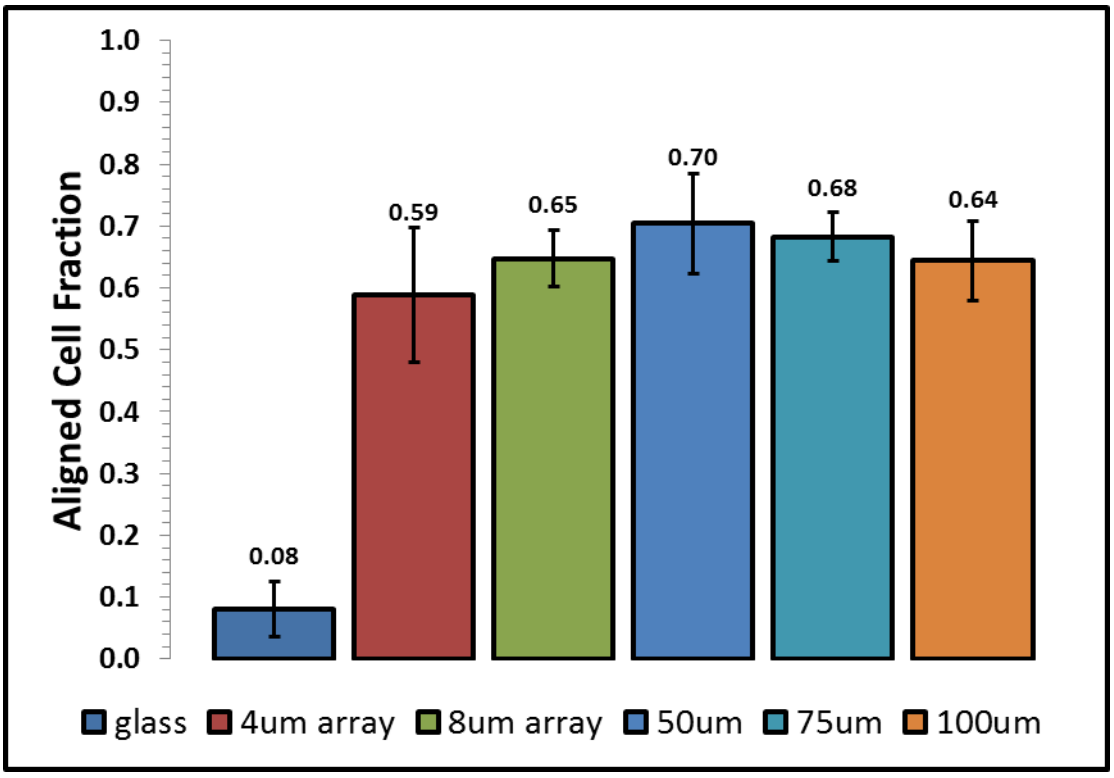

Figure 4-9: The fraction of NIH 3T3 fibroblasts aligned towards the orientation of the underlying pNIPAAm surfaces for the various surface types tested in this study. Cells were considered aligned if their orientation was within 10° of the underlying surface orientation. Error bars represent one standard deviation.

In order to compare alignment on pNIPAAm arrayed surfaces and wide isolated surfaces the fraction of aligned cells was calculated from each data set. Any cell that was oriented within 10° of the underlying surface orientation was considered to be aligned. The results of this are provided in Figure 4-9. This data shows that the overall fraction of aligned cells was greater on wide isolated pNIPAAm structures but the aligned fraction

appears to slightly decrease with increasing structure width. In contrast, on arrayed surfaces, the aligned fraction slightly increases between 4μm arrays and 8μm arrays. In contrast, an analysis of variance test was performed between each set of data alignment. The results of this test suggest that mean aligned fraction was not significantly different ($\alpha = 0.05$) between each structure geometry and differences in the means can be attributed to variance in the data.

4.4 Discussion of Results

Cell alignment has been previously demonstrated on surfaces comprised of grafted thin pNIPAAm films. This has been accomplished by either patterning the grafted domains amongst non-adhesive domains[199, 200], patterning the surface with fibronectin and culturing in the absence of serum [155], or grafting atop an established topography [189]. To date, this study is the first known demonstration of cell alignment on micron-scale three-dimensional surface structures comprised entirely of pNIPAAm. The two primary types of pNIPAAm structure surfaces, closely spaced arrays and wide isolated structures, applied in this study both showed a significant capacity to induce alignment in NIH 3T3 fibroblasts after 24 hours of culture. For all surfaces, mean orientation of cells was within 5° of the orientation of the underlying surface anisotropy suggesting that these geometries are acceptable to produce highly aligned micro-tissues on micron-scale pNIPAAm surfaces. Alignment of cells to the orientation of the underlying pNIPAAm surface in arrayed surfaces showed slight degradation after 96 hours although still remaining within a mean orientation of 10°, a metric used by multiple studies for determining successful alignment [148, 201, 202]. A study conducted by Charest et al.

demonstrated that alignment of both primary myoblasts and C2C12 myoblasts was significantly improved over smooth surfaces on patterned hot embossed polycarbonate surfaces. It was revealed that structures with widths from 5µm to 75µm had a strong influence on primary myoblast orientation while orientation of C2C12 myoblasts was only influenced in structures with widths between 5µm and 25µm. Additionally, it was reported that a width of 10µm was optimal in inducing cell alignment in both cell types [202]. This data is in agreement with our observations of the aligned fraction of fibroblasts on pNIPAAm surfaces. Aligned fraction data in this study shows no statistically relevant differences in fibroblast alignment when comparing each structure width used (4µm, 8µm, 50µm, 75µm, and 100µm widths). This is in contrast to the previously mentioned study, suggesting that cellular alignment of NIH 3T3 fibroblasts on pNIPAAm surfaces is not strongly influenced by structure width within these ranges but may become more important in other cell types. A similar relationship was observed in another study examining the effect of topography on cell alignment in baby hamster kidney cells and Madin Darby canine kidney cells. Although only arrayed surfaces were tested in this study it was shown that for both cell lines there seemed to be optimal alignment between 6µm and 12µm. It was also shown that depth played a much larger role in directing cell alignment over the range from 0.2µm to 1.9µm [148]. In the studies performed on pNIPAAm structures, arrayed surfaces (4µm and 8µm) were ~1µm in height while wider structures (50µm, 75µm, and 100µm) were approximately 20µm in height although no difference in aligned fraction was observed. Although it may be expected that changes in structure height would influence alignment, this may be due to either cell type or to the arrayed nature of shallow structures and the widely isolated nature of wider structures.

Another study testing the width of surface anisotropy where NIH 3T3 fibroblasts were cultured in a patterned three-dimensional matrix of gelatin methacrylate, presented data that shows alignment between structures having widths between 200µm and 50µm [203]. Alignment was observed to decrease with increasing width within this range. This is in contrast with our observations on wide pNIPAAm structures where no statistical difference in mean aligned fraction of cells between 50µm and 100µm widths is observed.

Although the data presented here is very encouraging for the application of micron-scale pNIPAAm structures in the development of organized micro-tissues, it is important to note that culture on these surfaces has some unaddressed challenges. Seeding cells on newly fabricated surfaces rarely results in significant cell coverage independent of cell seeding density. A possible cause for this could be the presence of unpolymerized monomer and initiator left in the material after polymerization, although samples were subjected to a series of rinses. After a few cycles of cell seeding, cell release by trypsinization and chelation, and sample disinfection cell coverage was typically enhanced. Even on samples where cell coverage was acceptable for micro-tissue evaluation, cell coverage was typically not complete as some areas of the sample remained uncovered. The domains where cell coverage was incomplete or absent was not conserved between culture cycles and it seemed that these domains were random. This may be explained by variations in seeding density and cell dispersion as well as the randomness associated with cell settling immediately following cell seeding. Although these issues did arise sufficient cell coverage could be obtained in order to perform analysis of micro-tissues on micron-scale pNIPAAm surfaces. This is in contrast to

observations made on grafted pNIPAAm films. A study aimed at determining the optimal parameters for cell adhesion on grafted pNIPAAm surfaces showed that adhesion dramatically decreases at film thicknesses exceeding 20nm which was greatly attributed to decreased dehydration of pNIPAAm chains as they extend further from the hydrophobic polystyrene tissue culture surface [95]. This study suggests that good cell adhesion is not feasible on thick layers of grafted pNIPAAm which is in contrast to the cell spreading and adhesion observed in micron-scale pNIPAAm layers. Although attaining cell coverage on micron-scale pNIPAAm structures needs to be optimized, it is clear from the results of this work that cell adhesion and spreading on these surfaces is more than feasible, which suggests that from a cell adhesion context micron-scale pNIPAAm surfaces are fundamentally different than grafted thin films.

Data from culture of fibroblasts on micron-scale pNIPAAm structures also shows a significant impact on cell shape. A 25% reduction in minimum ferret and an 18% increase in maximum ferret suggest a lengthening of aligned cells which is further verified by a 23% reduction in circularity. The measured changes in cell shape are extremely similar to the results published by Dalby et al. where primary human fibroblasts were cultured on quartz slides having patterned arrays of 12μm widths and depths of 2μm [204]. Additionally, a strong correlation between cellular alignment and reduction in circularity was observed in NIH 3T3 cells cultured on structures with a width of 50μm [203]. This study also showed that aligned cells experienced a significant reduction in cell spreading area on the quartz arrays, a result which is also observed in cells cultured on pNIPAAm arrays where mean cell spreading area was reduced by 12%. Although the reduction in cell spreading area induced by surface topography is not

completely understood it has been observed in many studies [192, 205, 206]. One study performed, using human fibroblasts on titanium coated surfaces, studied the effects of surface topography on cell shape and reported significant increases in cell height by using scanning laser confocal microscopy [198]. Although cell height was not included in this analysis, these results suggest a similar effect may be occurring on pNIPAAm surfaces and may warrant further evaluation.

Although relationships similar to those observed in this study exist, it is always import to keep in mind that cellular response to topological cues is largely influenced by cell type [148, 202, 205, 207]. The results of this study are positive for application of micron-scale pNIPAAm structures in cultivating micro-tissues for use in tissue engineering and should be applied over a wider range of geometries as well as cell type in order to test the extent of their potential application.

4.5 Summary

In this chapter, the well-studied cellular phenomenon of contact guidance was harnessed in micron-scale pNIPAAm structures of various size and spacing. It was demonstrated that alignment of NIH 3T3 fibroblasts could be accomplished by culture on pNIPAAm surfaces designed in a series of closely spaced arrayed structures as well as wide isolated structures. This allowed the culture of micro-tissues having the form of aligned cell sheets on closely spaced arrays or ribbon-like micro-tissues on wide isolated structures. In addition to cell alignment cell shape was also affected by culture on the surfaces such that cells were more elongated and showed a decreased spreading area in comparison to control surfaces.

Chapter 5: pNIPAAm Structures for Rapid Release of Organized Micro-Tissues

In the previous chapter we discussed various methods behind cell organization with an emphasis on using topographically induced cell alignment by contact guidance on various forms of patterned two-dimensional surfaces. In many cases the two-dimensional substrates were patterned with a three-dimensional topography with length-scales and geometries conducive to inducing cell alignment. While investigation of surfaces which can be used to direct cell organization is important, another important aspect of surface design must be considered; the ability to remove or translocate the organized micro-tissues while limiting any impact on micro-tissue structure and cell health. Application of these surfaces for advanced tissue engineering approaches is significantly retarded without a fruitful way to accomplish this. This chapter discusses some of the current approaches to cell release, or micro-tissue harvesting, and presents a new approach based on micron-scale pNIPAAm structures.

5.1 Engineered Approaches to Harvesting Micro-Tissues

As discussed early in Chapter 4, traditional methods of cell removal from culture surfaces typically involves the use of enzymes such as trypsin and/or chelating agents such as EDTA. Cell removal by these methods disaggregates any engineered organization of micro-tissues due to enzymatic destruction of ECM components and termination of cell/cell contacts [139, 208]. Also, enzymatic removal of cells has been shown to have

significant impacts on cell function [209]. This is not favorable for use with cells which have been cultured on engineered surfaces designed to induce cellular organization as organization will be lost and proper cellular function is questionable.

5.1.1 Mechanical Removal

Mechanical removal of cells from engineered surfaces is another option for harvesting of cultured cells but has shown to yield mixed results [139, 196, 208, 210]. Infrared spectra of human gastric cancer cells, after mechanical harvesting using a scraper, suggested that significant cellular damage occurred due to mechanical removal causing loss of intracellular RNA. Additionally, distinct morphological changes in mechanically removed cells were observed as well as reduced cell density [208]. While mechanical removal is highly invasive to cell survivability it has been shown that post-mechanical removal surfaces are very conducive to promoting growth of new cells most likely due to the presence of lipids which were expelled from broken cell walls [210]. Although this is an interesting result it does not provide any advantage of mechanical removal for subsequent application of harvested cells which are significantly damaged. One study claims successful mechanical removal of organized C2C12 myoblasts cultured on anisotropic PDMS surfaces. Myoblasts were cultured and aligned on PDMS surfaces, allowed to differentiate to form myotubes, and subsequently cultured with fresh cells to repeatedly form a multilayered micro-tissue of myotubes. Mechanical removal of cells was facilitated by a probe with a 5μm diameter and strips of multilayered myotube "bundles" were removed from the surface intact [196]. Although no data was presented to ensure that cell integrity was preserved, it is likely that mechanical removal in this

situation was a viable option as the micro-tissue was well formed in a three-dimensional nature providing increased mechanical stability within the micro-tissue in contrast to removal of planar micro-tissues. Although this may be a viable option for isolated studies, this would be a difficult approach to scale towards high-throughput tissue engineering technologies as very precise tools and human intervention are necessary therefore a more automated and universal approach is desired.

5.1.2 Degradation of Supporting Surface

Another approach to harvesting of micro-tissues has been to engineer a surface that can be dissolved or degraded by a treatment designed to be minimally invasive to the cultured tissue.

In one study a surface was modified with patterned collagen and seeded with mammary epithelial cells to form small islands of cells. Release of the small clusters was accomplished by collagenase-induced degradation of the underlying collagen surface resulting in the release of small cell clusters which were then placed in a three-dimensional collagen matrix [(211)]. While this is an interesting approach, and it appears that cell/cell contacts were preserved and ECM was potentially undisturbed, it resulted in the release of micro-tissues that did not preserve the shape induced by patterning of the surface, limiting its utility for the generation of highly organized micro-tissue constructs. Another study demonstrated the use of pNIPAAm films formed on PDMS which had a patterned surface by first polymerizing the PDMS on a steel block which had a grooved surface due to polishing with sandpaper. The pNIPAAm films were then removed from the PDMS surface leaving behind a patterned pNIPAAm surface. During the process

laminin and collagen IV were adsorbed onto one of the pNIPAAm film surfaces. The films were shown to be suitable for cell culture and possessed the mechanical strength to be manipulated by forceps. Cell laden pNIPAAm films could then be transferred to another surface, allowed to attach to the surface, and the cells could be released from the film by reducing the temperature to 22°C for 2 hours causing the pNIPAAm to dissolve away. Dissolution of the pNIPAAm film was possible as it was not formed into a gel due to the lack of a cross-linking agent during polymerization [212]. Although this is a very novel approach, it is unclear what impact dissolved pNIPAAm chains may have on cell health.

5.1.3 Thermal Activation of Thin pNIPAAm Grafts

One of the most promising strategies towards the non-invasive harvest of cultured cells was pioneered by Teruo Okano nearly 20 years ago [44]. In general, plasma-treated polystyrene culture surfaces were modified by grafting thin films of pNIPAAm onto the surface. The pNIPAAm modified surface remained an acceptable surface for cell culture at culture conditions (37°C) with the added advantage of the built-in responsive nature of the pNIPAAm layer. Through thermal manipulation of the pNIPAAm layer by lowering culture temperature below the demixing temperature (~32°C), a critical shift in the properties of the grafted pNIPAAm surface occurs resulting in controlled release of cultured cells. This method of cell harvest has been widely studied and applied to numerous cell types [47, 91, 93, 94, 97, 155, 190, 200, 213-216]. The process of releasing cells from a culture surface by thermal activation of pNIPAAm surfaces is commonly referred to as cell sheet engineering [45, 94, 96, 97]. Although the exact mechanics behind cell detachment

from grafted pNIPAAm are not fully understood several studies have been performed to elucidate the detachment mechanism. In one study, sodium azide was applied to cells to determine if ATP driven metabolic activity plays a role in detachment [43]. Sodium azide causes a drop in cellular ATP due to its inhibition of cytochrome C oxidase which is the final enzyme required for mitochondrial ATP production [112]. It was found that cell detachment from grafted pNIPAAm surfaces was reduced by 40 – 50% in the presence of 2mM sodium azide. Higher levels of sodium azide were attempted but led to cell damage and release on control surfaces. Although inhibition of release was not complete, potentially due to incomplete inhibition of ATP production, these results suggest that metabolically driven processes are a key aspect to cell release on these surfaces. Additional insights into the mechanism of cell detachment were gained by applying treatment of inhibitors targeting specific cellular functions such as protein synthesis and actin filament depolymerization. It was shown that tyrosin phosphorylation was an important cellular function to cell detachment and suppressing its activity resulted in loss of cell detachment on grafted pNIPAAm. Additionally, inhibition of both the depolymerization and the stabilization of F-actin resulted in reduced cell detachment suggesting that actin dynamics play a role in cell detachment. Through this study it was proposed that cell detachment from grafted pNIPAAm surfaces due to a thermally induced shift in material properties was a two-step process. First, a passive detachment step which is a result in the change in the surface interactions between the pNIPAAm layer and the ECM/cell construct and a second metabolically active detachment step which requires cytoskeletal reorganization and intracellular signal transduction [46].

Many studies have been performed where cultured cell sheets have shown significant success when applied *in vivo* for both animal and human testing. A few examples of the application of cell sheets released from grafted pNIPAAm surfaces include: hepatic tissue (liver) [213] neonatal rat skin fibroblasts for lung repair [216], oral mucosal epithelium for corneal reconstruction in human patients [21], and mesenchymal stem cells for treatment of infarcted rat hearts [217]. These successes demonstrate the inherent advantages of cell release without the need for chemical or harsh mechanical processes as well as the capacity to deliver micro-tissues intact and without any non-native biological or synthetic components.

5.2 Cell Release on Micron-Scale pNIPAAm Structures

In the following sections, results of cellular detachment of NIH 3T3 fibroblasts will be discussed and a new mechanism of cell detachment from micron-scale pNIPAAm structures will be suggested. As previous studies have suggested, pNIPAAm is a highly suitable material for culture and recovery of micro-tissues but to date no studies have been published testing the ability for micron-scale pNIPAAm topographies to induce cellular organization and recovery. The previous chapter outlined the capacity for these surfaces to induce cellular organization and the subsequent sections of this chapter will outline its capacity to rapidly harvest organized micro-tissues.

5.2.1 Cell Release from pNIPAAm Arrays

Three-dimensional micron-scale structures comprised of pNIPAAm were chosen as a suitable platform for cellular organization and release. Release of micro-tissues

formed on pNIPAAm structures was induced by shifting culture temperature with cold DPBS to ~28°C on a microscope stage to evaluate the effects of release due to thermally initiated pNIPAAm swelling by sequential capture of images or video acquisition. Release of an aligned sheet of fibroblasts is presented in Figure 5-1. Release of the aligned micro-tissue after 24 hours of culture was nearly instantaneous releasing within 1 second after application of cold DPBS. As the micro-tissue released it began to contract and ultimately formed a coiled or wrapped structure.

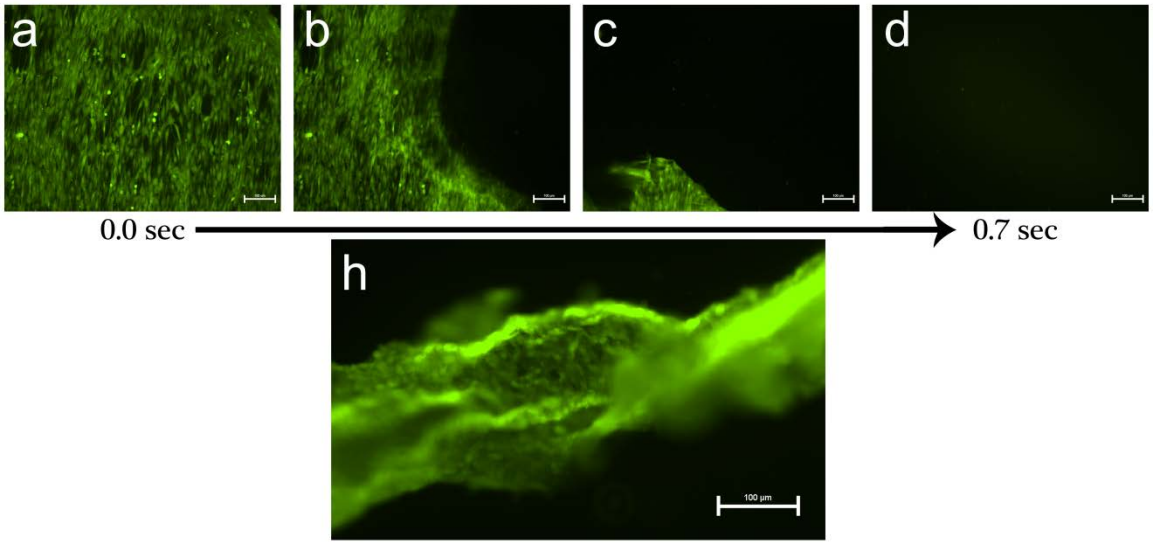

Figure 5-1: Release of an aligned sheet of NIH 3T3 fibroblasts from an array of pNIPAAm structures (4µm). Cells were stained with calcein-AM and cultured for 24 hours with detachment occurring in under 1 second (a-d) and the resultant released tissue in a coiled confirmation (h). Size bars represent 100µm

To elucidate if the effects of DPBS flow into the culture dish assisted in the rapid release of the aligned sheet, aligned cells were allowed to cool from culture temperatures under the thermal gradient of room temperature (~26°C). After 3 minutes disassociation of the cell sheet from the pNIPAAm array was in progress as presented in Figure 5-2. It is

important to note that complete detachment of aligned sheets without forces provided by gentle agitation with cold DPBS was typically incomplete. This may be due to ECM continuity and cell contacts between the aligned micro-tissue and the cells bound to the glass surface bordering the pNIPAAm array as these structures are only ~1µm in height.

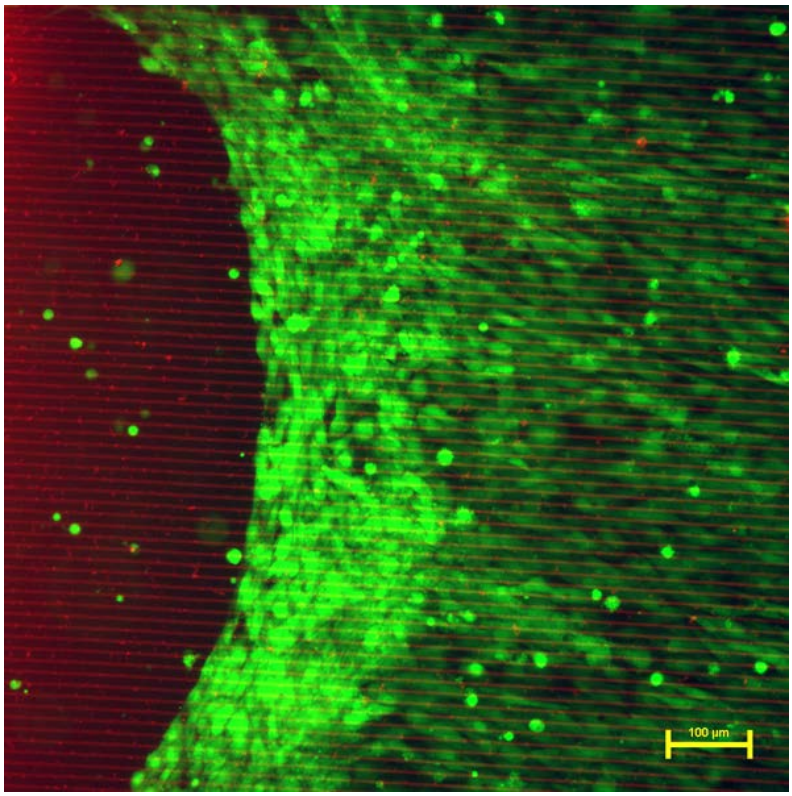

Figure 5-2: Release of NIH 3T3 fibroblasts on a pNIPAAm array (4µm) after unaided cooling from culture temperature to room temperature for 3 min. Size bar represents 100 µm.

Although release of micro-tissues from the surface of pNIPAAm arrays has been demonstrated, it is important to note the capacity of this approach towards dictating the boundary shape of the aligned micro-tissue. Figure 5-3 shows the removal of an aligned micro-tissue at one of the outer boundaries of the array. This shows that cells are readily detached from the pNIPAAm array while leaving cells bound to the periphery glass

virtually unchanged demonstrating the capacity of these patterns to dictate the peripheral shape of the released micro-tissue.

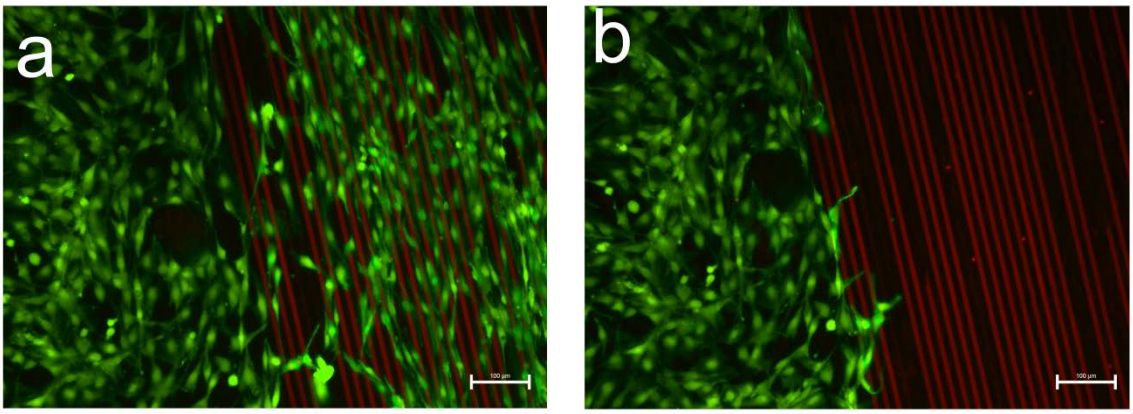

Figure 5-3: Release of an aligned micro-tissue shown from the boundary of the pNIPAAm array. Size bar represents 100µm.

5.2.2 Cell Release from Wide Isolated pNIPAAM Structures

Release of organized micro-tissues was also tested on wide isolated pNIPAAm structures. These structures have a height of 22µm, far greater than the pNIPAAm arrays (0.8µm), and typically release was unhindered by any peripherally glass bound cells. Similar to release of micro-tissues on arrayed pNIPAAm surfaces, release was initiated by addition of cold DPBS to reduce the culture temperature to ~28°C. Release of an aligned "ribbon-like" micro-tissue from a 100µm wide pNIPAAm structure is presented in Figure 5-4. Typically within 10 seconds of shifting the culture temperature noticeable expansion of the underlying pNIPAAm structure begins. As the structure begins to swell, retraction of the overlying micro-tissue is initiated. Although the cells are released from the surface, the micro-tissue acts as a single entity and cells within it appear to remain attached to one another. This suggests that cell/cell contacts and potentially ECM is

undamaged and the overall integrity of the micro-tissue is preserved. In most cases, significant cell detachment was observed 3 minutes post-swelling. Although a majority of the micro-tissue detaches from the surface, complete disassociation of the micro-tissue from the surface was rarely observed suggesting that small portions of the micro-tissue remain attached and inhibit complete micro-tissue release into the bulk. Although detachment may not be complete, gentle agitation of the surface by fluid flow with a pipette or shaking of the culture dish generally assists complete disassociation suggesting that the contact points are few and weak.

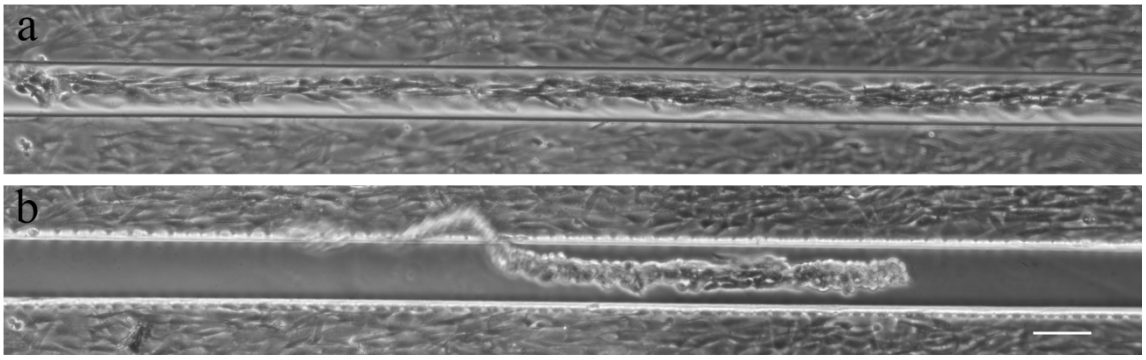

Figure 5-4: Thermally induced detachment of a ribbon-like micro-tissue from a wide pNIPAAm structure. A 100µm wide pNIPAAm structure (ε=0.42) shown pre-swelling (a) and 3 minutes post-swelling (b). Size bar represents 100µm.

A time-lapse of the detachment process is shown in Figure 5-5 to demonstrate the progress of cell detachment over a 3 minute period following thermally induced swelling of the pNIPAAm structure. Significant changes in the micro-tissue orientation and structure follows only 30 seconds after applying cold DPBS. Cells begin to contract and round. The micro-tissue begins to shrink as cell contacts with the surface are disturbed and internal tensile forces are translated into micro-tissue retraction as the cell loses traction. Cell release data collected on well-populated 75µm and 100µm width samples

with a swelling induced surface strain (ε) above 0.3 showed that mean area of cell detachment was 85% after 3 minutes post-swelling. Although quantitative data was not acquired, samples which had been cultured for 48 hours or more showed slightly different results. Some samples released cells in a similar fashion to those cultured for 24 hours while others showed virtually no cell release. Although the exact reasoning for this has yet to be determined it may be due to excessive buildup of ECM as it was also observed that the pNIPAAm structures on these samples showed little to no surface strain upon swelling.

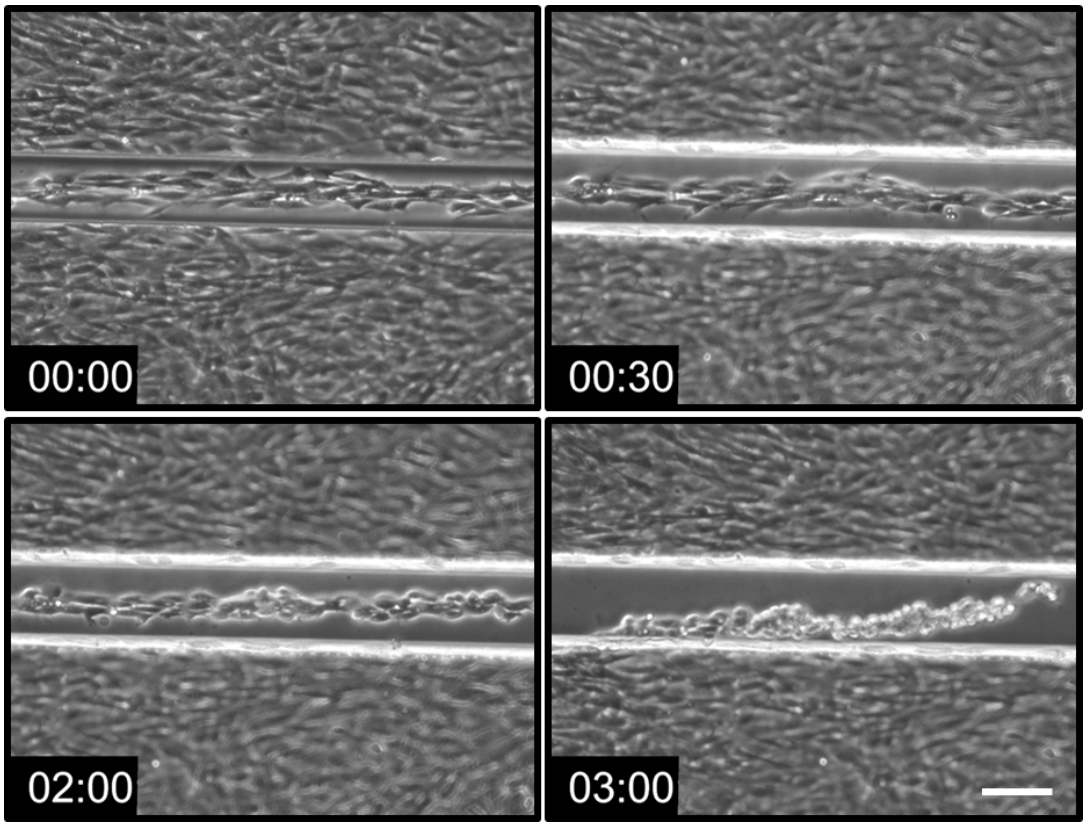

Figure 5-5: Swelling induced release of a ribbon-like micro-tissue comprised of aligned fibroblasts grown atop a 100µm wide isolated pNIPAAm structure 0min, 0.5min, 2min, and 3min post swelling (ε=0.39). The final frame (3min) was taken at a location a few hundred microns to the left of the other images to follow the retracting micro-tissue. Size bar represents 100µm.

In addition to detachment of well-formed ribbon-like micro-tissues, detachment of cells on a sparsely populated pNIPAAm structure was also observed (Figure 5-6). Cells which are closely spaced (as shown on the left portion of Figure 5-6) detach in a similar fashion as those in well-formed micro-tissues suggesting that shared ECM is releasing in tandem with cell release and, while holding adjacent cells together, facilitate forces responsible for cell detachment. In contrast, cells which are more isolated either spontaneously detach or round up on the surface.

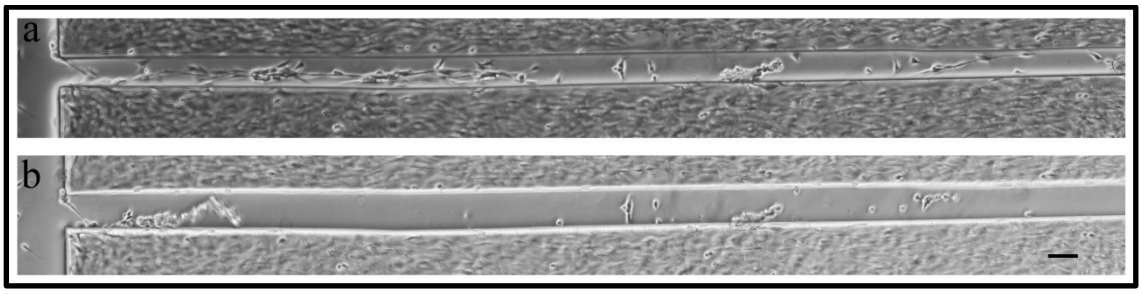

Figure 5-6: Detachment of cells from a sparsely populated 100μm pNIPAAm structure (ε=0.41) showing cells pre-swelling (a) and 3 minutes post-swelling (b). Size bar represents 100μm.

Partial cell release was also observed on structures with smaller widths (20μm). Although a complete analysis of cell detachment on these structures was not performed, observations are presented here. Qualitatively, cells elongated along the pNIPAAm structure's long axis to form micro-tissues with a "fiber-like" geometry. Micro-tissue fibers were no more than 3 cells in width, more typically one or two, and many cells in length. Due to the severely reduced width in these pNIPAAm structures lateral swelling no longer dominates the geometry of the final swollen structure as discussed previously. In fact, these high aspect ratio structures experience a bulk buckling instability upon swelling. Fibroblasts still partially attached to high aspect-ratio pNIPAAm structures,

post swelling, are provided in Figure 5-7. Although detachment is incomplete, a significant portion of both isolated cells and fiber-like micro-tissues detach such that a majority of the cell bodies are suspended between buckles.

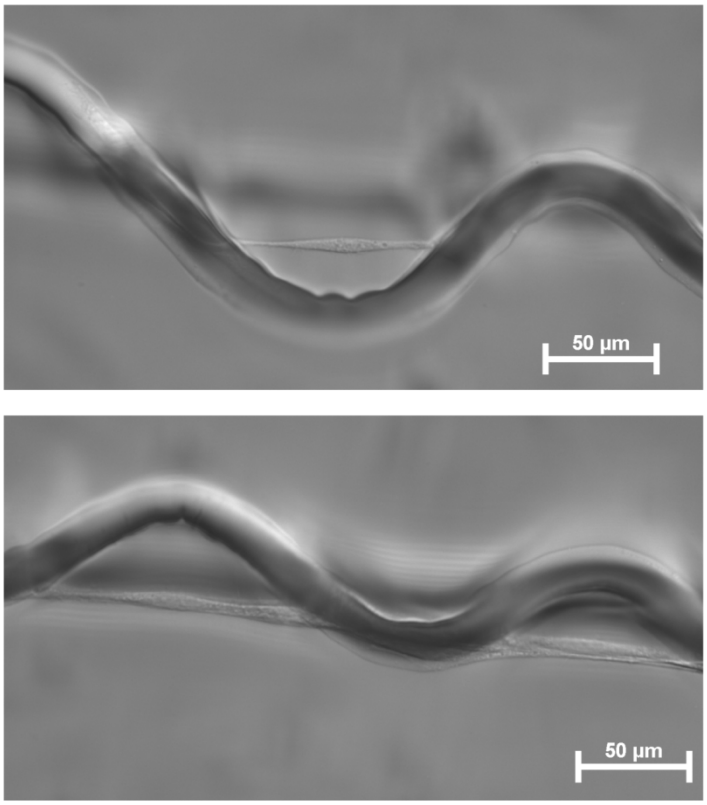

Figure 5-7: NIH 3T3 Fibroblasts grown on 20µm wide pNIPAAm structures after thermally initiated swelling. Size bars represent 50µm.

5.2.3 Mechanism for Cell Release

Previous studies on thin grafted pNIPAAm films aimed at elucidating the mechanism of thermally induced cell detachment from pNIPAAm surfaces have come to address two primary components involved in the process. The first component is driven by a change in the hydrophobicity of the surface while the second involves metabolically active processes within the cell which lead to a rearrangement of the cellular cytoskeleton

[46]. After having demonstrated reasonable micro-tissue release from micron-scale pNIPAAm structures it became a focus of this work to understand the mechanism of cell detachment from these surfaces in comparison to grafted films. Two primary observations revealed that the mechanisms may be completely different. First, cell release from micron-scale structures is much more rapid than release reported from grafted films. For instance, release from wide isolated pNIPAAm structures is, in most cases, nearly complete within 3 minutes (Figure 5-5) while release from grafted surfaces can take from 15 minutes to over an hour [43, 93, 210, 213, 217]. Second, release from pNIPAAm films is generally performed by shifting surfaces from culture temperature (37°C) to 20°C or below while release from micron-scale pNIPAAm structures is managed by only shifting culture temperature to ~28°C. Additionally, it was noted that in some experiments documenting cell release from wide isolated pNIPAAm structures, cell release was retarded on samples which exhibited a low swelling ratio resulting in a low degree of surface strain. These observations are in contrast to detachment of cells on grafted films of pNIPAAm and warranted further investigation. Due to the rapid nature of cell release in micron-scale pNIPAAm structures it is believed that metabolic processes play a diminished role, if any at all. Rather, it is hypothesized that cell release from these surfaces is primarily facilitated by the swelling induced expansion, or strain, of the structure surface. Swelling of thin grafted pNIPAAm films results in very little geometric augmentation within the length scale of the cell. Micron-scale pNIPAAm structures, on the other hand, experience changes in shape and geometry on the scale of the cell and are therefore capable of producing shear forces which have potential to impact interactions between the ECM/cell complex and the surface. In order to test the strain-induced

detachment hypothesis as a potential mechanism to explain cell release from micron-scale pNIPAAm structures, wide isolated surfaces were designed to exhibit various degrees of surface strain by adjusting the cross-link density from 1% - 4%. This resulted in structures with surface strains ranging from 0.12 to 0.71. Additionally, the role of metabolic activity was assessed by incubating cells with sodium azide prior to release, as sodium azide plays an important role in cellular ATP production and was used in previous work to demonstrate the contribution of metabolic activity in cell release on grafted pNIPAAm surfaces [(43)]. Finally, Y-27632, an inhibitor of Rho-associated protein kinases, was used to treat cells prior to thermally-induced swelling to determine if the mechanical properties of the cell play a role in detachment.

Data measuring the percent reduction in attachment area of micro-tissues on surfaces of varying degrees of surface strain, after 3 minutes of swelling, is provided in Figure 5-8. Evaluation of this data uncovers a strong relationship between detachment and degree of surface strain. It was anticipated that cell detachment would vary in tandem with strain; however, it appears that there is a range between strains of 0.2 and 0.3 where there is a critical shift in the degree of detachment. Taking a strain of 0.3 to be a critical boundary for active detachment, averages of micro-tissue detachment area were calculated. For strains above 0.3, average detachment area was 85%±16% while for strains below the critical strain, average detachment area was 10%±24%. The large variance in low strain samples is due to the two points within a transition range between good and poor detachment but were included in the average as they fell below the established critical strain.

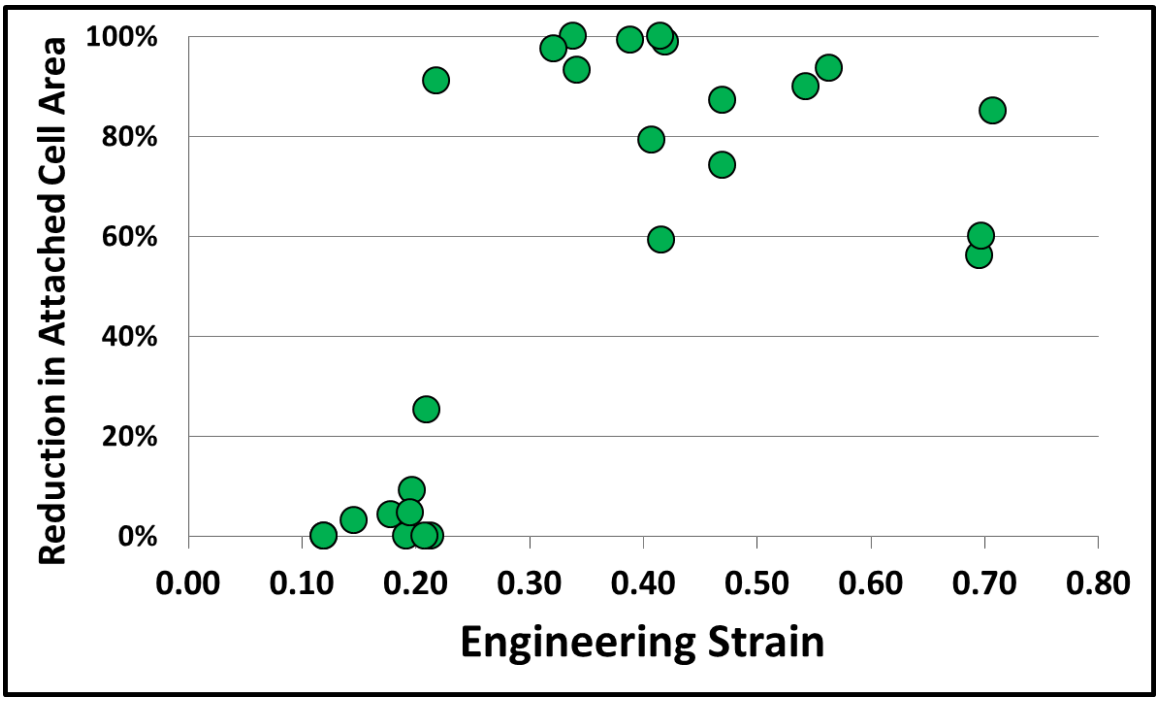

Figure 5-8: Measure of the detachment area of micro-tissues on wide pNIPAAm structures after 3 minutes of swelling as a function of swelling-induced surface strain.

Although detachment from micron-scale pNIPAAm surfaces was not observed at strains below 0.3 within 3 minutes post-swelling, observations were made for durations exceeding 30 minutes of low temperature treatment to test if detachment from low strain surfaces would propagate with time as seen in detachment from thin, grafted, pNIPAAm films. A sample with a surface strain of 0.18 is presented in Figure 5-9 prior to swelling and after 3 and 35 minutes post-swelling. Figure 5-9 shows that detachment of micro-tissues on low strain pNIPAAm surfaces is negligible even 35 minutes after swelling while maintaining low temperature treatment. This suggests that the mechanics which dominate cell release from thin, grafted, pNIPAAm surfaces may not be present in micron-scale surfaces.

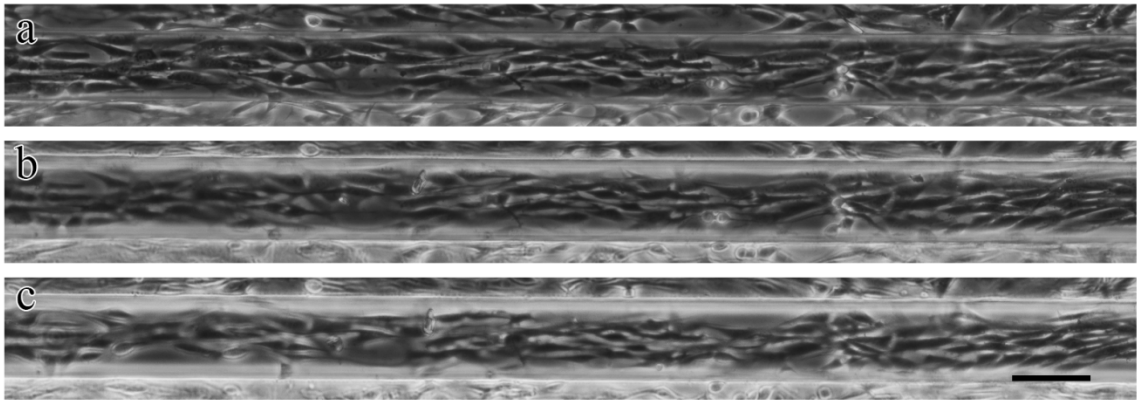

Figure 5-9: Micro-tissue grown atop a 100µm pNIPAAm structure prior to thermally-induced swelling (a) and after swelling for 3 minutes (b) and 35 minutes (c). Surface strain is 0.18 and size bar represents 100µm.

To address the potential effects of cellular metabolism on detachment of cells from wide pNIPAAm surfaces, micro-tissue detachment area was evaluated in micro-tissues exposed to sodium azide for 60 minutes. These tests were performed on samples having swelling-induced surface strains ranging from 0.17 to 0.66. The results of these experiments are provided in Figure 5-10. A critical change between detaching and non-detaching micro-tissues at a surface strain of approximately 0.3 was again observed. Cell detachment area at strains exceeding 0.3 was an average of 84%±11%. This suggests that detachment of sodium azide treated micro-tissues act in a similar way to non-treated samples and further suggests that ATP driven metabolic processes play a diminished role, if any, in cell detachment from micron-scale pNIPAAm structures. Additionally, these results reinforce that expansion of the surface, or surface strain, plays an important role in micro-tissue detachment due to mechanical forces which arise, even under conditions where cellular process which require ATP are diminished.

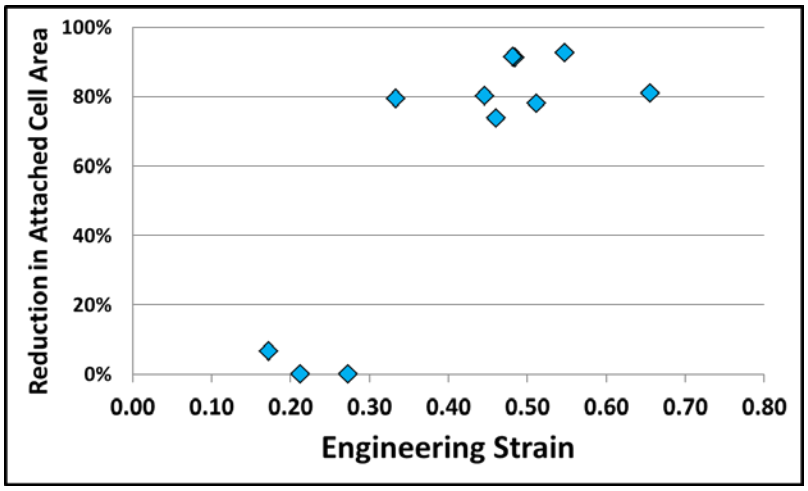

Figure 5-10: Measure of the detachment area of sodium azide treated micro-tissues on wide pNIPAAm structures after 3 minutes of swelling as a function of swelling-induced surface strain.

If cellular release from micron-scale pNIPAAm structures is driven by mechanical forces, it is important to further query the process by augmenting the mechanical characteristics of the attached cells. This was accomplished by treating micro-tissues attached to wide pNIPAAM structures with Y-27632, a compound known to inhibit stabilization of components of the cytoskeletal structure and reduce traction forces between cells and the surface. The results from this test are presented in Figure 5-11. Average cell detachment area was found to be only 1%±4%. The results show practically no appreciable reduction in cell attachment area when treated with the Rho-associated protein kinase inhibitor. In fact in some samples a slight increase in cell attachment area was observed suggesting that upon straining of the pNIPAAm surface cells stretched in tandem with the surface. Images comparing the effect of thermally-induced surface strain on cell detachment for cells treated with sodium azide, Y-27632, and untreated micro-tissues are presented in Figure 5-12.

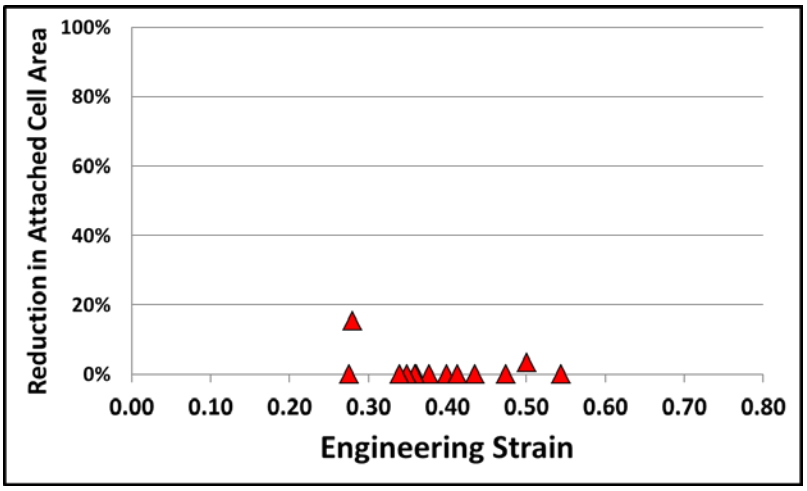

Figure 5-11: Measure of the detachment area of Y-27632 treated micro-tissues on wide pNIPAAm structures after 3 minutes of swelling as a function of swelling-induced surface strain.

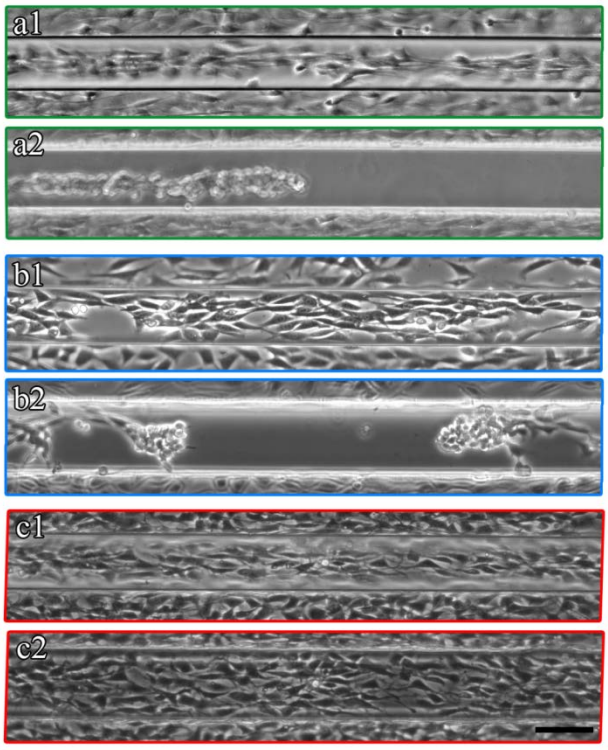

Figure 5-12: Micro-tissues grown atop 100µm isolated pNIPAAm structures in the culture state (1) and the thermally-induced swollen state (2) for untreated cells (a) and cells treated with sodium azide (b) or Y-27632 (c). The average surface strain due to swelling for these samples is 0.35±0.03.

5.3 Discussion of Results

Results obtained by testing micro-tissue release from micron-scale pNIPAAm structures demonstrate that rapid release can be obtained by shifting culture temperature from 37°C to ~28°C. Complete release from pNIPAAm arrays was typically facilitated by gentle agitation through tapping of the culture dish or light shear by pipetting. When cold DPBS fluid was lightly pipetted over the surface, micro-tissue sheet detachment was extremely rapid and occurred within a second. If samples were allowed to cool unaided at room temperature, cell release was initiated and the cell sheets began to detach in some areas of the sample but detachment was usually incomplete and ceased (Figure 5-2). This is probably due to the scale of these patterns. Arrays of pNIPAAm are about 1μm in height from the surface which would allow for significant association between cells in the aligned micro-tissue and cells attached to the periphery glass potentially stabilizing the retracting tissue and preventing complete release. When fluid is flowed over the surface fluid can flow underneath the detaching tissue allowing for significant forces to influence the sheet and disassociate it from the peripheral anchored cells. This suggests that future design of these surfaces may include for an increase in pNIPAAm array height in order to minimize interactions between organized micro-tissues and cell growth on peripheral substrates. Release from arrayed surfaces in this manner is much more rapid than release from wide isolated pNIPAAm structures. This may be due to a few variables. First, attachment area between the micro-tissue and the surface is greatly reduced in arrayed surfaces due to the gaps between pNIPAAm structures. This not only reduces micro-tissue attachment area but also allows for flow of solvent underneath the sheet as cold DPBS is added to the sample and as the sheet detaches. Secondly, because the cross-

sectional area, and overall volume, of structures in the pNIPAAm array is far less than in wide structures, swelling rate would be far greater in arrayed structures which could address the increase in detachment rate. Additionally, it was shown when detachment from pNIPAAm arrays is complete, cells on the periphery of the array remained attached to the glass. This gives evidence that sheets of various peripheral geometries can be formed and released for greater control over the organization and shape of organized micro-tissues.

Release from wide isolated pNIPAAm structures was rapid in nature when compared to traditional release from grafted pNIPAAm films. Micro-tissue release was typically initiated within 30 seconds (Figure 5-5) and complete within approximately 3 minutes. Interestingly, release of cells typically began by release of a portion of the micro-tissue which then began to retract down the length of the structure as subsequent cells in the micro-tissue detached. Typically, when micro-tissue retraction reached a certain point (sometimes at the end of that particular micro-tissue) detachment would cease and the entire retracted micro-tissue would remain anchored at that point. Subsequent agitation of the surface through tapping of the sample or gentle agitation with a pipette resulted in complete release of the micro-tissue. Although in many cases complete detachment of micro-tissues is desired, this form of partial detachment could be advantageous for the selective isolation of single micro-tissues. If it remains slightly attached at a point it could be feasible to harvest a single micro-tissue by extracting the partially released tissue from the surface by simple acquisition through pipetting under a microscope.

Cell detachment from narrow isolated pNIPAAm structures differed from detachment in wide isolated structures. Cells detached from various portions of the structure as it buckled but appeared to remain attached at certain points resulting in cells suspended between buckles on the swollen structure. In addition to use for cell printing, as will be discussed later, this process has potential to be used to study the mechanical properties of cells.

Cell release has been performed on pNIPAAm surfaces for nearly 20 years. This technique was pioneered by Okano in the early 90's by demonstrating that cells grown on grafted pNIPAAm tissue culture surfaces could be released by low temperature treatment [44]. Typically low temperature treatment is performed at 20°C or below and cell release can take between 15 minutes and over an hour [43, 93, 210, 213]. One study showed that the temperature of the treatment depends on cell type such that temperature treatment was optimized in order to induce the greatest degree of cell detachment. It was suggested that this was caused by a delicate balance between hydration of the underlying pNIPAAm layer and the metabolic activity of the cells. At lower temperatures, hydration is more complete but cell metabolism slows. Providing additional proof that cell detachment from grafted films requires both cell metabolism and surface hydration [43]. Early experiments required extended periods of cold temperature treatment in order to detach cell sheets. The rate of cell detachment was improved by altering the grafted pNIPAAm layer through generating porous grafted membranes to enhance hydration rates of the pNIPAAm surface [93] or co-polymerization with 2-carboxyisopropylacrylamide to augment the hydrophobicity change [218]. These conditions raise important questions when considering the application of cells released from grafted pNIPAAm layers for

tissue engineering purposes. Exposing cells to low temperature environments can significantly impact cellular functions such as transcription, translation, metabolism, and cellular cytoskeleton and it is unclear how this may impact subsequent use and value of the harvested micro-tissue [219-221]. In contrast, cell release from micron-scale pNIPAAm structures has been demonstrated by treating cells at temperatures much closer to culture temperatures (~28°C) and for much shorter durations (3 minutes or less). This serves to reduce the potential impact of low temperature treatment on cell health and function while still generating harvestable, organized, micro-tissues. Another complication which arises when considering cell release from pNIPAAm surfaces is the retraction and aggregation of the cell sheet. A common method used to prevent this from occurring during release from grafted pNIPAAm films is to use a supporting structure to release the cells onto as detachment occurs, preventing retraction of the cells as they lose traction with the pNIPAAm surface. For instance, in one study shrinking of cardiac myocytes upon release was prevented by using chitin membranes which aided in preventing micro-tissue shrinkage and facilitated translocation of the cell sheet to a fresh culture surface [214]. A similar issue faces cell release from micron-scale pNIPAAm structures as micro-tissues retract and shrink upon release causing them to lose their peripheral shape. This makes the micro-tissue less useful for applications where precise spatial organization is desired. To prevent this, a novel micro-contact printing technique was developed where cells can be translocated directly from pNIPAAm structures to a desired surface without the need for an intermediate transfer surface. The finer details of this technique will be discussed in the next chapter.

There also appears to be a significant difference in the mechanism behind detachment of micro-tissues from micron-scale pNIPAAm surfaces in contrast to detachment from grafted thin films. In grafted thin films, results from numerous studies suggest that detachment is the result of two distinct processes: metabolically driven cellular functions which require ATP, such as cytoskeletal reorganization, and changes in the hydration state of the pNIPAAm surface [43, 46]. This work has demonstrated that reduction in metabolic activity, through reduction of ATP production by treatment with sodium azide, had little to no impact on micro-tissue detachment from micron-scale structures. Rather, the data presented here suggests that the mechanism for detachment is strongly related to the degree of surface strain generated by expansion of the surface resulting from the thermally initiated swelling of the pNIPAAm structure. This is most likely caused by a balance between the tension forces between the cell and surface generated by focal adhesions and actin filaments (stress fibers) and the sheer stress generated by the expansion of the underlying surface. Additionally, treatment with Y-27632 retarded cell detachment from the surfaces with strains above the critical strain of 0.3. Data from micro-tissue response to various degrees of surface strain on: pNIPAAm structures for control, sodium azide treatments, and Y-27632 treatments are combined in Figure 5-13. Here it can easily be concluded that the strain of the surface plays a dominant role in micro-tissue detachment independent of treatment with sodium azide. In contrast, interfering with cellular contractility through Y-27632 treatment severely impacts the efficiency of micro-tissue detachment. This further suggests that mechanical forces drive detachment.

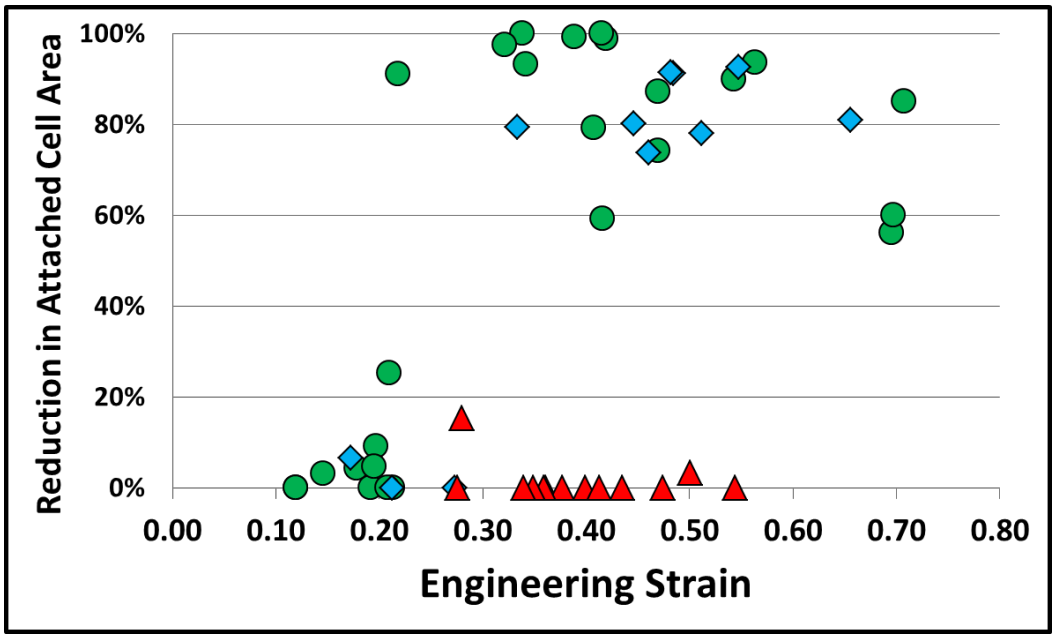

Figure 5-13: Combined data showing the effects of thermally induced strain of pNIPAAm surfaces on micro-tissue detachment in cells treated with sodium azide (♦), Y-27632 (▲), and untreated (●).

Y-27632 inhibits Rho-associated protein kinases specifically p160ROCK [(111)]. Amongst other cellular changes, inhibition by Y-27632 causes a reduction in actin-myosin contractility and ultimately intracellular tension [(222)]. This leads to a reduction in cellular resistance to stretching and thus more compliant to stresses generated by the strain of the underlying surface. In fact, image analysis of cells on swollen pNIPAAm structures after treatment with Y-27632 suggest that cells slightly deform as the swelling-induced strain is applied. This results in a slight increase in average cell coverage area post-swelling as shown in Figure 5-14. Images of pre-swelling and post-swelling micro-tissues treated with Y-27632 are presented in Figure 5-15 where slight deformation of the cell bodies in the micro-tissue is observed.

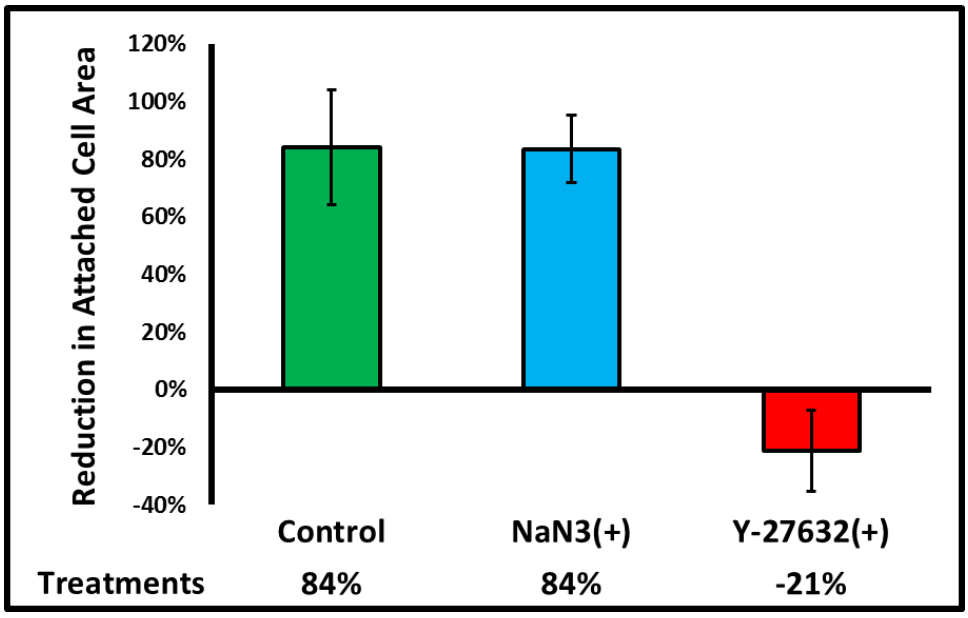

Figure 5-14: Reduction in cell attachment area for micro-tissues on pNIPAAm surfaces with strains exceeding 0.3. Error bars represent 1 standard deviation.

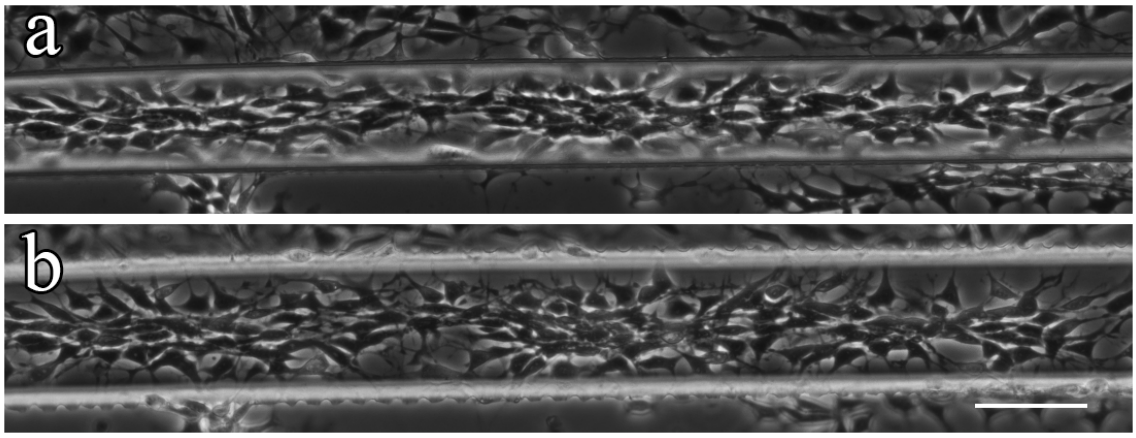

Figure 5-15: A micro-tissue treated with Y-27632 grown on a micron-scale pNIPAAm structure 100µm in width after 24 hours of culture before (a) and after (b) thermally-induced swelling showing slight deformation in the constituent cell bodies. Size bar represents 100µm.

Another interesting observation arising from this study was the general lack of detachment observed in micro-tissues on wide micron-scale pNIPAAm structures which

experienced levels of surface strain below 0.3 even after over 30 minutes of low temperature incubation (Figure 5-9). Although detachment after lengthy low temperature incubation was not always completely retarded, if any detachment was observed it was extremely incomplete. This is in contrast to detachment on grafted films where detachment is typically observed within 30 minutes. It would be prudent to assume that the mechanism of cellular detachment proposed on grafted pNIPAAm films may also apply to micron-scale structures, if detachment is not first induced by forces generated by the expanding surface between the micro-tissue and the pNIPAAm surface during swelling. This discrepancy may be attributed to the higher temperatures at which release was performed or suggest that the mechanism which governs detachment from grafted films is highly diminished or non-existent in micron-scale structures.

5.4 Summary

Micro-tissue release from micron-scale pNIPAAm structures has been demonstrated on both closely spaced arrays and wide, isolated, structures. Although in some cases complete detachment of the micro-tissue was incomplete, detachment was sufficient enough to facilitate complete removal of the micro-tissue by gentle agitation. Cell release from these surfaces requires less reduction in culture temperature and detachment is more rapid than reported on grafted pNIPAAm films making these surfaces attractive for further study, as impacts on cell health and function can be minimized. Additionally, it was found that the mechanism of cell detachment from micron-scale surfaces differs from grafted films. In contrast to grafted films, inhibition of metabolic activity through reduction in cellular ATP production had no observable effect on micro-

tissue release. This suggests that cellular functions may not play an important role. However, the degree of swelling-induced surface strain did appear to have a significant impact on micro-tissue release where a critical strain between 0.2 and 0.3 seems to dictate successful release. This suggests that detachment in micron-scale structures is governed by mechanical forces rather than the two step hydration/cytoskeletal-reorganization model proposed in grafted thin films.

Chapter 6: Translocation of Organized Micro-Tissues by Micro-Contact Stamping

Exploration of methods to induce cellular organization and release of cultured cells in a minimally invasive fashion has been carried out for over two-decades, yielding a handful of extremely fruitful strategies. Formation of organized cells is generally facilitated by exploiting the cellular phenomena of contact guidance where many cell types preferentially align to anisotropic surfaces. Release of cells has been carried out in a number of ways with release from thin grafted films of pNIPAAm being the most widely studied. With all of this effort applied to organization and release of cells, very little progress has been made in applying these practices to higher level tissue engineering applications such as minimally invasive harvest and translocation of cells and/or micro-tissues aimed at development of complex and spatially organized, multi-layered, three-dimensional micro-tissues. This chapter reviews currently explored strategies for micro-tissue translocation and its application for the development of three-dimensional micro-tissues as well as introducing a novel approach to direct translocation of organized micro-tissues by micro-contact stamping of micro-tissues from micron-scale pNIPAAm surfaces to a target substrate.

6.1 Current Strategies for Translocation of Cultured Micro-Tissues

Release of micro-tissues can be accomplished by a few techniques, but generally results in the contraction of cells within the micro-tissue due to loss of mechanical

stability with the underlying substrate upon detachment. Traction forces generated by actin-myosin mechanics generate tensile stress within the cell through tension generated in actin filaments also known as “stress fibers”. Upon disruption of ECM/focal adhesion bonds to the surface, intracellular stress fibers relax resulting in the contraction of cell bodies [92, 199, 211, 214, 223]. This results in the formation of a micro-tissue which no longer mimics the geometry of the cultured construct. To date, no know process has been developed to restore contracted tissues into their native geometry suggesting that an unaided approach to micro-tissue release has limited utility in tissue engineering applications and an approach used in tandem with cell detachment would be attractive.

One approach towards this involves cell culture on a thick pNIPAAm film lacking any internal crosslinks. This allows for a pNIPAAm film that has the mechanical stability required to handle with forceps, making it a good surface for cell culture and translocation. After culture is complete and a suitable micro-tissue is formed, the film can be removed and placed in contact with another surface, incubated, and the pNIPAAm film can be dissolved away by a low temperature treatment. This has been shown to successfully transplant functional cardiomyocyte micro-tissues [212]. While this is an interesting approach, dissolution of the pNIPAAm film will result in long chain pNIPAAm molecules remaining in the bulk culture which raises question regarding their impact on cell health and may require a series of washing steps prior to translocation to limit potential impacts.

Another study demonstrated the culture of human fibroblasts in tandem with a poly(lactic-co-glycolic acid) mesh. The aim was to reduce cell sheet contraction by folding a grown sheet over the surface of the mesh, in a four step folding process, to

generate a thick cell sheet that was easily manipulated for transplantation in a host [224]. The folding was performed using forceps raising questions regarding the impact that direct mechanical manipulation of sensitive cell sheets may have on cell health and membrane integrity.

As cell sheet engineering, a concept introduced by Teruo Okano, is a widely studied approach for cell culture and cell release, recent studies have demonstrated approaches towards translocation of cells from the culture surface to a target surface. These approaches generally involve the use of an intermediate surface which acts to stabilize the micro-tissue during release and translocation. In one study, hydrophilically modified polyvinylidenefluoride (PVDF) membranes were used as such a support to aid in transfer of human aortic endothelial cells from grafted pNIPAAm films to a virgin tissue culture surface. PVDF membranes were then peeled away from the transferred cells leaving behind the cell sheet attached to the virgin surface [92]. One question which remains regarding this technique is the mechanical disassociation of the transfer membrane and its impact on cell membrane stability. More recent studies involving translocation of cell sheets from grafted pNIPAAm surfaces have demonstrated the use of hydrogel coated stamps as an intermediate surface for translocation of cells [98-100, 199, 225]. In one study a gelatin stamp was incubated on a cultured cell sheets for 30 minutes at low temperature (20°C) to induce cell release and transfer of myoblast to the hydrogel stamp. With the myoblast sheet still attached to the gelatin stamp, subsequent sheets are transferred to the stamp in the same fashion, yielding a gelatin stamp containing a multilayered micro-tissue. The gelatin stamp is then placed on a virgin surface such as TCPS and incubated at low temperature (20°C) for an unreported period to allow

attachment of cells to the fresh surface. Finally the gelatin stamp is removed by increasing the temperature to culture conditions (37°C) causing the gelatin to melt away and leaving behind the multilayered micro-tissue. This technique has met with promise and has been used to generate pseudo vascularized micro-tissues by combining the stamping technique with contact guidance induced cellular organization [98, 99, 199]. In one study a multilayered sheet consisting of five separately cultured and harvested sheets of skeletal myoblasts and dermal fibroblasts were combined on a gelatin stamp surface and transferred to a tissue culture dish to evaluate vertical cell migration within the three-dimensional micro-tissue [100]. These studies demonstrate the power of a stamp-based approach to generating highly complex three-dimensional micro-tissue. Although this technique seems extremely promising as a tissue engineering strategy, a few concerns can be raised. As previously discussed in Chapter 5, cell release from grafted pNIPAAm surfaces typically requires a lengthy low-temperature incubation of the cells, raising concerns about cell health and impact on cellular functions and gene expression [219-221]. In reports outlining the approach of cell release to gelatin stamps this incubation is approximately 30 minutes for each transferred cell sheet. Additionally, transfer of the micro-tissue from the gelatin stamp to a virgin surface requires an additional low-temperature incubation to induce micro-tissue attachment of approximately 20 minutes and up to 2 hours in some cases [100, 199]. This suggests that some of the cells which comprise a five layer micro-tissue would have been subjected to low temperatures (20°C) for a minimum of 170 minutes and a maximum of 270 minutes or approximately 4 ½ hours.

6.2 Cell Stamping from Micron-Scale pNIPAAm Structures

The concept of developing highly organized, three-dimensional, micro-tissues by a stamp-based technique is highly attractive but current strategies towards this are slow and require cells to be subject to hypothermic conditions for extended periods of time in order to develop multi-layered micro-tissues. To address these issues a process has been developed which has potential to form similar micro-tissues while reducing both the degree and duration cells are subjected to a hypothermic environment. A schematic overview for a micron-scale pNIPAAm based approach to micro-contact stamping of organized micro-tissues is presented in Figure 6-1. The entire process is comprised of six primary steps and has thus far been performed using NIH 3T3 mouse fibroblasts. First, sample surfaces are seeded with a high density of cells to ensure good surface coverage. Second, cells are allowed to incubate on the surface for approximately 24 hours such that cells can fully spread on the pNIPAAm structures, orient to the anisotropy, and generate sufficient ECM. The pNIPAAm surface is then placed in contact with a target surface and held in place by adding a small weight to ensure good contact. The samples are then cooled to ~28°C by adding a small amount of ice cold DPBS. This causes thermally-induced swelling of the surface generating a surface strain which results in rapid detachment of cells from the pNIPAAm structures. The swollen stamp and target surface are allowed to incubate for 3-5 minutes to give sufficient time for adsorption of ECM proteins from the micro-tissue to the target surface as well as adequate cell adhesion [(226)]. Finally, the weight is removed and the target surface is retracted containing the stamped micro-tissue.

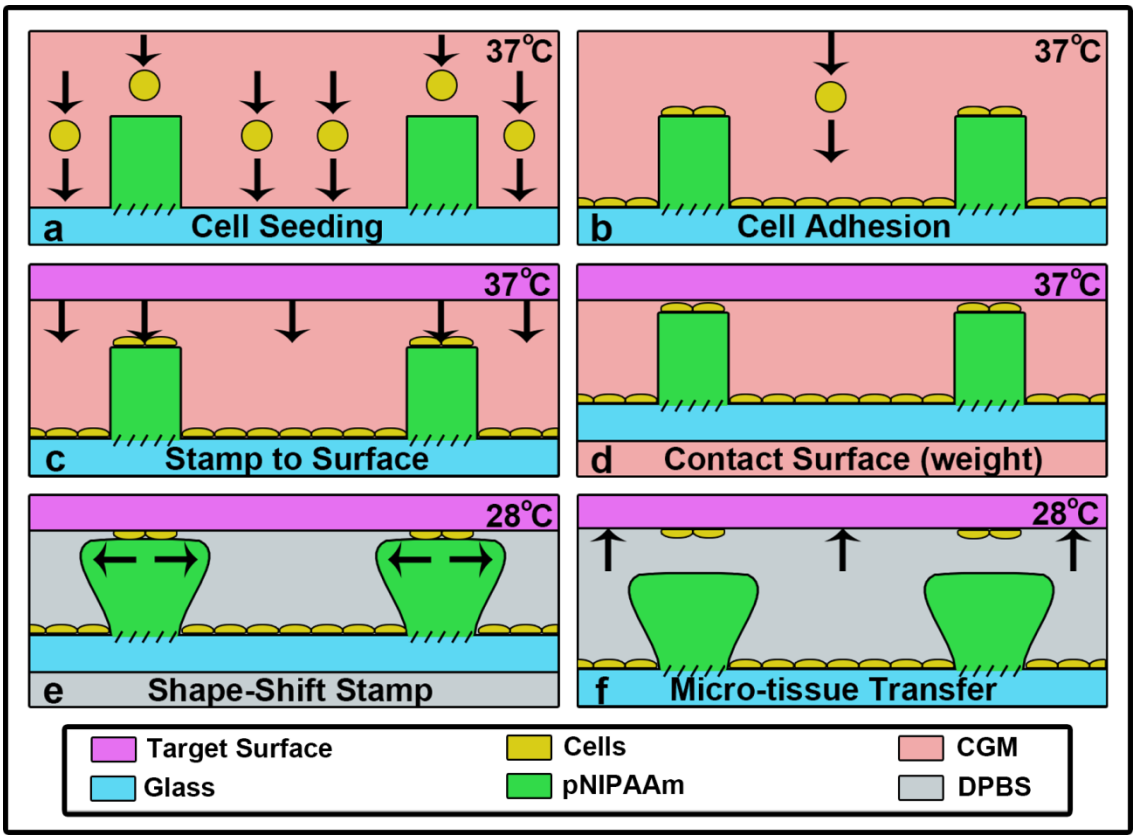

Figure 6-1: Schematic outlining the primary steps involved in micro-contact stamping of organized micro-tissues from pNIPAAm structures.

This micro-contact stamping procedure was testing using NIH 3T3 mouse fibroblasts cultured on micron-scale pNIPAAm closely spaced arrays and wide isolated structures. Stamping was attempted on two types of surface: TCPS and PDMS. Both surfaces were incubated with fibronectin prior to stamping to enhance cell adhesion to the surface. A partially transferred micro-tissue from an arrayed surface (8μm) is shown in Figure 6-2. This micro-tissue remained well attached to the TCPS surface post stamping although during the stamping process adhesion throughout the surface area of the tissue and the TCPS surface was not fully developed after 3 minutes of incubation.

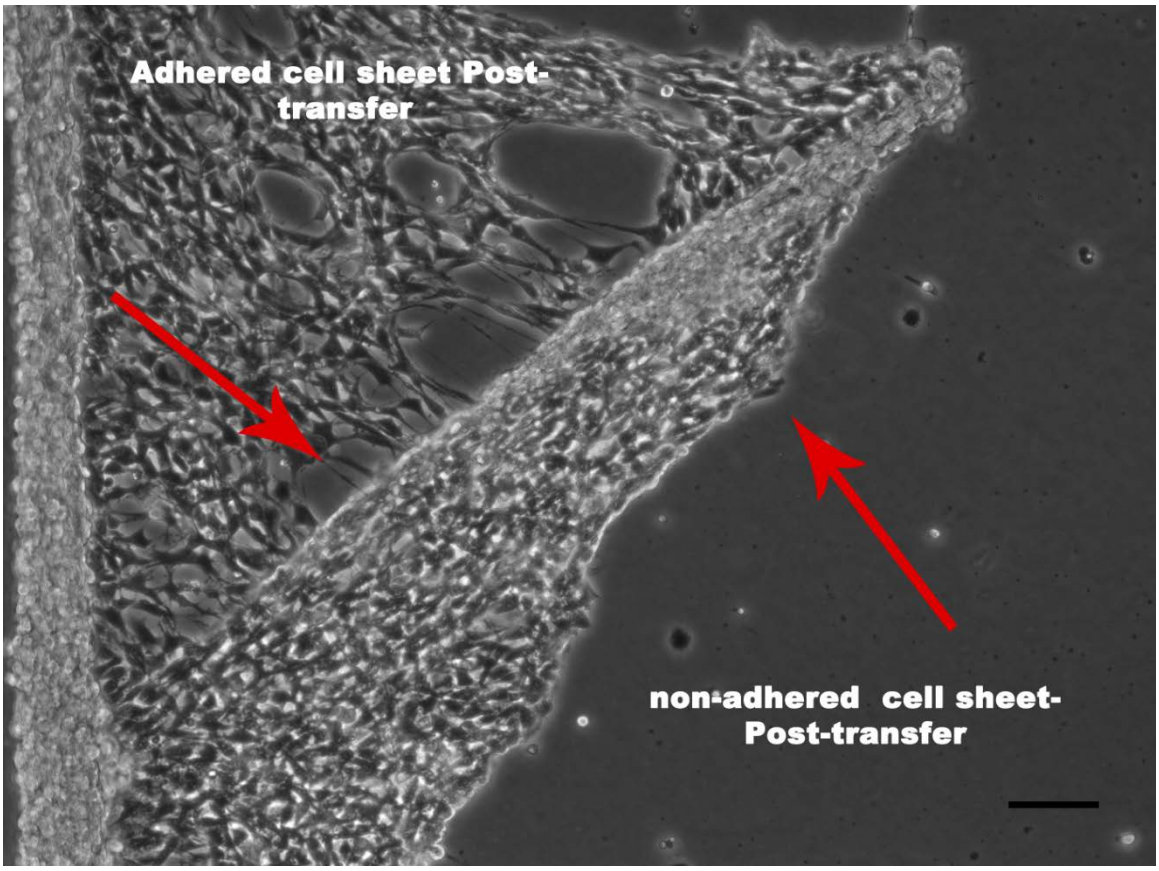

Figure 6-2: Partial transfer of an aligned sheet from a pNIPAAm arrayed surface to a fibronectin treated TCPS surface after 3 minutes of incubation. Size bar represents 100µm.

Incomplete transfer can be attributed to insufficient time for adhesion to the surface or poor conformal contact between the stamp and receiving surface. To address these two potential issues stamping was performed on a more compliant surface (PDMS) and incubation times were increased to 5 minutes before disassociation of the two surfaces. An aligned micro-tissue from an arrayed pNIPAAm surface (8µm) was stamped onto a PDMS surface after 5 minutes of incubation prior to disassociation of the two surfaces (Figure 6-3). Although transfer was still incomplete, maintenance of cell alignment and organization was significantly enhanced and non-transferred portions of

the micro-tissue were completely absent from the stamped surface suggesting that they were lost to the bulk during the stamping process.

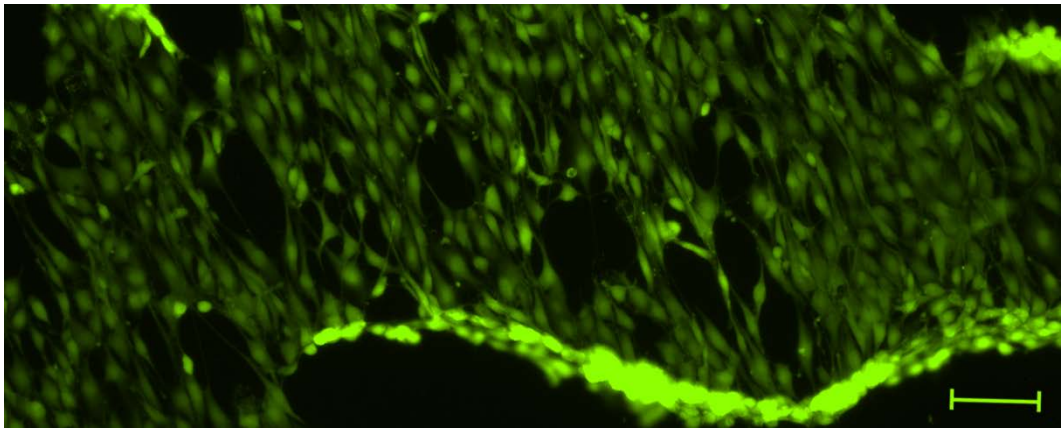

Figure 6-3: Transfer of an aligned micro-tissue sheet from an arrayed pNIPAAm surface to a fibronectin coated PDMS surface after 5 minutes of incubation. Size bar represents 100µm.

Stamping of micro-tissues developed on isolated pNIPAAm structures was also performed. Figure 6-4 displays a ribbon-like micro-tissue that was stamped from a 100µm wide pNIPAAm structure to a fibronectin treated PDMS surface after 5 minutes of incubation prior to disassociation of the two surfaces. The stamped micro-tissue was 120.8 µm at its widest point. Although the strain of this surfaces was not directly tested, it was fabricated from a chemistry which typically yields a surface strain of 0.35 – 0.45. This suggests that the micro-tissue slightly stretched perpendicular to its long axis with a strain of about 0.21 before detaching and adhering to the PDMS surface resulting in the transfer of a 120.8µm micro-tissue although the pNIPAAm surface would have expanded to approximately 135µm.

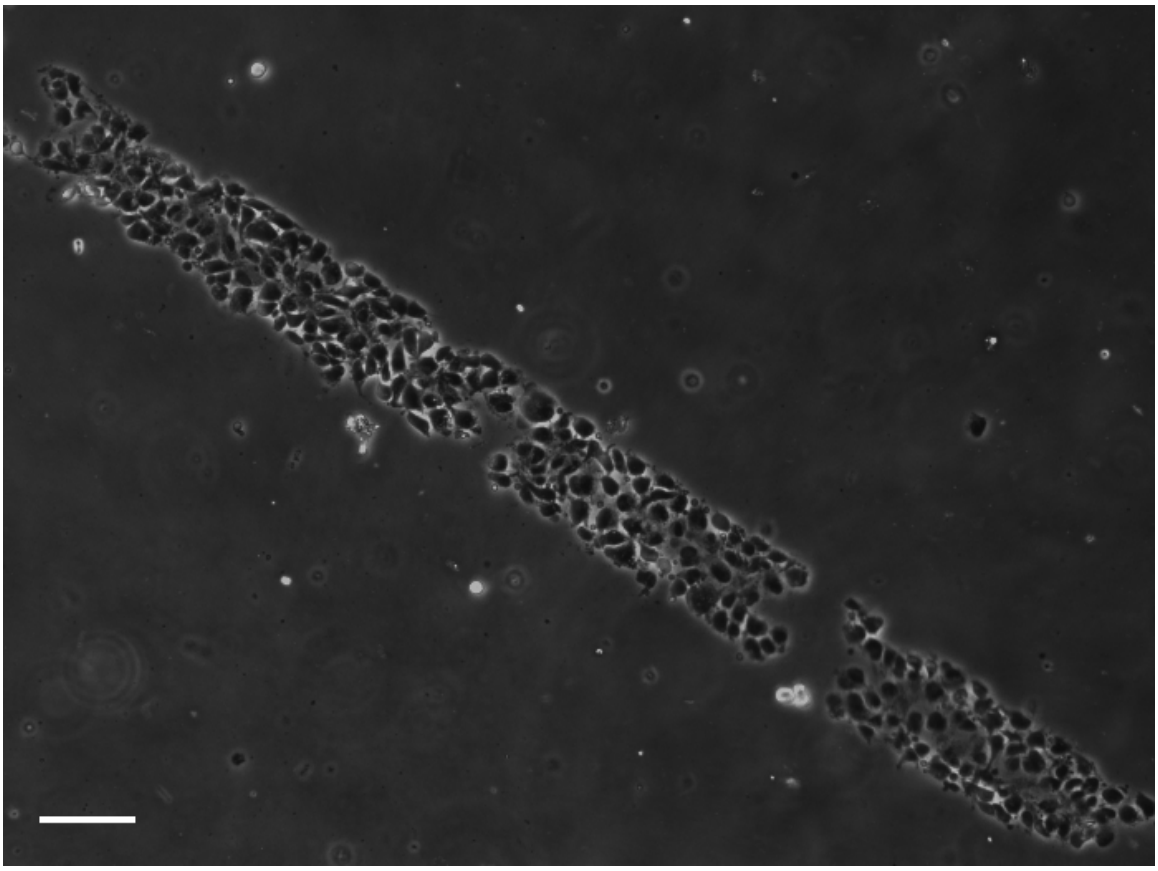

Figure 6-4: Transfer of a ribbon-like micro-tissue from a 100µm wide pNIPAAm structure by micro-contact stamping onto a PDMS surface. Size bar represents 100µm.

Transfer of the micro-tissue in Figure 6-4 appears to have affected the alignment of its constituent cells resulting in a stamped micro-tissue which retains its global organization, but has lost cellular polarization. Although it is not completely clear why this occurs, many attempts at stamping have shown similar results while others have provided transfers that conserve more of the micro-tissue structure and alignment as can be seen in Figure 6-5. Here a ribbon-like micro-tissue was transferred from a 75µm wide pNIPAAm structure. At its widest point the stamped micro-tissue had a width of 80.1µm which can be interpreted as a slight stretching of the stamped micro-tissue with a strain of approximately 0.07.

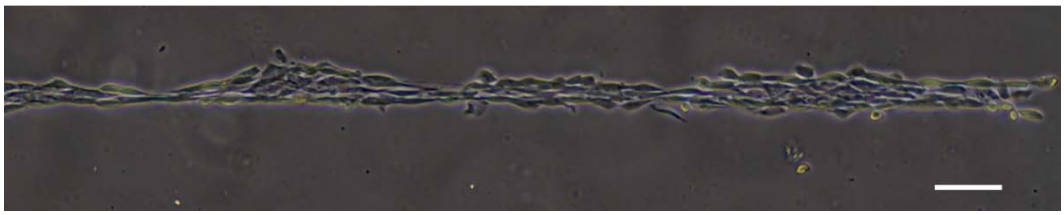

Figure 6-5: Transfer of a ribbon-like micro-tissue from an isolated pNIPAAm structure having a width of 75µm to a fibronectin treated PDMS surface by micro-contact stamping. Size bar represents 100µm.

Micro-tissue stamping from pNIPAAm structures typically results in complete removal of micro-tissues from the structures and, while optimization of the process must be further explored, can result in the transfer of micro-tissues to the receiving surface without significant transfer of surrounding cells bound to the glass surface as shown in Figure 6-6.

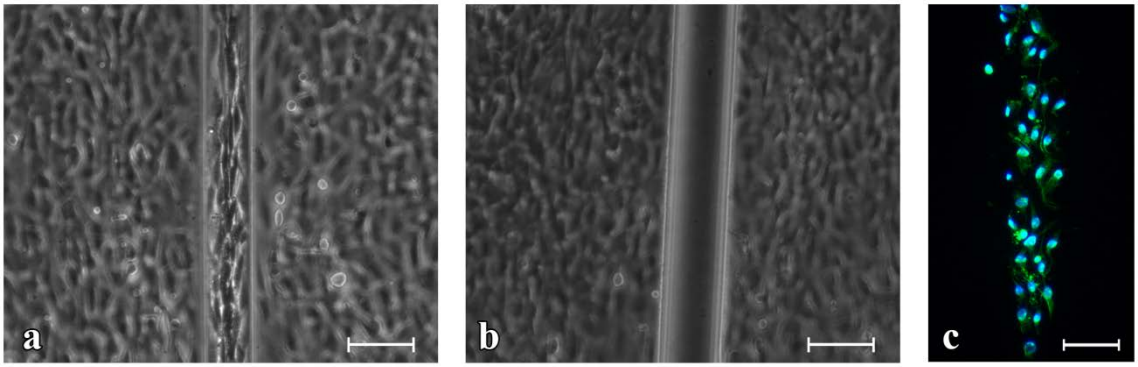

Figure 6-6: A ribbon-like micro-tissue cultured atop of a 75µm wide pNIPAAm structure (a) shown removed from the structure (b) by micro-contact stamping of the micro-tissue onto a fibronectin treated PDMS surface (c) and stained to show the cell bodies (green) and cell nuclei (blue). Size bars represent 100µm.

Micro-contact stamping of micro-tissues from narrow isolated pNIPAAm structures has been accomplished in the same way, resulting in the stamping of “fiber-like” structures on the receiving PDMS surface. A stamped “fiber-like” structure is

presented in Figure 6-7 where a fiber consisting of no more than two cells in width was transferred to a fibronectin coated PDMS surface from a 20µm wide pNIPAAm beam which undergoes bulk structural buckling as a result of thermally-induced swelling.

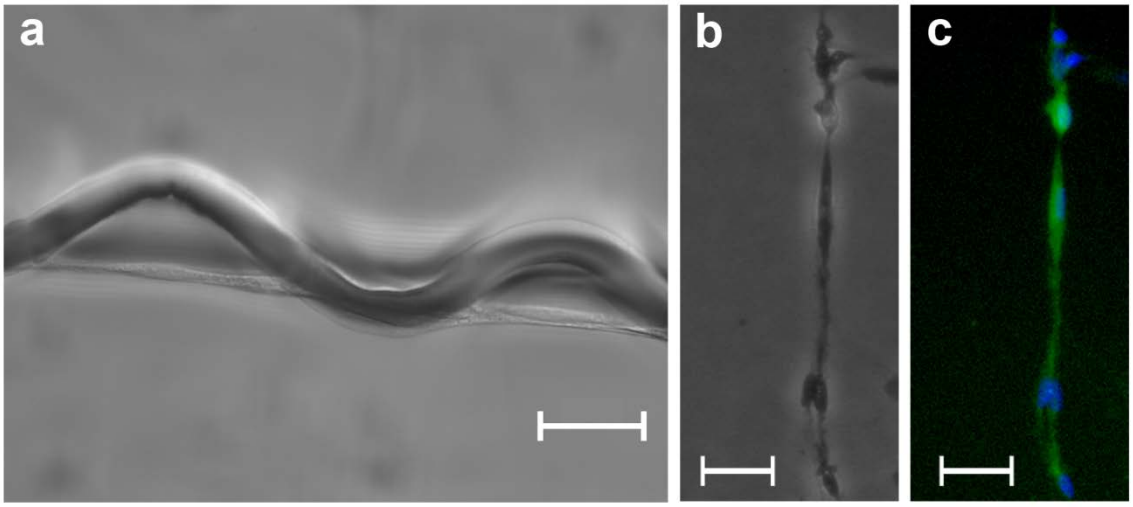

Figure 6-7: A fiber-like micro-tissue formed on a 20µm wide pNIPAAm structure (a) which has been micro-contact stamped onto a fibronectin coated PDMS surface shown in phase contrast (b) and stained (c) to show the cell bodies (green) and cell nuclei (blue). Size bar represents 50µm.

To determine the viability of stamped cells two methods were employed. First, calcein-AM staining was performed on transferred micro-tissue sheets as shown in Figure 6-3. Uptake of calcein-AM suggests cell viability by demonstrating healthy, intact cell membranes. Additionally cell health and maintenance of cell organization was tested by observing stamped micro-tissues on the receiving PDMS surface after four hours of incubation under culture conditions. Figure 6-8 shows a micro-tissue stamped from a 75µm structure directly after stamping and four hours prior to stamping. Although the micro-tissue shape and cell polarization seem to be adequately preserved directly after stamping, within four hours of stamping cell spreading and migration on the non-

patterned surface result in significant loss of these features. This demonstrates cell viability post-stamping but introduces a new challenge as micro-tissue organization is gradually lost due to cellular migration and a lack of any type of confining features or anisotropic topography.

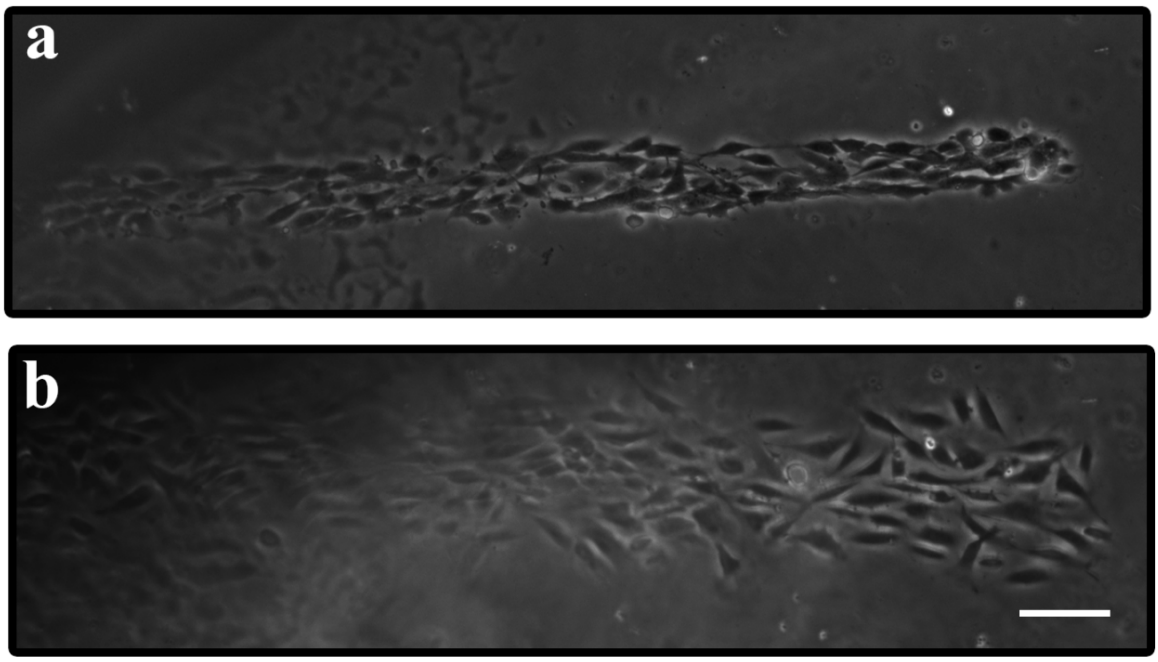

Figure 6-8: A ribbon-like micro-tissue stamped onto a fibronectin treated PDMS surface from a 75μm wide structure directly after stamping (a) and after four hours of incubation under standard culture conditions (b). Size bar represents 100μm.

Because pNIPAAm surfaces can be patterned over wide areas having various geometries, cell stamping can translocate micro-tissues with both local and global control over micro-tissue organization and geometry. Figure 6-9 shows a fibronectin coated PDMS surface after stamping an array of widely spaced “ribbon-like” micro-tissues over an area extending a few millimeters.

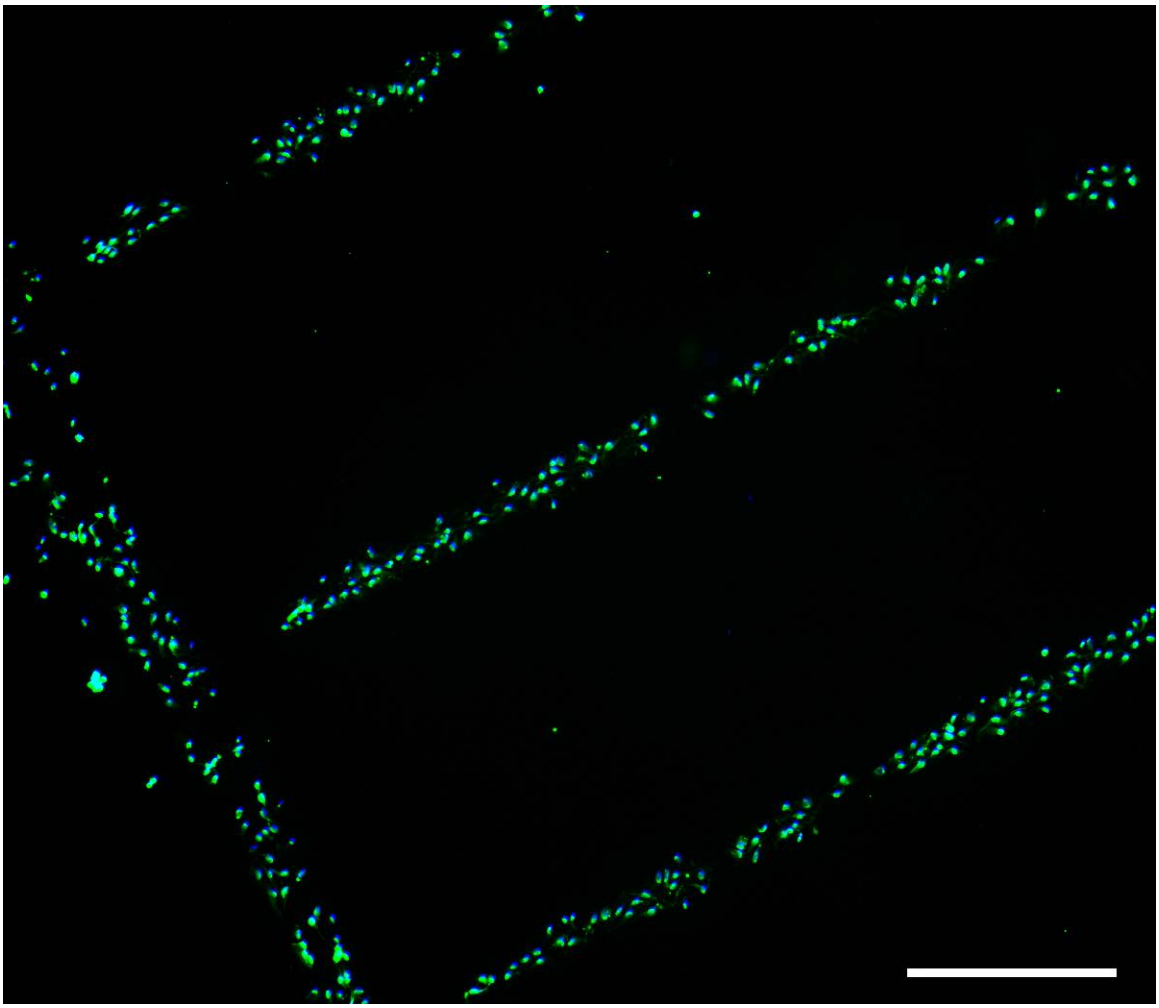

Figure 6-9: Fibroblasts stained to show the cell bodies (green) and cell nuclei (blue) after stamping onto a fibronectin coated PDMS surface. Size bar represents 500µm.

6.3 Discussion of Results

Previous studies have demonstrated that a stamping-based method for translocation of cultured tissues is an attractive strategy for micro-tissue harvest as well as the development of multi-layered micro-tissue constructs [98-100, 199]. The results of this study demonstrate the feasibility of stamping organized micro-tissues directly from the pNIPAAm structure to a receiving surface. Stamping has been demonstrated using NIH 3T3 mouse fibroblasts grown atop various geometries of pNIPAAm structures.

Organized cellular micro-tissues were transferred from the surfaces to both polystyrene and PDMS surfaces treated with fibronectin to enhance cell adhesion. Sheets of aligned cells, “ribbon-like” micro-tissue strips and “fiber-like” micro-tissue lines were successfully stamped through this process. It was observed that stamping was more favorable on a softer, more compliant PDMS surface in contrast to a TCPS surface and extended incubation times between the stamp and the surface helped with transfer and maintenance of cellular organization. Additionally, cell health was shown to be good in cells stamped by this process as staining with calcein-AM was successful and cell migration and spreading was observed hours after transfer. Although this is a promising technique for micro-tissue translocation, it is not without its challenges. Stamping of cells from pNIPAAm structures proved to be challenging and reproducibility was low with stamping success of approximately 10%. When micro-tissue stamping was achieved, pattern transfer was not complete across the entire sample. Incomplete transfer and transfer success can be attributed to a few factors such as: conformal contact between the stamp and the surface, stamping pressure, incubation time between the stamp and receiving surface, and stable approach and retraction of the two surfaces pre and post stamping.

Conformal contact is absolutely necessary for good micro-tissue transfer over a large area, especially when patterns are highly isolated such as the ones containing “ribbon-like” micro-tissues. Misalignment between the two surfaces of less than a degree can result in loss of patterned micro-tissue transfer over large areas of the sample. Previous studies which involved an intermediate transfer surface, such as a soft gelatin gel, did not report such difficulty [98-100, 199]. This could be due to the fact that transferred

cells were usually in the form of large millimeter-scale sheets. As cells in the sheet are held together by ECM and cell/cell contacts, small degrees of misalignment would not prevent transfer of the entire sheet as cells would remained attached in the micro-tissue. Also, the gelatin gels used are extremely soft providing enhanced compliance with the surface which aids in buffering any potential misalignments.

Stamping pressure can also play a critical role in micro-tissue transfer. It is important for cells to be in good contact with the surface in order to induce adhesion to the surface while too much pressure could result in damaging cell membranes. Without applying any pressure by adding weight (i.e. using only the weight of the PDMS stamp) cell stamping was primarily unsuccessful. This is most likely due to extreme lack of contact between the two surfaces. Small weights ranging from 20g to 100g were attempted to ensure good contact between the two surfaces. It was observed that transfer was optimal using smaller weights but larger weights were applied to help facilitate good conformal contact between the two surfaces and hopefully enhancing global pattern transfer. At weights exceeding 50g, micro-tissue stamping was extremely poor and in many cases delamination of the pNIPAAm structure occurred. Delamination may be caused by the additional plane of confinement induced by the additional weight applied to structure tops. This could result in an increase in internal stresses in the swelling gel, ultimately causing the gel to delaminate.

Incubation time between the pNIPAAm surface and the receiving surface is important in order to allow for adsorption of ECM proteins and formation of focal adhesions between cells which comprise the micro-tissue and the new surface. Although this time is essential for good micro-tissue transfer, it would be attractive to minimize this

time while still maintaining good transfer for reducing the impact of low temperature incubation of cells, as this could potentially result in changes in cell health and biochemical state [219-221]. Results for cells stamped with a three minute incubation showed transfer of cells but typically resulted in loss of cellular polarization in the micro-tissue. This could be due to lack of good adhesion between cells and the receiving surface resulting in retraction of the cell bodies upon loss of contact with the pNIPAAm support. Cells stamped with incubation times of five minutes or longer showed enhanced preservation of cellular polarization suggesting that this may be close to the lower limit of the contact time required to allow sufficient micro-tissue transfer in NIH 3T3 fibroblasts while maintaining cell organization.

Stamping from pNIPAAm structures was primarily performed by hand for this study which can present problems which may address incomplete transfer of micro-tissues. Placing a 1x1cm PDMS surface atop a 22x22mm sample, adding a weight, and then removing them without shearing the two surfaces is impractical. Shearing of these two surfaces during this process can result in loss of micro-tissue organization and result in the destruction of the stamped tissue. A fiber-like micro-tissue stamped from a 20µm wide isolated pNIPAAm structure is shown in Figure 6-10. From this, image cells from the original micro-tissue appear to be sheared across the surface which may be the result of poor approach or retraction of the two surfaces during stamping.

It was shown that the width of a “ribbon-like” micro-tissue transferred from a 100µm pNIPAAm structure to a receiving surface was slightly increased from 100µm to 120.8µm even though the surface would have expanded to at least 135µm based on the fabrication chemistry (Figure 6-4). The stretched micro-tissue after stamping implies that

the micro-tissue released and transferred to the surface after experiencing a strain of approximately 0.21. Additionally, in Figure 6-5 another “ribbon-like” micro-tissue is shown post transfer from a 75μm pNIPAAm structure also being stretched in width with a micro-tissue strain of approximately 0.07. Interestingly, both of the strains observed in stamped micro-tissues are either at, or below, the critical strain range presented in Chapter 5, further suggesting that micro-tissue detachment is strain driven. Also, the micro-tissue which experienced the greatest degree of strain had lost a majority of cellular polarization of its constituent cells while the micro-tissue which experienced less strain maintained its cellular polarization. Although in the context of this study it is unclear the exact reason for this, this may suggest that stabilization of the micro-tissue by adhesion to the receiving surface may play an important role before retraction of the stamp as the stamped micro-tissue which retained more of its internal cellular polarization had been incubated with the surface for a longer period.

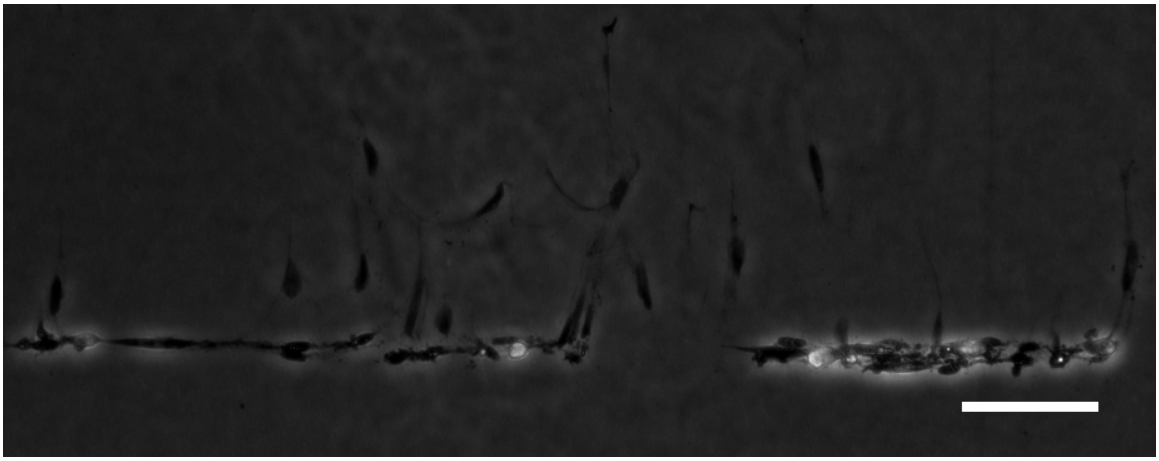

Figure 6-10: Phase contrast image of a fiber-like micro-tissue stamped onto a fibronectin coated PDMS surface showing cells disaggregated from the micro-tissue. Size bar represents 100μm.

In general, stamping directly from pNIPAAm structures to a receiving surface has potential although optimization is required. This process offers a method by which stamping of organized micro-tissues can be performed without an intermediate surface and more rapidly than existing studies have demonstrated. Overall, this helps to reduce the impact of extended exposure to low temperature environments as the temperature drop has been minimized and exposure time reduced. Also, previous attempts to develop multi-layered micro-tissues through multiple stamping events require the cells to be constantly subjected to low temperature environments until formation of the three-dimensional micro-tissue is complete. The process presented here addresses this problem as cells stamped onto a surface can be incubated for a period prior to subsequent stamping acting to reduce the impact of extended exposure to low temperatures. This cannot be performed on current gelatin-based stamping technologies as heating of the media would cause melting of the gelatin layer and loss of the intermediate layer.

6.4 Summary

Stamping organized micro-tissues directly from the culture surface to a final receiving surface has yet to be shown without the need for an intermediate transfer surface. This work demonstrates the use of responsive surfaces capable of organizing cells into ordered micro-tissues for the direct stamping of micro-tissues to a receiving surface. Although there are still some challenges which must be met, this may be a viable technique for the subsequent construction of three-dimensional micro-tissues through multiple stamping of cells in a manner which reduces the impact of lengthy low-temperature treatments and preserves cellular state and function.

Chapter 7: Summary

Development of engineered materials capable of interfacing with biological systems is essential to advancing the field of tissue engineering. This study provides insights into the mechanical nature of micron-scale structures comprised of the thermally responsive polymer pNIPAAm. Due to the responsive nature of pNIPAAm, its use has been widespread in tissue engineering with most research focused on its application as a culture surface where cell adhesion can be thermally controlled. Typically, shifts in material geometry are not attributed to the material's application as the material films are on a length-scale that is far below that of a single cell. Although application of pNIPAAm for use in tissue engineering has been studied for quite some time, this study provides a novel approach to its application in the context of cell culture and harvesting of well-organized micro-tissues by generating micron-scale structures that significantly alter their geometry in response to a thermal cue.

In order to accomplish this, the swelling behavior of surface confined pNIPAAm structures was evaluated to gain further insights into swelling-induced changes in structure geometry resulting from various degrees of swelling and initial state geometries. Boundaries between the onset of bulk buckling and differential lateral swelling/localized edge buckling were experimentally measured for systems at a length scale appropriate for tissue engineering applications. Although a linear elastic model can capture general trends in the onset and geometry of these instability modes it was found that

discrepancies between the linear theory and experimental observation increase as the degree of swelling of the material increases. As swelling increases, the data presented here gives evidence that mid-transition geometries are attained prior to the onset of the instability. It is these transitional state geometries which ultimately dictate the equilibrium structure suggesting that greater attention must be given to mid-transition swelling states in both experimental and theoretical studies. Additionally, observations reveal that multiple stable transition states can be attained during the swelling process prior to reaching the final equilibrium structure further complicating theoretical analysis of these systems.

Organization of cells *in vitro* is essential to developing useful micro-tissues capable of mimicking native tissues for use in both therapeutic and discovery-based tissue engineering applications. The results of this study have demonstrated the capacity for micron-scale pNIPAAm structures to influence the formation of highly aligned micro-tissues in various geometries including aligned micro-tissue sheets, “ribbon-like” micro-tissues, and “fiber-like” micro-tissues.

Release of micro-tissues grown atop thin pNIPAAm film surfaces has been widely studied and applied for nearly two decades. Although an attractive platform for cell growth and release, cultures must be subjected to extremely low temperatures for highly extended periods of time in order to achieve release raising questions regarding the health and physiological state of released micro-tissues. In fact, the primary accepted mechanism for release from these surfaces is fueled by changes within the cell that require an active metabolism. This study provides an alternative approach to cell release from pNIPAAm surfaces such that thermally initiated release can be rapidly invoked by

significant alteration of the surface geometry, uncoupling the release mechanism from cellular function. These results provide evidence that rapid cell release from micron-scale pNIPAAm surfaces is mechanical in nature and is a function of the expansion, or strain, of the swelling surface. It has also been shown that cell release can be rapidly performed within a few minutes if the expanding surface exceeds a critical strain of approximately 0.3. Additional data shows that the contractility of the cell also plays an important role in release from these surfaces. In fact, reduction in intercellular tension by inhibition of actin/myosin contractility prevented cell release suggesting that both the shear stress which results from the expanding surface and the tensile forces within the cell dictate release and may be specific to cell type. This provides motivation for further evaluation of the conditions required for rapid cell release in various cell types important to current tissue engineering strategies. In addition to release which is more rapid than on thin film surfaces, the temperature shifts required to induce detachment ($\Delta T \approx 9°C$) are not as severe as those required on pNIPAAm films ($\Delta T \approx 17°C$). This, coupled with a significantly reduced low-temperature incubation duration (~3min), provides a platform which can potentially reduce the biological impact of non-native environmental conditions on cell health and physiological state resulting in the harvest and transfer of cells more likely to mimic their native culture physiology.

Finally, application of this platform as a vehicle for the direct transfer of organized micro-tissues cultured on micron-scale pNIPAAm structures to an appropriate receiving surface was demonstrated. A typical drawback to the subsequent stacking of organized micro-tissues is the need for an intermediate surface. This increases the duration which cells experience suboptimal physical environments and increases the

complexity of the process. The capacity to directly transfer organized micro-tissues in a rapid fashion has been demonstrated and provides a design platform for minimally invasive production of complex, three-dimensional, organized micro-tissues for therapeutic and discovery-based tissue engineering approaches.

References Cited

1. Fujishige S, Kubota K, & Ando I (1989) Phase-Transition of Aqueous-Solutions of Poly(N-Isopropylacrylamide) and Poly(N-Isopropylmethacrylamide). *J Phys Chem-Us* 93(8):3311-3313.

2. Hirokawa Y & Tanaka T (1984) Volume Phase-Transition in a Nonionic Gel. *J Chem Phys* 81(12):6379-6380.

3. Vidyasagar A, Majewski J, & Toomey R (2008) Temperature induced volume-phase transitions in surface-tethered Poly(N-isopropylacrylamide) networks. *Macromolecules* 41(3):919-924.

4. Dai S, Ravi P, & Tam KC (2008) pH-Responsive polymers: synthesis, properties and applications. *Soft Matter* 4(3):435-449.

5. Ruan CM, Zeng KF, & Grimes CA (2003) A mass-sensitive pH sensor based on a stimuli-responsive polymer. *Anal Chim Acta* 497(1-2):123-131.

6. Gupta P, Vermani K, & Garg S (2002) Hydrogels: from controlled release to pH-responsive drug delivery. *Drug Discov Today* 7(10):569-579.

7. Huang J, Hu XB, Zhang WX, Zhang YH, & Li GT (2008) pH and ionic strength responsive photonic polymers fabricated by using colloidal crystal templating. *Colloid Polym Sci* 286(1):113-118.

8. Sugiura S, Sumaru K, Ohi K, Hiroki K, Takagi T, & Kanamori T (2007) Photoresponsive polymer gel microvalves controlled by local light irradiation. *Sensor Actuat a-Phys* 140(2):176-184.

9. Chen GF, Svec F, & Knapp DR (2008) Light-actuated high pressure-resisting microvalve for on-chip flow control based on thermo-responsive nanostructured polymer. *Lab on a Chip* 8(7):1198-1204.

10. Yashima E & Maeda K (2008) Chirality-responsive helical polymers. *Macromolecules* 41(1):3-12.

11. Ulijn RV (2006) Enzyme-responsive materials: a new class of smart biomaterials. *J Mater Chem* 16(23):2217-2225.

12. Tanaka F, Koga T, & Winnik FM (2008) Temperature-responsive polymers in mixed solvents: Competitive hydrogen bonds cause cononsolvency. *Physical Review Letters* 101(2).

13. Ekici S, Ilgin P, Yilmaz S, Aktas N, & Sahiner N (2011) Temperature and magnetic field responsive hyaluronic acid particles with tunable physical and chemical properties. *Appl Surf Sci* 257(7):2669-2676.

14. Ge J, Neofytou E, Cahill TJ, Beygui RE, & Zare RN (2012) Drug Release from Electric-Field-Responsive Nanoparticles. *ACS Nano* 6(1):227-233.

15. Black AL, Lenhardt JM, & Craig SL (2011) From molecular mechanochemistry to stress-responsive materials. *J Mater Chem* 21(6):1655-1663.

16. Crenshaw BR, Burnworth M, Khariwala D, Hiltner A, Mather PT, Simha R, & Weder C (2007) Deformation-induced color changes in mechanochromic polyethylene blends. *Macromolecules* 40(7):2400-2408.

17. Bawa P, Pillay V, Choonara YE, & du Toit LC (2009) Stimuli-responsive polymers and their applications in drug delivery. *Biomedical Materials* 4(2).

18. Agarwal AK, Dong L, Beebe DJ, & Jiang HR (2007) Autonomously-triggered microfluidic cooling using thermo-responsive hydrogels. *Lab on a Chip* 7(3):310-315.

19. Hu JM & Liu SY (2010) Responsive Polymers for Detection and Sensing Applications: Current Status and Future Developments. *Macromolecules* 43(20):8315-8330.

20. Rosso F, Marino G, Giordano A, Barbarisi M, Parmeggiani D, & Barbarisi A (2006) Smart materials as scaffolds for tissue engineering (vol 203, pg 468, 2006). *Journal of Cellular Physiology* 209(3):1054-1054.

21. Nishida K, Yamato M, Hayashida Y, Watanabe K, Yamamoto K, Adachi E, Nagai S, Kikuchi A, Maeda N, Watanabe H, Okano T, & Tano Y (2004) Corneal reconstruction with tissue-engineered cell sheets composed of autologous oral mucosal epithelium. *New Engl J Med* 351(12):1187-1196.

22. Cooperstein MA & Canavan HE (2010) Biological cell detachment from poly(N-isopropyl acrylamide) and its applications. *Langmuir* 26(11):7695-7707.

23. Da Silva RMP, Mano JF, & Reis RL (2007) Smart thermoresponsive coatings and surfaces for tissue engineering: switching cell-material boundaries. *Trends Biotechnol* 25(12):577-583.

24. Bernstein HS (2011) *Tissue engineering in regenerative medicine* (Humana Press, New York) pp xiv, 426 p.

25. Tanaka T, Sato E, Hirokawa Y, Hirotsu S, & Peetermans J (1985) Critical Kinetics of Volume Phase-Transition of Gels. *Physical Review Letters* 55(22):2455-2458.

26. Wu C & Wang XH (1998) Globule-to-coil transition of a single homopolymer chain in solution. *Physical Review Letters* 80(18):4092-4094.

27. Maeda Y, Nakamura T, & Ikeda I (2001) Changes in the hydration states of poly(N-alkylacrylamide)s during their phase transitions in water observed by FTIR spectroscopy. *Macromolecules* 34(5):1391-1399.

28. Meersman F, Wang J, Wu YQ, & Heremans K (2005) Pressure effect on the hydration properties of poly(N-isopropylacrylamide) in aqueous solution studied by FTIR spectroscopy. *Macromolecules* 38(21):8923-8928.

29. Cheng H, Shen L, & Wu C (2006) LLS and FTIR studies on the hysteresis in association and dissociation of poly(N-isopropylacrylamide) chains in water. *Macromolecules* 39(6):2325-2329.

30. Wang XH, Qiu XP, & Wu C (1998) Comparison of the coil-to-globule and the globule-to-coil transitions of a single poly(N-isopropylacrylamide) homopolymer chain in water. *Macromolecules* 31(9):2972-2976.

31. Shibayama M & Tanaka T (1993) Volume Phase-Transition and Related Phenomena of Polymer Gels. *Adv Polym Sci* 109:1-62.

32. Tanford C (1980) *The hydrophobic effect : formation of micelles and biological membranes* (Wiley, New York) 2d Ed pp ix, 233 p.

33. Vidyasagar A, Smith HL, Majewski J, & Toomey RG (2009) Continuous and discontinuous volume-phase transitions in surface-tethered, photo-crosslinked poly(N-isopropylacrylamide) networks. *Soft Matter* 5(23):4733-4738.

34. Deng YL, Xiao HN, & Pelton R (1996) Temperature-sensitive flocculants based on poly(N-isopropylacrylamide-co-diallyldimethylammonium chloride). *J Colloid Interf Sci* 179(1):188-193.

35. Li HH, O'Shea JP, & Franks GV (2009) Effect of Molecular Weight of Poly(N-isopropyl acrylamide) Temperature-Sensitive Flocculants on Dewatering. *Aiche J* 55(8):2070-2080.

36. Sakohara S, Kimura T, & Nishikawa K (2000) Flocculation mechanism of suspended particles utilizing hydrophilic/hydrophobic transition of thermosensitive polymer. *Kagaku Kogaku Ronbun* 26(5):734-737.

37. Kaholek M, Lee WK, Ahn SJ, Ma HW, Caster KC, LaMattina B, & Zauscher S (2004) Stimulus-responsive poly(N-isopropylacrylamide) brushes and nanopatterns prepared by surface-initiated polymerization. *Chem Mater* 16(19):3688-3696.

38. Balamurugan S, Mendez S, Balamurugan SS, O'Brien MJ, & Lopez GP (2003) Thermal response of poly(N-isopropylacrylamide) brushes probed by surface plasmon resonance. *Langmuir* 19(7):2545-2549.

39. Huber DL, Manginell RP, Samara MA, Kim BI, & Bunker BC (2003) Programmed adsorption and release of proteins in a microfluidic device. *Science* 301(5631):352-354.

40. Ista LK, Mendez S, & Lopez GP (2010) Attachment and detachment of bacteria on surfaces with tunable and switchable wettability. *Biofouling* 26(1):111-118.

41. Ista LK, Perez-Luna VH, & Lopez GP (1999) Surface-grafted, environmentally sensitive polymers for biofilm release. *Appl Environ Microb* 65(4):1603-1609.

42. Cunliffe D, Smart CA, Tsibouklis J, Young S, Alexander C, & Vulfson EN (2000) Bacterial adsorption to thermoresponsive polymer surfaces. *Biotechnol Lett* 22(2):141-145.

43. Okano T, Yamada N, Okuhara M, Sakai H, & Sakurai Y (1995) Mechanism of Cell Detachment from Temperature-Modulated, Hydrophilic-Hydrophobic Polymer Surfaces. *Biomaterials* 16(4):297-303.

44. Okano T, Yamada N, Sakai H, & Sakurai Y (1993) A Novel Recovery-System for Cultured-Cells Using Plasma-Treated Polystyrene Dishes Grafted with Poly(N-Isopropylacrylamide). *J Biomed Mater Res* 27(10):1243-1251.

45. Yamato M & Okano T (2004) Cell sheet engineering. *Mater Today* 7(5):42-47.

46. Yamato M, Okuhara M, Karikusa F, Kikuchi A, Sakurai Y, & Okano T (1999) Signal transduction and cytoskeletal reorganization are required for cell detachment from cell culture surfaces grafted with a temperature-responsive polymer. *J Biomed Mater Res* 44(1):44-52.

47. Yang J, Yamato M, Shimizu T, Sekine H, Ohashi K, Kanzaki M, Ohki T, Nishida K, & Okano T (2007) Reconstruction of functional tissues with cell sheet engineering. *Biomaterials* 28(34):5033-5043.

48. Yang J, Yamato M, Kohno C, Nishimoto A, Sekine H, Fukai F, & Okano T (2005) Cell sheet engineering: Recreating tissues without biodegradable scaffolds. *Biomaterials* 26(33):6415-6422.

49. DuPont SJ, Cates RS, Stroot PG, & Toomey R (2010) Swelling-induced instabilities in microscale, surface-confined poly(N-isopropylacryamide) hydrogels. *Soft Matter* 6(16):3876-3882.

50. Dušek K (1993) *Responsive gels : volume transitions* (Springer-Verlag, Berlin ; New York).

51. Flory PJ (1953) *Principles of polymer chemistry* (Cornell University Press, Ithaca,) p 672 p.

52. Flory PJ & Tatara YI (1975) Elastic Free-Energy and Elastic Equation of State - Elongation and Swelling of Polydimethylsiloxane Networks. *J Polym Sci Pol Phys* 13(4):683-702.

53. Matzelle TR, Geuskens G, & Kruse N (2003) Elastic properties of poly(N-isopropylacrylamide) and poly(acrylamide) hydrogels studied by scanning force microscopy. *Macromolecules* 36(8):2926-2931.

54. Hashmi SM & Dufresne ER (2009) Mechanical properties of individual microgel particles through the deswelling transition. *Soft Matter* 5(19):3682-3688.

55. Qiu Y & Park K (2012) Environment-sensitive hydrogels for drug delivery. *Adv Drug Deliv Rev*.

56. Soppimath KS, Aminabhavi TM, Dave AM, Kumbar SG, & Rudzinski WE (2002) Stimulus-responsive "smart" hydrogels as novel drug delivery systems. *Drug Dev Ind Pharm* 28(8):957-974.

57. Yu C, Mutlu S, Selvaganapathy P, Mastrangelo CH, Svec F, & Frechett JMJ (2003) Flow control valves for analytical microfluidic chips without mechanical parts based on thermally responsive monolithic polymers. *Analytical Chemistry* 75(8):1958-1961.

58. Li ZM, He QH, Ma D, & Chen HW (2010) On-chip integrated multi-thermo-actuated microvalves of poly(N-isopropylacrylamide) for microflow injection analysis. *Anal Chim Acta* 665(2):107-112.

59. Breid D & Crosby AJ (2011) Effect of stress state on wrinkle morphology. *Soft Matter* 7(9):4490-4496.

60. Chan EP & Crosby AJ (2006) Fabricating microlens arrays by surface wrinkling. *Adv Mater* 18(24):3238-+.

61. Chan EP & Crosby AJ (2006) Spontaneous formation of stable aligned wrinkling patterns. *Soft Matter* 2(4):324-328.

62. Chan EP, Smith EJ, Hayward RC, & Crosby AJ (2008) Surface wrinkles for smart adhesion. *Adv Mater* 20(4):711-+.

63. Ortiz O, Vidyasagar A, Wang J, & Toomey R (2010) Surface instabilities in ultrathin, cross-linked poly(N-isopropylacrylamide) coatings. *Langmuir* 26(22):17489-17494.

64. Cendula P, Kiravittaya S, Mei YF, Deneke C, & Schmidt OG (2009) Bending and wrinkling as competing relaxation pathways for strained free-hanging films. *Phys Rev B* 79(8).

65. Dervaux J, Couder Y, Guedeau-Boudeville MA, & Ben Amar M (2011) Shape transition in artificial tumors: from smooth buckles to singular creases. *Phys Rev Lett* 107(1):018103.

66. Mora T & Boudaoud A (2006) Buckling of swelling gels. *Eur Phys J E* 20(2):119-124.

67. Sultan E & Boudaoud A (2008) The buckling of a swollen thin gel layer bound to a compliant substrate. *J Appl Mech-T Asme* 75(5).

68. Tanaka T, Sun ST, Hirokawa Y, Katayama S, Kucera J, Hirose Y, & Amiya T (1987) Mechanical Instability of Gels at the Phase-Transition. *Nature* 325(6107):796-798.

69. Tirumala VR, Stafford CM, Ocola LE, Douglas JF, & Mahadevan L (2012) Geometric Control of Rippling in Supported Polymer Nanolines. *Nano Lett* 12(3):1516-1521.

70. Castellanos A, DuPont SJ, Heim AJ, Matthews G, Stroot PG, Moreno W, & Toomey RG (2007) Size-exclusion "capture and release" separations using surface-patterned poly(N-isopropylacrylamide) hydrogels. *Langmuir* 23(11):6391-6395.

71. Kang MK & Huang R (2011) Swelling-Induced Instability of Substrate-Attached Hydrogel Lines. *Int J Appl Mech* 3(2):219-233.

72. Liang HY & Mahadevan L (2009) The shape of a long leaf. *P Natl Acad Sci USA* 106(52):22049-22054.

73. Zhang JP, Zhao XH, Suo ZG, & Jiang HQ (2009) A finite element method for transient analysis of concurrent large deformation and mass transport in gels. *J Appl Phys* 105(9).

74. Hong W, Zhao XH, Zhou JX, & Suo ZG (2008) A theory of coupled diffusion and large deformation in polymeric gels. *J Mech Phys Solids* 56(5):1779-1793.

75. Kang MK & Huang R (2010) Swell-induced surface instability of confined hydrogel layers on substrates. *J Mech Phys Solids* 58(10):1582-1598.

76. Yoon JW, Cai SQ, Suo ZG, & Hayward RC (2010) Poroelastic swelling kinetics of thin hydrogel layers: comparison of theory and experiment. *Soft Matter* 6(23):6004-6012.

77. Biot MA (1941) General theory of three-dimensional consolidation. *J Appl Phys* 12(2):155-164.

78. Dorans K (2009) A stem cell ban is lifted, but some states see a heavy backlash. *Nat Med* 15(4):347-347.

79. Herman AR (2002) The history of skin grafts. *J Drugs Dermatol* 1(3):298-301.

80. Davis JS (1941) Address of the President: The Story of Plastic Surgery. *Ann Surg* 113(5):641-656.

81. Freshwater MF & Krizek TJ (1978) George David Pollock and the development of skin grafting. *Ann Plast Surg* 1(1):96-102.

82. Gibson T & Medawar PB (1943) The fate of skin homografts in man. *J Anat* 77(Pt 4):299-310 294.

83. Eaglstein WH & Falanga V (1998) Tissue engineering for skin: an update. *J Am Acad Dermatol* 39(6):1007-1010.

84. Nerem RM (1992) Tissue engineering in the USA. *Med Biol Eng Comput* 30(4):CE8-12.

85. Drury JL & Mooney DJ (2003) Hydrogels for tissue engineering: scaffold design variables and applications. *Biomaterials* 24(24):4337-4351.

86. Liu XH, Holzwarth JM, & Ma PX (2012) Functionalized Synthetic Biodegradable Polymer Scaffolds for Tissue Engineering. *Macromol Biosci* 12(7):911-919.

87. Bramfeldt H, Sabra G, Centis V, & Vermette P (2010) Scaffold Vascularization: A Challenge for Three-Dimensional Tissue Engineering. *Curr Med Chem* 17(33):3944-3967.

88. Chung CA, Yang CW, & Chen CW (2006) Analysis of cell growth and diffusion in a scaffold for cartilage tissue engineering. *Biotechnol Bioeng* 94(6):1138-1146.

89. Drury JL & Mooney DJ (2003) Hydrogels for tissue engineering: scaffold design variables and applications. *Biomaterials* 24(24):4337-4351.

90. Kikuchi A, Okuhara M, Karikusa F, Sakurai Y, & Okano T (1998) Two-dimensional manipulation of confluently cultured vascular endothelial cells using temperature-responsive poly(N-isopropylacrylamide)-grafted surfaces. *J Biomat Sci-Polym E* 9(12):1331-1348.

91. Kushida A, Yamato M, Konno C, Kikuchi A, Sakurai Y, & Okano T (1999) Decrease in culture temperature releases monolayer endothelial cell sheets together with deposited fibronectin matrix from temperature-responsive culture surfaces. *J Biomed Mater Res* 45(4):355-362.

92. Hirose M, Kwon OH, Yamato M, Kikuchi A, & Okano T (2000) Creation of designed shape cell sheets that are noninvasively harvested and moved onto another surface. *Biomacromolecules* 1(3):377-381.

93. Kwon OH, Kikuchi A, Yamato M, Sakurai Y, & Okano T (2000) Rapid cell sheet detachment from poly(N-isopropylacrylamide)-grafted porous cell culture membranes. *J Biomed Mater Res* 50(1):82-89.

94. Shimizu T, Yamato M, Kikuchi A, & Okano T (2003) Cell sheet engineering for myocardial tissue reconstruction. *Biomaterials* 24(13):2309-2316.

95. Akiyama Y, Kikuchi A, Yamato M, & Okano T (2004) Ultrathin poly(N-isopropylacrylamide) grafted layer on polystyrene surfaces for cell adhesion/detachment control. *Langmuir* 20(13):5506-5511.

96. Masuda S, Shimizu T, Yamato M, & Okano T (2008) Cell sheet engineering for heart tissue repair. *Adv Drug Deliver Rev* 60(2):277-285.

97. Elloumi-Hannachi I, Yamato M, & Okano T (2010) Cell sheet engineering: a unique nanotechnology for scaffold-free tissue reconstruction with clinical applications in regenerative medicine. *J Intern Med* 267(1):54-70.

98. Sasagawa T, Shimizu T, Sekiya S, Haraguchi Y, Yamato M, Sawa Y, & Okano T (2010) Design of prevascularized three-dimensional cell-dense tissues using a cell sheet stacking manipulation technology. *Biomaterials* 31(7):1646-1654.

99. Williams C, Xie AW, Yamato M, Okano T, & Wong JY (2011) Stacking of aligned cell sheets for layer-by-layer control of complex tissue structure. *Biomaterials* 32(24):5625-5632.

100. Kino-Oka M, Ngo TX, Nagamori E, Takezawa Y, Miyake Y, Sawa Y, Saito A, Shimizu T, Okano T, & Taya M (2012) Evaluation of vertical cell fluidity in a multilayered sheet of skeletal myoblasts. *Journal of Bioscience and Bioengineering* 113(1):128-131.

101. Bhadriraju K & Chen CS (2002) Engineering cellular microenvironments to cell-based drug testing improve. *Drug Discov Today* 7(11):612-620.

102. Griffith LG & Swartz MA (2006) Capturing complex 3D tissue physiology in vitro. *Nat Rev Mol Cell Bio* 7(3):211-224.

103. Sundstrom L, Biggs T, Laskowski A, & Stoppini L (2012) OrganDots - an organotypic 3D tissue culture platform for drug development. *Expert Opin Drug Dis* 7(6):525-534.

104. Mehta G, Hsiao AY, Ingram M, Luker GD, & Takayama S (Opportunities and challenges for use of tumor spheroids as models to test drug delivery and efficacy. *J Control Release* (0).

105. Brzoska JB, Benazouz I, & Rondelez F (1994) Silanization of Solid Substrates - a Step toward Reproducibility. *Langmuir* 10(11):4367-4373.

106. Kim E, Xia YN, & Whitesides GM (1995) Polymer Microstructures Formed by Molding in Capillaries. *Nature* 376(6541):581-584.

107. Kim E, Xia YN, & Whitesides GM (1996) Micromolding in capillaries: Applications in materials science. *J Am Chem Soc* 118(24):5722-5731.

108. Xia YN & Whitesides GM (1998) Soft lithography. *Annu Rev Mater Sci* 28:153-184.

109. Liu XM, Wang LS, Wang L, Huang JC, & He CB (2004) The effect of salt and pH on the phase-transition behaviors of temperature-sensitive copolymers based on N-isopropylacrylamide. *Biomaterials* 25(25):5659-5666.

110. Yagi Y, Inomata H, & Saito S (1992) Solubility Parameter of an N-Isopropylacrylamide Gel. *Macromolecules* 25(11):2997-2998.

111. Ishizaki T, Uehata M, Tamechika I, Keel J, Nonomura K, Maekawa M, & Narumiya S (2000) Pharmacological properties of Y-27632, a specific inhibitor of Rho-associated kinases. *Mol Pharmacol* 57(5):976-983.

112. Palmieri F & Klingenberg M (1967) Inhibition of respiration under the control of azide uptake by mitochondria. *Eur J Biochem* 1(4):439-446.

113. Dumbauld DW, Shin H, Gallant ND, Michael KE, Radhakrishna H, & Garcia AJ (2010) Contractility Modulates Cell Adhesion Strengthening Through Focal Adhesion Kinase and Assembly of Vinculin-Containing Focal Adhesions. *Journal of Cellular Physiology* 223(3):746-756.

114. Doukoglou TD & Hunter IW (1995) Volumetric image distortion due to refractive index mismatch in 3D confocal scanning laser microscopy. *Engineering in Medicine and Biology Society, 1995., IEEE 17th Annual Conference*, pp 505-506 vol.501.

115. Clarys JP, Martin AD, & Drinkwater DT (1984) Gross tissue weights in the human body by cadaver dissection. *Hum Biol* 56(3):459-473.

116. Ingber DE (2005) Mechanical control of tissue growth: Function follows form. *P Natl Acad Sci USA* 102(33):11571-11572.

117. Armstrong E, Schleicher A, Omran H, Curtis M, & Zilles K (1995) The Ontogeny of Human Gyrification. *Cereb Cortex* 5(1):56-63.

118. Zasadzinski JA, Ding J, Warriner HE, Bringezu F, & Waring AJ (2001) The physics and physiology of lung surfactants. *Curr Opin Colloid In* 6(5-6):506-513.

119. Hamilton DJ, Pilliar RM, Waldman S, & Kandel RA (2010) Effect of circumferential constraint on nucleus pulposus tissue in vitro. *Spine J* 10(2):174-183.

120. Chan A, Orme RP, Fricker RA, & Roach P (2012) Remote and local control of stimuli responsive materials for therapeutic applications. *Adv Drug Deliv Rev*.

121. Roy D, Cambre JN, & Sumerlin BS (2010) Future perspectives and recent advances in stimuli-responsive materials. *Prog Polym Sci* 35(1-2):278-301.

122. Li Y & Tanaka T (1990) Kinetics of Swelling and Shrinking of Gels. *J Chem Phys* 92(2):1365-1371.

123. Flory PJ & Rehner J (1943) Statistical mechanics of cross-linked polymer networks II Swelling. *J Chem Phys* 11(11):521-526.

124. Flory PJ & Rehner J (1943) Statistical mechanics of cross-linked polymer networks I Rubberlike elasticity. *J Chem Phys* 11(11):512-520.

125. Eddington DT & Beebe DJ (2004) Flow control with hydrogels. *Adv Drug Deliver Rev* 56(2):199-210.

126. Dervaux J & Ben Amar M (2012) Mechanical Instabilities of Gels. *Annu Rev Conden Ma P* 3:311-332.

127. Tirumala VR, Divan R, Ocola LE, & Mancini DC (2005) Direct-write e-beam patterning of stimuli-responsive hydrogel nanostructures. *J Vac Sci Technol B* 23(6):3124-3128.

128. Caykara T, Kiper S, & Demirel G (2006) Thermosensitive poly(N-isopropylacrylamide-co-acrylamide) hydrogels: Synthesis, swelling and interaction with ionic surfactants. *Eur Polym J* 42(2):348-355.

129. Kabra BG, Gehrke SH, Hwang ST, & Ritschel WA (1991) Modification of the Dynamic Swelling Behavior of Poly(2-Hydroxyethyl Methacrylate) in Water. *J Appl Polym Sci* 42(9):2409-2416.

130. Park TG & Hoffman AS (1993) Sodium Chloride-Induced Phase-Transition in Nonionic Poly(N-Isopropylacrylamide) Gel. *Macromolecules* 26(19):5045-5048.

131. Patra L, Vidyasagar A, & Toomey R (2011) The effect of the Hofmeister series on the deswelling isotherms of poly(N-isopropylacrylamide) and poly(N,N-diethylacrylamide). *Soft Matter* 7(13):6061-6067.

132. Zhang YJ, Furyk S, Bergbreiter DE, & Cremer PS (2005) Specific ion effects on the water solubility of macromolecules: PNIPAM and the Hofmeister series. *J Am Chem Soc* 127(41):14505-14510.

133. Inomata H, Goto S, Otake K, & Saito S (1992) Effect of Additives on Phase-Transition of N-Isopropylacrylamide Gels. *Langmuir* 8(2):687-690.

134. Panayiotou M, Garret-Flaudy F, & Freitag R (2004) Co-nonsolvency effects in the thermoprecipitation of oligomeric polyacrylamides from hydro-organic solutions. *Polymer* 45(9):3055-3061.

135. Takigawa T, Yamawaki T, Takahashi K, & Masuda T (1997) Change in Young's modulus of poly(N-isopropylacrylamide) gels by volume phase transition. *Polym Gels Netw* 5(6):585-589.

136. Sierra-Martin B, Laporte Y, South AB, Lyon LA, & Fernandez-Nieves A (2011) Bulk modulus of poly(N-isopropylacrylamide) microgels through the swelling transition. *Phys Rev E* 84(1).

137. Curtis ASG, Forrester JV, Mcinnes C, & Lawrie F (1983) Adhesion of Cells to Polystyrene Surfaces. *Journal of Cell Biology* 97(5):1500-1506.

138. Hassall CJ, Allen TG, Pittam BS, & Burnstock G (1989) The use of cell and tissue culture techniques in the study of regulatory peptides. *Experientia Suppl* 56:113-136.

139. Canavan HE, Cheng XH, Graham DJ, Ratner BD, & Castner DG (2005) Cell sheet detachment affects the extracellular matrix: A surface science study comparing thermal liftoff, enzymatic, and mechanical methods. *J Biomed Mater Res A* 75A(1):1-13.

140. Isenberg BC & Wong JY (2006) Building structure into engineered tissues. *Mater Today* 9(12):54-60.

141. Sell SA, McClure MJ, Garg K, Wolfe PS, & Bowlin GL (2009) Electrospinning of collagen/biopolymers for regenerative medicine and cardiovascular tissue engineering. *Adv Drug Deliver Rev* 61(12):1007-1019.

142. Iatridis JC (2009) Tissue Engineering Function Follows Form. *Nat Mater* 8(12):923-924.

143. Scott W, Stevens J, & Binder-Macleod SA (2001) Human skeletal muscle fiber type classifications. *Phys Ther* 81(11):1810-1816.

144. Eschenhagen T, Eder A, Vollert I, & Hansen A (2012) Physiological aspects of cardiac tissue engineering. *Am J Physiol-Heart C* 303(2):H133-H143.

145. Liau B, Christoforou N, Leong KW, & Bursac N (2011) Pluripotent stem cell-derived cardiac tissue patch with advanced structure and function. *Biomaterials* 32(35):9180-9187.

146. Wojciakstothard B, Madeja Z, Korohoda W, Curtis A, & Wilkinson C (1995) Activation of Macrophage-Like Cells by Multiple Grooved Substrata - Topographical Control of Cell Behavior. *Cell Biology International* 19(6):485-490.

147. Clark P, Connolly P, Curtis ASG, Dow JAT, & Wilkinson CDW (1987) Topographical Control of Cell Behavior .1. Simple Step Cues. *Development* 99(3):439-448.

148. Clark P, Connolly P, Curtis ASG, Dow JAT, & Wilkinson CDW (1990) Topographical Control of Cell Behavior .2. Multiple Grooved Substrata. *Development* 108(4):635-644.

149. Curtis A & Wilkinson C (1997) Topographical control of cells. *Biomaterials* 18(24):1573-1583.

150. Clark P, Connolly P, Curtis ASG, Dow JAT, & Wilkinson CDW (1991) Cell Guidance by Ultrafine Topography Invitro. *Journal of Cell Science* 99:73-77.

151. Kurpinski K, Chu J, Hashi C, & Li S (2006) Anisotropic mechanosensing by mesenchymal stem cells. *P Natl Acad Sci USA* 103(44):16095-16100.

152. Gopalan SM, Flaim C, Bhatia SN, Hoshijima M, Knoell R, Chien KR, Omens JH, & McCulloch AD (2003) Anisotropic stretch-induced hypertrophy in neonatal ventricular myocytes micropatterned on deformable elastomers. *Biotechnol Bioeng* 81(5):578-587.

153. Healy KE, Lom B, & Hockberger PE (1994) Spatial-Distribution of Mammalian-Cells Dictated by Material Surface-Chemistry. *Biotechnol Bioeng* 43(8):792-800.

154. Chen CS, Mrksich M, Huang S, Whitesides GM, & Ingber DE (1998) Micropatterned surfaces for control of cell shape, position, and function. *Biotechnol Progr* 14(3):356-363.

155. Williams C, Tsuda Y, Isenberg BC, Yamato M, Shimizu T, Okano T, & Wong JY (2009) Aligned Cell Sheets Grown on Thermo-Responsive Substrates with Microcontact Printed Protein Patterns. *Adv Mater* 21(21):2161-+.

156. Vacanti JP, Morse MA, Saltzman WM, Domb AJ, Perezatayde A, & Langer R (1988) Selective Cell Transplantation Using Bioabsorbable Artificial Polymers as Matrices. *J Pediatr Surg* 23(1):3-9.

157. Griffith LG (2000) Polymeric biomaterials. *Acta Mater* 48(1):263-277.

158. Sachlos E & Czernuszka JT (2003) Making tissue engineering scaffolds work. Review: the application of solid freeform fabrication technology to the production of tissue engineering scaffolds. *Eur Cell Mater* 5:29-39; discussion 39-40.

159. Ma PX (2008) Biomimetic materials for tissue engineering. *Adv Drug Deliv Rev* 60(2):184-198.

160. Cukierman E, Pankov R, Stevens DR, & Yamada KM (2001) Taking cell-matrix adhesions to the third dimension. *Science* 294(5547):1708-1712.

161. Hutmacher DW (2000) Scaffolds in tissue engineering bone and cartilage. *Biomaterials* 21(24):2529-2543.

162. Lee SH & Shin H (2007) Matrices and scaffolds for delivery of bioactive molecules in bone and cartilage tissue engineering. *Adv Drug Deliver Rev* 59(4-5):339-359.

163. Prabhakaran MP, Venugopal J, Chan CK, & Ramakrishna S (2008) Surface modified electrospun nanofibrous scaffolds for nerve tissue engineering. *Nanotechnology* 19(45).

164. Ghasemi-Mobarakeh L, Prabhakaran MP, Morshed M, Nasr-Esfahani MH, Baharvand H, Kiani S, Al-Deyab S, & Ramakrishna S (2011) Application of conductive polymers, scaffolds and electrical stimulation for nerve tissue engineering. *J Tissue Eng Regen M* 5(4):E17-E35.

165. Iwasa J, Engebretsen L, Shima Y, & Ochi M (2009) Clinical application of scaffolds for cartilage tissue engineering. *Knee Surg Sport Tr A* 17(6):561-577.

166. Naito Y, Shinoka T, Duncan D, Hibino N, Solomon D, Cleary M, Rathore A, Fein C, Church S, & Breuer C (2011) Vascular tissue engineering: Towards the next generation vascular grafts. *Adv Drug Deliver Rev* 63(4-5):312-323.

167. Cleary MA, Geiger E, Grady C, Best C, Naito Y, & Breuer C (2012) Vascular tissue engineering: the next generation. *Trends Mol Med* 18(7):394-404.

168. Rouwkema J, Koopman BFJM, van Blitterswijk CA, Dhert WJA, & Malda J (2010) Supply of Nutrients to Cells in Engineered Tissues. *Biotechnol Genet Eng* 26:163-177.

169. Langer R (2009) Perspectives and Challenges in Tissue Engineering and Regenerative Medicine. *Adv Mater* 21(32-33):3235-3236.

170. Schaner PJ, Martin ND, Tulenko TN, Shapiro IM, Tarola NA, Leichter RF, Carabasi RA, & DiMuzio PJ (2004) Decellularized vein as a potential scaffold for vascular tissue engineering. *J Vasc Surg* 40(1):146-153.

171. Ott HC, Matthiesen TS, Goh SK, Black LD, Kren SM, Netoff TI, & Taylor DA (2008) Perfusion-decellularized matrix: using nature's platform to engineer a bioartificial heart. *Nat Med* 14(2):213-221.

172. Bao J, Shi YJ, Sun HQ, Yin XL, Yang RN, Li L, Chen X, & Bu H (2011) Construction of a Portal Implantable Functional Tissue-Engineered Liver Using Perfusion-Decellularized Matrix and Hepatocytes in Rats. *Cell Transplantation* 20(5):753-766.

173. Gilbert TW, Sellaro TL, & Badylak SF (2006) Decellularization of tissues and organs. *Biomaterials* 27(19):3675-3683.

174. Petersen TH, Calle EA, Zhao LP, Lee EJ, Gui LQ, Raredon MB, Gavrilov K, Yi T, Zhuang ZW, Breuer C, Herzog E, & Niklason LE (2010) Tissue-Engineered Lungs for in Vivo Implantation. *Science* 329(5991):538-541.

175. Price AP, England KA, Matson AM, Blazar BR, & Panoskaltsis-Mortari A (2010) Development of a Decellularized Lung Bioreactor System for Bioengineering the Lung: The Matrix Reloaded. *Tissue Eng Pt A* 16(8):2581-2591.

176. Uygun BE, Soto-Gutierrez A, Yagi H, Izamis ML, Guzzardi MA, Shulman C, Milwid J, Kobayashi N, Tilles A, Berthiaume F, Hertl M, Nahmias Y, Yarmush ML, & Uygun K (2010) Organ reengineering through development of a transplantable recellularized liver graft using decellularized liver matrix. *Nat Med* 16(7):814-U120.

177. Liu Y, Bharadwaj S, Lee SJ, Atala A, & Zhang YY (2009) Optimization of a natural collagen scaffold to aid cell-matrix penetration for urologic tissue engineering. *Biomaterials* 30(23-24):3865-3873.

178. Borschel GH, Huang YC, Calve S, Arruda EM, Lynch JB, Dow DE, Kuzon WM, Dennis RG, & Brown DL (2005) Tissue engineering of recellularized small-diameter vascular grafts. *Tissue Engineering* 11(5-6):778-786.

179. Song JJ & Ott HC (2011) Organ engineering based on decellularized matrix scaffolds. *Trends Mol Med* 17(8):424-432.

180. Craighead HG, James CD, & Turner AMP (2001) Chemical and topographical patterning for directed cell attachment. *Curr Opin Solid St M* 5(2-3):177-184.

181. Altomare L, Gadegaard N, Visai L, Tanzi MC, & Fare S (2010) Biodegradable microgrooved polymeric surfaces obtained by photolithography for skeletal muscle cell orientation and myotube development. *Acta Biomater* 6(6):1948-1957.

182. Barbucci R, Pasqui D, Wirsen A, Affrossman S, Curtis A, & Tetta C (2003) Micro and nano-structured surfaces. *J Mater Sci-Mater M* 14(8):721-725.

183. Thakar RG, Ho F, Huang NF, Liepmann D, & Li S (2003) Regulation of vascular smooth muscle cells by micropatterning. *Biochem Bioph Res Co* 307(4):883-890.

184. Dunn GA & Brown AF (1986) Alignment of Fibroblasts on Grooved Surfaces Described by a Simple Geometric Transformation. *Journal of Cell Science* 83:313-340.

185. Yang J, Rose FRAJ, Gadegaard N, & Alexander MR (2009) A High-Throughput Assay of Cell-Surface Interactions using Topographical and Chemical Gradients. *Adv Mater* 21(3):300-304.

186. Yim EKF, Reano RM, Pang SW, Yee AF, Chen CS, & Leong KW (2005) Nanopattern-induced changes in morphology and motility of smooth muscle cells. *Biomaterials* 26(26):5405-5413.

187. Mahoney MJ, Chen RR, Tan J, & Saltzman WM (2005) The influence of microchannels on neurite growth and architecture. *Biomaterials* 26(7):771-778.

188. Gingras J, Rioux RM, Cuvelier D, Geisse NA, Lichtman JW, Whitesides GM, Mahadevan L, & Sanes JR (2009) Controlling the Orientation and Synaptic Differentiation of Myotubes with Micropatterned Substrates. *Biophys J* 97(10):2771-2779.

189. Lin JB, Isenberg BC, Shen Y, Schorsch K, Sazonova OV, & Wong JY (2012) Thermo-responsive poly(N-isopropylacrylamide) grafted onto microtextured poly(dimethylsiloxane) for aligned cell sheet engineering. *Colloids Surf B Biointerfaces* 99:108-115.

190. Takahashi H, Nakayama M, Shimizu T, Yamato M, & Okano T (2011) Anisotropic cell sheets for constructing three-dimensional tissue with well-organized cell orientation. *Biomaterials* 32(34):8830-8838.

191. Charest JL, Eliason MT, Garcia AJ, & King WP (2006) Combined microscale mechanical topography and chemical patterns on polymer cell culture substrates. *Biomaterials* 27(11):2487-2494.

192. Andersson AS, Olsson P, Lidberg U, & Sutherland D (2003) The effects of continuous and discontinuous groove edges on cell shape and alignment. *Experimental Cell Research* 288(1):177-188.

193. Deutsch J, Motiagh D, Russell B, & Desai TA (2000) Fabrication of microtextured membranes for cardiac myocyte attachment and orientation. *J Biomed Mater Res* 53(3):267-275.

194. Glawe JD, Hill JB, Mills DK, & McShane MJ (2005) Influence of channel width on alignment of smooth muscle cells by high-aspect-ratio microfabricated elastomeric cell culture scaffolds. *J Biomed Mater Res A* 75A(1):106-114.

195. Brydone AS, Dalby MJ, Berry CC, Meek RMD, & McNamara LE (2011) Grooved surface topography alters matrix-metalloproteinase production by human fibroblasts. *Biomedical Materials* 6(3).

196. Zhao Y, Zeng HS, Nam J, & Agarwal S (2009) Fabrication of Skeletal Muscle Constructs by Topographic Activation of Cell Alignment. *Biotechnol Bioeng* 102(2):624-631.

197. Loesberg WA, te Riet J, van Delft FCMJM, Schon P, Figdor CG, Speller S, van Loon JJWA, Walboomers XF, & Jansen JA (2007) The threshold at which substrate nanogroove dimensions may influence fibroblast alignment and adhesion. *Biomaterials* 28(27):3944-3951.

198. Chou L, Firth JD, Uitto VJ, & Brunette DM (1995) Substratum surface topography alters cell shape and regulates fibronectin mRNA level, mRNA stability, secretion and assembly in human fibroblasts. *J Cell Sci* 108 (Pt 4):1563-1573.

199. Tsuda Y, Shimizu T, Yarnato M, Kikuchi A, Sasagawa T, Sekiya S, Kobayashi J, Chen G, & Okano T (2007) Cellular control of tissue architectures using a three-dimensional tissue fabrication technique. *Biomaterials* 28(33):4939-4946.

200. Takahashi H, Nakayama M, Itoga K, Yamato M, & Okano T (2011) Micropatterned Thermoresponsive Polymer Brush Surfaces for Fabricating Cell Sheets with Well-Controlled Orientational Structures. *Biomacromolecules* 12(5):1414-1418.

201. Teixeira AI, Abrams GA, Bertics PJ, Murphy CJ, & Nealey PF (2003) Epithelial contact guidance on well-defined micro- and nanostructured substrates. *Journal of Cell Science* 116(10):1881-1892.

202. Charest JL, Garcia AJ, & King WP (2007) Myoblast alignment and differentiation on cell culture substrates with microscale topography and model chemistries. *Biomaterials* 28(13):2202-2210.

203. Aubin H, Nichol JW, Hutson CB, Bae H, Sieminski AL, Cropek DM, Akhyari P, & Khademhosseini A (2010) Directed 3D cell alignment and elongation in microengineered hydrogels. *Biomaterials* 31(27):6941-6951.

204. Dalby MJ, Riehle MO, Yarwood SJ, Wilkinson CDW, & Curtis ASG (2003) Nucleus alignment and cell signaling in fibroblasts: response to a micro-grooved topography. *Experimental Cell Research* 284(2):274-282.

205. Biela SA, Su Y, Spatz JP, & Kemkemer R (2009) Different sensitivity of human endothelial cells, smooth muscle cells and fibroblasts to topography in the nano-micro range. *Acta Biomater* 5(7):2460-2466.

206. Meredith DO, Eschbach L, Riehle MO, Curtis ASG, & Richards RG (2007) Microtopography of metal surfaces influence fibroblast growth by modifying cell shape, cytoskeleton, and adhesion. *J Orthop Res* 25(11):1523-1533.

207. Lu X & Leng Y (2009) Comparison of the Osteoblast and Myoblast Behavior on Hydroxyapatite Microgrooves. *J Biomed Mater Res B* 90B(1):438-445.

208. Fujioka N, Morimoto Y, Takeuchi K, Yoshioka M, & Kikuchi M (2003) Difference in infrared spectra from cultured cells dependent on cell-harvesting method. *Appl Spectrosc* 57(2):241-243.

209. Yang L, Cheng F, Liu TQ, Lu JR, Song KD, Jiang LL, Wu S, & Guo WH (2012) Comparison of mesenchymal stem cells released from poly(N-isopropylacrylamide) copolymer film and by trypsinization. *Biomedical Materials* 7(3).

210. Canavan HE, Cheng XH, Graham DJ, Ratner BD, & Castner DG (2006) A plasma-deposited surface for cell sheet engineering: Advantages over mechanical dissociation of cells. *Plasma Process Polym* 3(6-7):516-523.

211. Leight J, Liu W, Chaturvedi R, Chen S, Yang M, Raghavan S, & Chen C (2012) Manipulation of 3D Cluster Size and Geometry by Release from 2D Micropatterns. *Cellular and Molecular Bioengineering* 5(3):299-306.

212. Fujita H, Shimizu K, & Nagamori E (2009) Application of a Cell Sheet-Polymer Film Complex With Temperature Sensitivity for Increased Mechanical Strength and Cell Alignment Capability. *Biotechnol Bioeng* 103(2):370-377.

213. Ohashi K, Yokoyama T, Yamato M, Kuge H, Kanehiro H, Tsutsumi M, Amanuma T, Iwata H, Yang J, Okano T, & Nakajima Y (2007) Engineering functional two- and three-dimensional liver systems in vivo using hepatic tissue sheets. *Nat Med* 13(7):880-885.

214. Shimizu T, Yamoto M, Kikuchi A, & Okano T (2001) Two-dimensional manipulation of cardiac myocyte sheets utilizing temperature-responsive culture dishes augments the pulsatile amplitude. *Tissue Engineering* 7(2):141-151.

215. Yamato M, Konno C, Utsumi M, Kikuchi A, & Okano T (2002) Thermally responsive polymer-grafted surfaces facilitate patterned cell seeding and co-culture. *Biomaterials* 23(2):561-567.

216. Kanzaki M, Yamato M, Takagi R, Kikkawa T, Isaka T, Okano T, & Onuki T (2012) Controlled collagen crosslinking process in tissue-engineered fibroblast sheets for preventing scar contracture on the surface of lungs. *J Tissue Eng Regen M*:n/a-n/a.

217. Miyahara Y, Nagaya N, Kataoka M, Yanagawa B, Tanaka K, Hao H, Ishino K, Ishida H, Shimizu T, Kangawa K, Sano S, Okano T, Kitamura S, & Mori H (2006) Monolayered mesenchymal stem cells repair scarred myocardium after myocardial infarction. *Nat Med* 12(4):459-465.

218. Ebara M, Yamato M, Hirose M, Aoyagi T, Kikuchi A, Sakai K, & Okano T (2003) Copolymerization of 2-carboxyisopropylacrylamide with N-isopropylacrylamide accelerates cell detachment from grafted surfaces by reducing temperature. *Biomacromolecules* 4(2):344-349.

219. Al-Fageeh MB, Marchant RJ, Carden MJ, & Smales CM (2006) The cold-shock response in cultured mammalian cells: Harnessing the response for the improvement of recombinant protein production. *Biotechnol Bioeng* 93(5):829-835.

220. Fujita J (1999) Cold shock response in mammalian cells. *J Mol Microbiol Biotechnol* 1(2):243-255.

221. Sonna LA, Fujita J, Gaffin SL, & Lilly CM (2002) Invited review: Effects of heat and cold stress on mammalian gene expression. *J Appl Physiol* 92(4):1725-1742.

222. ChrzanowskaWodnicka M & Burridge K (1996) Rho-stimulated contractility drives the formation of stress fibers and focal adhesions. *Journal of Cell Biology* 133(6):1403-1415.

223. Tomasek JJ, Haaksma CJ, Eddy RJ, & Vaughan MB (1992) Fibroblast contraction occurs on release of tension in attached collagen lattices: dependency on an organized actin cytoskeleton and serum. *Anat Rec* 232(3):359-368.

224. Ng KW & Hutmacher DW (2006) Reduced contraction of skin equivalent engineered using cell sheets cultured in 3D matrices. *Biomaterials* 27(26):4591-4598.

225. Isenberg BC, Tsuda Y, Williams C, Shimizu T, Yamato M, Okano T, & Wong JY (2008) A thermoresponsive, microtextured substrate for cell sheet engineering with defined structural organization. *Biomaterials* 29(17):2565-2572.

226. Carter WG, Rauvala H, & Hakomori SI (1981) Studies on Cell-Adhesion and Recognition .2. The Kinetics of Cell-Adhesion and Cell Spreading on Surfaces Coated with Carbohydrate-Reactive Proteins (Glycosidases and Lectins) and Fibronectin. *Journal of Cell Biology* 88(1):138-148.

Appendices

Appendix A: Copyright and Reproduction Permissions

The following was received by email on 9-20-2012 and grants permission for reuse of the material presented in Chapter 3.

From: CONTRACTS-COPYRIGHT (shared)
To: "Samuel DuPont"
Subject: RE: Manuscript Reuse
Date: Thursday, September 20, 2012 6:31:15 AM

Dear Samuel

The Royal Society of Chemistry (RSC) hereby grants permission for the use of your paper(s) specified below in the printed and microfilm version of your thesis. You may also make available the PDF version of your paper(s) that the RSC sent to the corresponding author(s) of your paper(s) upon publication of the paper(s) in the following ways: in your thesis via any website that your university may have for the deposition of theses, via your university's Intranet or via your own personal website. We are however unable to grant you permission to include the PDF version of the paper(s) on its own in your institutional repository. The Royal Society of Chemistry is a signatory to the STM Guidelines on Permissions (available on request).

Please note that if the material specified below or any part of it appears with credit or acknowledgement to a third party then you must also secure permission from that third party before reproducing that material.

Please ensure that the thesis states the following:

Reproduced by permission of The Royal Society of Chemistry

and include a link to the paper on the Royal Society of Chemistry's website.

Please ensure that your co-authors are aware that you are including the paper in your thesis.

Regards

Gill Cockhead
Publishing Contracts & Copyright Executive

Gill Cockhead (Mrs), Publishing Contracts & Copyright Executive
Royal Society of Chemistry, Thomas Graham House
Science Park, Milton Road, Cambridge CB4 0WF, UK
Tel +44 (0) 1223 432134, Fax +44 (0) 1223 423623
http://www.rsc.org

From: Samuel DuPont [mailto:sjdupont@mail.usf.edu]
Sent: 19 September 2012 21:39
To: CONTRACTS-COPYRIGHT (shared)
Subject: Manuscript Reuse

To Whom it May Concern,

Hello, my name is Samuel DuPont and am the first author on the following publication:

Swelling-induced instabilities in microscale, surface-confined poly(N-isopropylacryamide) hydrogels

Samuel James DuPont Jr. , Ryan Scott Cates , Peter George Stroot and Ryan Toomey

Soft Matter, 2010,6, 3876-3882
DOI: 10.1039/C0SM00021C

Appendix A (Continued)

I am looking to request permission to use material from this publication for my Ph.D. dissertation. I do not intent to reproduce the manuscript in its entirety but would like to use a substantial amount from it as it was a large portion of my fundamental work towards my Ph.D. This includes most of the figures as well as portions of the text (although most text will be rewritten in context of the dissertation)

Please advise me on how I should proceed so I can include this work in my dissertation.

Thank you for your time and attention,

Samuel J. DuPont
PhD Candidate
Chemical & Biomedical Engineering
University of South Florida
Tampa, FL

Appendix A (Continued)

The following was received on 8-23-2012 and grants permission for reuse of Figure 3-34 in Chapter 3.

From: Corinne Griffon
To: "Samuel DuPont"
Subject: RE: Copyright question EPJE
Date: Thursday, August 23, 2012 4:05:00 AM

Dear Sir,

In answer to your request, we are pleased to inform you that you are authorized to reproduce:

Figures 3,6,7 published in Eur. Phys. J. E vol 20, p 119-124 (2006).

We kindly ask you to provide the references of the source: title, year, issue and the URL address of the journal.

Yours sincerely,

Permissions Dept
EDP Sciences

De : Samuel DuPont [mailto:sjdupont@mail.usf.edu]
Envoyé : mercredi 22 août 2012 23:53
À : contact@edpsciences.org
Objet : Copyright question

To Whom it May Concern,

My name is Samuel DuPont and I am a graduate student at the University of South Florida in Tampa, FL. I am currently writing my dissertation as a requirement for my Ph.D. in the field of Chemical Engineering and would like to request permission to reproduce some figures in my dissertation found in the following publication in your journal:

Mora T & Boudaoud A (2006) Buckling of swelling gels. *Eur Phys J E* 20(2):119-124.

Specifically figures 3, 6, and 7.

Thank you for your time and attention,

Samuel J. DuPont
PhD Candidate
Chemical & Biomedical Engineering
University of South Florida
Tampa, FL

About the Author

Samuel DuPont Jr. was born in upstate New York and received his B.S. in Chemical Engineering (*summa cum laude*) and M.E. in Environmental Engineering at the University of South Florida. Samuel's research experience started in his junior year where he spent many weekends learning about bacterial cell culture and molecular biology tools. It was this experience that fostered his love for research science and ultimately led to his decision to pursue a Ph.D. During his time in the lab, Samuel worked closely with many students and assisted in mentoring numerous undergraduate and Master's level students. Samuel was involved in several professional organizations and served as president of the Florida Water Environment Association and as vice-president of the American Water Works Association and has participated in numerous outreach events. In tandem with his doctoral research, Samuel worked closely with Hillsborough County schools to aid in elementary education. Through participation in the NSF funded GK-12 program, Samuel worked with local teachers to enhance elementary education and developed/presented multiple workshops aimed at enhancing teacher knowledge in the fields of science, technology, engineering, and mathematics (STEM). These experiences led Samuel and his close friend and fellow graduate student, Audrey Buttice, to pursue further ways to enhance STEM education at the elementary level. With support and guidance from Dr. Tapas Das, Audrey and Samuel went on to develop a unique program which aimed to facilitate STEM education in the classroom.